CENOZOIC MAFIC TO INTERMEDIATE VOLCANISM AT LAVA MOUNTAIN AND SPRING MOUNTAIN, UPPER WIND RIVER BASIN, WYOMING

by

ANNA CATHERINE DOWNEY

B.S., SUNY College at Oneonta, 2013

A THESIS

submitted in partial fulfillment of the requirements for the degree

MASTER OF SCIENCE

Department of Geology
College of Arts and Sciences

KANSAS STATE UNIVERSITY
Manhattan, Kansas

2015

Approved by:

Major Professor
Dr. Matthew Brueseke

Abstract

The Upper Wind River Basin (UWRB) is located in north-central Wyoming, to the south of the Yellowstone National Park boundary and east of Jackson Hole. Both Lava Mountain and Spring Mountain are Quaternary volcanoes in the UWRB. Lava Mountain is a shield volcano composed of 26 separate lavas capped by a scoria cone. Spring Mountain is located about ~36 km east of Lava Mountain, north of Dubois, WY, where eruptions of basalt cut through Paleocene and Eocene strata. The goal of this study aims to reconstruct the petrogenesis of magmas erupted at both volcanoes using geochemical, petrographic, and isotopic analyses. Important local events in geologic history played a large role in the development of the UWRB. This includes a long history of ancient and Cenozoic subduction, regional extension, and also the migration of the North American plate over the Yellowstone hotspot. The few previous studies on Lava Mountain claim the rocks are mafic in composition, however this was based solely on reconnaissance geological mapping. Geochemical evidence presented in this thesis show Lava Mountain rocks range from basaltic andesite to dacite. Basaltic andesite and dacite are interstratified at the base until approximately 2774 m; the rest of the volcano is andesite. All Lava Mountain samples are largely aphanitic and crystal-poor. Conversely, at Spring Mountain, localized normal faulting controls the location of eruptions of olivine-rich basalt. Petrographic analysis for both Lava Mountain and Spring Mountain display a range of evidence for open system processes, including sieved and/or resorbed pyroxenes, olivines and feldspars, as well as xenocrysts that suggest an influence from crustal assimilation. A petrogenetic model is introduced that discusses how Lava Mountain magma production occurred via fractional crystallization of basalt to dacite, then magma mixing of basaltic andesite and dacite, coupled with small amounts of crustal assimilation, to form the locally erupted andesites.

All samples, including Spring Mountain basalts, have $^{87}Sr/^{86}Sr$ isotopes of 0.70608 and 0.70751, with $^{143}Nd/^{144}Nd$ isotopes of 0.51149 and 0.51157 and εNd values of -18 to -22. Pb isotopes plot to the left of the Geochron and directly on to slightly above the Stacey-Kramers curve. Strontium, neodymium, and lead isotope data suggest that Spring Mountain basalts are melts of ancient (e.g., 2.8 Ga Beartooth province) lithospheric mantle. The high $^{87}Sr/^{86}Sr$ values and exceptionally low εNd values separate the UWRB rocks from both Yellowstone and Snake River Plain volcanics, and suggest they originated from a different magma source. Finally, thermal

evidence suggests melting genesis for UWRB rocks may not be Yellowstone plume related; rather it is more likely linked to Cenozoic extension.

Table of Contents

List of Figures

List of Tables

Acknowledgements

I would like to thank my advisor, Dr. Matthew Brueseke, for accepting me as a student and providing me the opportunity to be part of such an exciting and diverse project. Thank you for all your continuous support, encouragement, and life lessons throughout these past two years. Thank you Dr. Pamela Kempton for all of your advice and help on this project, especially during the final months, and for all the hard work you do to make the geology department a fun community to be a part of. Many thanks to Dr. Saugata Datta for serving on my committee. Thank you to John Morton of Miami University for analyzing the major, trace, and rare earth data, and to Jeff Vervoort of Washington State University for providing the Sr-Nd-Pb isotope data. Thanks to Dr. Shawn Hutchinson in the Kansas State Department of Geography for his help with ArcGIS. Thank you to Caleb Dodd for being the best field partner I could have asked for, and helping me carry all my heavy samples! Additionally, thank you Caleb for providing me with olivine microprobe data for my thesis. I would like to thank the Geological Society of America, the Tobacco Root Geological Society, the Wyoming Geological Association, and the Kansas Geological Foundation for the monetary grants necessary to complete this project. Thank you to all the friends I've made in Kansas, for the countless laughs and good times. You were my family away from home. Thank you to the vast number of students I've taught over the past two years, for being absolutely hilarious and making teaching geology labs a highlight of every week. Last, thank you to my parents, who although they may not know exactly what my research is about, they will always be my biggest supporters. I am so blessed to have had the opportunity to spend the past two years with such wonderful people in Thompson Hall.

Chapter 1 - Introduction

The study presents new data on the physical, temporal, and spatial characteristics of two largely unstudied volcanoes, Lava Mountain and Spring Mountain, which are located southeast of Yellowstone National Park in the Upper Wind River Basin (UWRB) of Wyoming, USA. The purpose of the study is to document the origin of these volcanoes and their erupted magmas.

Geographically, these rocks are located on the southern margin of the Wyoming Craton, in the northeastern most corner of the Great Basin physiographic province, north of the Colorado Plateau, and southeast of the Snake River Plain. Its location raises questions as to the competing influences from prior subduction, regional crustal extension and associated mantle upwelling, plume-related volcanism (Yellowstone hotspot), and ancient lithosphere. This project uses geochemical tools to attempt to unravel these competing processes and influences.

Farallon plate subduction timing correlates with the majority of the Laramide Orogeny, which led to major deformation of the western United States during the Cenozoic (Jurdy, 1984). The UWRB sits atop of the Wyoming Craton, an ancient lithospheric craton composed of Late Archean rocks. Part of the Wyoming Craton may correspond to ancient subduction of oceanic lithosphere along the edges of an older Archean continent (Muller and Wooden, 1988). Both ancient and more recent subduction events have had effects on the UWRB, as suggested by geochemical subduction signatures in Cenzoic igneous rocks (Mirnejad and Bell, 2006; Feeley, 2003). Extension affected northwest WY as evident in structures like the Teton normal fault, extensional corridors in the southeast portion of Yellowstone National Park, and UWRB fault zones mapped by Love et. al (1979). How much of this extension is solely due to Basin and Range extension (Anders et. al., 2009) vs. extension related to a localized stress field associated with the Yellowstone hotspot (Pierce and Morgan, 1992), is unclear. Finally, proximity of the UWRB to the position of the Yellowstone hotspot, and age correlations between UWRB rocks and the youngest Yellowstone eruptions, warrant exploration of any potential petrogenetic relationship between the two. The sole K-Ar date of 0.48 ± 0.06 Ma from Lava Mountain (Obradovich, 1978) suggests it overlaps in age with recent volcanism at the Yellowstone volcanic field, so there is the potential for the two to be petrogenically, and possibly thermally, related.

Regional Geology

The Wyoming Craton stabilized at ~2.8 Ga and underlies the majority of present day Wyoming, southeastern Montana, and small areas of eastern Idaho, western South Dakota, and northern Utah (Mueller and Wooden, 1988; Foster, et. al., 2006). Evidence for Archean subduction in rocks residing in the craton includes radiogenic isotope constraints and trace element data. Craton rocks are now exposed at the surface due to Laramide thick-skinned reverse faulting in many of the regional mountain ranges (e.g., Beartooth, Wind River Range, etc.)

Central Wyoming was a stable shelf environment from the Paleozoic to early Cretaceous, as sediments were deposited into epicontinental seas during transgressions (Ray and Keefer, 1985). Paleozoic sediments were mostly limestone, where Mesozoic strata included shale, siltstone, and sandstone that thicken westward (Keefer, 1970). By the late Cretaceous, seas began to shift eastward due to uplift to the west, leading to both marine and non-marine sediments being deposited in the Wind River Basin. This coincided with the onset of the Laramide Orogeny (and just post-dated the earlier Sevier Orogeny), which created the Rocky Mountains through shallow subduction of the Farallon Plate beginning at ~70 Ma. The Laramide Orogeny was caused by the flattening of the subduction angle of the Farallon Plate that continued until 40-50 Ma (Finn, 2007); mountain ranges were uplifted along high-angle reverse faults and the basin began to subside through the early Eocene, resulting in a large sediment influx of various thicknesses into the basin in a wedge-shaped structure. Laramide structures are evident today in the forms of large down-warped anticlines and dome structures in the basin. By the end of the Eocene, most uplift and subsidence had stopped; however, accumulation of sediment into the Wind River Basin continued through the mid-Miocene (Ray and Keefer, 1985).

Basin and Range extensional tectonism may have played a crucial role in the development of UWRB volcanism. The Basin and Range province extends from Canada through the western United States into Mexico and is generally characterized by two separate extensional phases: an initial phase of low angle normal faulting that exposed mid-crustal rocks at the surface, and a later phase of high angled faulting forming extended terranes. Both magmatism type and timing are variable across areas of the Basin and Range. The beginning of the Tertiary saw a decline in magmatism that increased again at the beginning of the Eocene around 60-70 Ma. In the vicinity of northwest Wyoming, Basin and Range extension is manifested by large-displacement normal faults and associated half-grabens (e.g., Teton normal fault and Jackson Hole, Star Valley, Swan

Valley, etc.). Cenozoic normal faults have been mapped by other workers in the UWRB (e.g., Love et al., 1979, Hart, unpublished) and are likely related. The relationship between Basin and Range extension and the Yellowstone hotspot is debated, but there is likely a link between the two phenomena (e.g., Colgan and Henry, 2009; Camp et al., 2015).

In the UWRB, mid-Eocene to Pliocene rocks are predominantly volcanics of the Absaroka Volcanic Field (Keefer, 1970). Local Absaroka volcanism extends from north of Dubois, WY, northeast into Yellowstone, into southwest Montana. Absaroka volcanic deposits range from 55 to 45 Ma and are associated with at least three individual andesitic stratovolcanoes that produced over 23,000 km^2 of volcanic material (Feeley and Cosca, 2003). Seismic studies show the crust below the Absaroka province is 45-50 km thick (Prodehl and Lipman, 1989). Intercalated with Absaroka lavas are thick air-fall deposits and extensive lahars. Most lavas found in the Absoraka Supergroup (Washburn, Sunlight, and Thorofare Groups) are calc-alkaline and andesitic to dacitic, with an increasing K_2O content to the east (Feeley, et. al, 2002). Calc-alkaline rocks are primarily found in the western Absarokas. Rocks to the east have shoshonite characteristics. Recent studies on Absaroka rocks show evidence for crustal contamination, magma mixing, and fractional crystallization, with greater emphasis on open system processes for calc-alkaline magma genesis (Feeley, 2003). For example, Sr and Nd isotope results indicate that silicic melts from the Washburn volcano originated from partial melting of deep crustal rocks. This contrasts with other volcanic activity in the Absarokas, such as Sunlight Volcano, whose eruptions included shoshonites from mantle-derived magmas (Feeley, et. al., 2002); these rocks primarily evolved through fractional crystallization. The mantle source is very similar for both major rock types (calc-alkaline and shoshonite) and can be chemically traced to ancient depleted lithospheric mantle that has since been enriched by both older and recent metasomatic events. The latter was most likely associated with the eastward subduction of the Farallon Plate under present-day North America (Feeley, 2003).

Small volumes of younger volcanic rocks occur overlying Absaroka Volcanics along the northern margin of the Wind River Basin (in the southern portion of the Absaroka Mountains; Fig. 1.2); some of these are the focus of this study and have been recently been documented by others (e.g., Pilot Knob, Wildcat Hill, and Crescent Mountain; Downey, et. al., 2014; Adams, D. C., 2014). Other volcanoes and lavas exist and have been mapped by Keefer (1957) and Love et al., (1979), though remain unstudied by modern techniques.

Yellowstone Extrusives

Over the past 2 m.y., the Yellowstone hotspot has erupted over 6000 km^3 of primarily felsic and mafic magma (Christiansen, 2001). The most commonly accepted theory for the creation of the Yellowstone volcanic field is a stationary hotspot that is currently located underneath present day Yellowstone National Park, U.S.A. (Christiansen et al., 2002). Compositionally, the system is primarily bimodal (basalt-rhyolite). The origin of the hotspot is still debated, however the melt anomaly first along the Nevada/Oregon border in the middle Miocene, forming the Columbia River-Steens Flood Basalts between 16.6-15.0 Ma (Carlson and Hart, 1987; Christiansen, 2001; Brueseke et al., 2007; Camp and Ross, 2004).

As the North American plate migrated southwest, Yellowstone hotspot-related volcanism migrated to the northeast, eventually forming the Eastern Snake River Plain (ESRP) and ultimately the Yellowstone Plateau (Fig 1.1). Large-scale Tertiary silicic eruptions between 10 and 4 Ma, followed by basaltic dike intrusions into the Holocene, shaped the present day ESRP (Payne et. al., 2013). On the ESRP, rhyolite lavas and pyroclastic deposits are overlain by thin layers of younger basalt from various shield volcanoes; many of the presumed silicic calderas have been infilled by younger basaltic volcanism (Christiansen and McCurry, 2008). Although basalts and rhyolites are abundant, there is sparse evidence of intermediate composition igneous rocks in the region and where present, they are low in volume and related to open-system processes (e.g., magma-mixing) (Christiansen, 2001).

Recent Yellowstone volcanism includes three major explosive silicic eruptions that together helped to form the present day Yellowstone Plateau volcanic field. Each of these three eruptions lasted between 0.5 to 1 m.y.; the Huckleberry Ridge, Mesa Falls, and Lava Creek eruptions occurred 2.1, 1.3, and 0.64 m.y. ago, respectively (Christiansen, 2001). The current caldera at Yellowstone was created during the eruption of the Lava Creek tuffs and recent basaltic volcanism that post-dates this includes young basalts of the Snake River Group, the Osprey Group, and the Madison River Basalt Group (Christiansen, et. al., 2007).

Almost all Yellowstone extrusive rocks are rhyolites, making up 95% of the entire volcanic field (Christiansen, 1984). The few areas of exposed basalts found within Yellowstone are primarily from the first and third eruptive cycles. According to Christiansen and Blank (1972), very few basalts are present that date before ~1 Ma. Basalts followed alternating periods of felsic eruptions in Yellowstone during periods of extension. The total volume of basalts generated is

uncertain. Christiansen and Blank (1972) described two: the Junction Butte Basalt and the Basalt of the Narrows. The Junction Butte Basalt is located underneath the Huckleberry Ridge Tuff in northern Yellowstone and forms an unconformity over the Absoraka Volcanic Supergroup. It is assumed to be only slightly older than the 2 m.y. Huckleberry Ridge Tuff, with limits of 2.0 to 2.4 m.y. (Christiansen, 2001). The Basalt of The Narrows cuts through the Huckleberry Ridge Tuff and the Junction Butte basalt. These rocks have been classified as possibly first or second cycle basalt, depending on the literature, and are extremely similar in both chemistry and lithology to the Junction Butte Basalts (Christiansen, 2001).

Almost all basalts located in Yellowstone erupted during the third eruptive cycle. They are primarily concentrated around areas of previous basaltic activity and extensional faulting. The Unidine Basalt was erupted before the Lava Creek eruption. All basalts studied after the Lava Creek eruption are found outside of the main caldera, layered between rhyolitic ash flows. These include the Swan Lake Flat, Madison River, Osprey, Falls River, Gerrit and Mariiposa Lake Basalts. They are all similar in lithology and chemistry, with the exception of the Madison River Basalt. This basalt contains more potassium, iron, and less calcium and magnesium than the others, which are classified as olivine tholeiites. There is some evidence of mixed lavas of basalt and rhyolite compositions in the basalts of Geode Creek and Mariposa Lake (Christiansen, 2001, Pritchard and Larsen, 2013).

The close proximity to hotspot affected areas suggest there may be a connection between the Yellowstone volcanic field and young Upper Wind River Basin (UWRB) volcanism. Further chemical analysis and comparison of these basalts to Lava and Spring Mountain samples is found in Chapter 4.

Local Geology

The UWRB is located in north-central Wyoming, to the south of the Yellowstone National Park boundary and east of the Eastern Snake River Plain (Fig 1.2). It is bounded on all sides by remnants of the Laramide Orogeny, including the Wind River and Owl Creek uplifts (Keefer, 1970), and opens to the east and south to form one of the most prominent basins in Wyoming (Keefer, 1957). The Wind River Range resides to the west, the Washakie, Owl Creek, and Southern Bighorn Mountains to the north, the Casper Arch to the east, and Granite Mountains to the south (Keefer, 1970). The Wind River Basin is partially defined by its highly folded and faulted anticlinal

uplifts (Seeland and Brauch, 1975).

Precambrian igneous and metamorphic rocks outline the north, south, and western flanks of the Wind River Basin. These include over 10,000 km^3 of Late Archaen granite, schist, and gneiss cut by mafic dikes (Keefer 1970). From the late Cretaceous through early Tertiary, sediments removed during uplift of the Wind River Mountains were deposited into the central parts of the Wind River Basin until uplift halted in the late Eocene. Rocks deposited pre-Tertiary in the basin total almost 17,000 ft. in thickness (Seeland and Brach, 1975). Volcaniclastic deposits from the Absoraka Range, including volcanic conglomerate and tuffaceous sandstone, compose much of the Eocene sedimentary strata found in the UWRB (Keefer, 1970). Strata was also formed from the extensive erosion of uplifted areas surrounding the Wind River Basin after Laramide uplift ceased, including 8,000 ft. of Wind River Formation alone (Finn, 2007).

Both Lava Mountain and Spring Mountain lie in the UWRB, WY. The UWRB is located northeast of the Great Basin, north of the Colorado Plateau, and southeast of the Yellowstone Plateau volcanic field. At Yellowstone, the end of the most recent caldera cycle was marked by intracaldera effusive rhyolite volcanism and coeval mafic magmatism, some of which was extracaldera in origin; basalts often erupted along N-S trending normal faults (Christiansen 2001). The oldest post-third cycle rhyolites at Yellowstone are 0.525 myr old and the oldest mafic eruptions occurred at 0.588 kyr (Abedini, et. al., 2007; Christiansen, et. al., 2007). In the UWRB, Lava Mt. is a partially dissected shield volcano composed of twenty-six separate lavas capped by a cinder cone (Love and Love, 1997; Fig 1.3). One of the upper-most lavas yielded a K-Ar age of 0.48 ± 0.06 Ma (Obradovich, 1978). If accurate, this places Lava Mt. volcanism temporally coincident with the mafic eruptions associated with the end of the third Yellowstone caldera cycle, and considerably younger than the Absoraka Volcanics.

About 38 km east at Spring Mt., undated basalts erupted along normal faults that cut Paleozoic and Eocene strata (reconnaissance fieldwork by M. Brueseke and W.K. Hart; Fig. 1.4). Mapping by Keefer (1957) indicate that erupted lavas flowed south into the basin. Their relative lack of weathering, existing vegetation, and stratigraphic position, indicates they are younger than Absaroka Volcanics.

Three additional volcanic bodies discussed in this thesis, both intrusive and extrusive, can be found in and around the UWRB in addition to Lava Mountain and Spring Mountain (Fig. 1.2). Approximately 2 km west of Lava Mountain, the alkaline intrusive complex of Pilot Knob has

been dated by K-Ar geochronology at ~3.4 Ma (Obradovich, 1978). Another intrusive body, Wildcat Hill, exists ~5 km northwest of Pilot Knob; it occurs on an apparent fault zone that lies on strike from a major extension-related fault zone ~10 km northwest of Pilot Knob (Dodd, 2015, Fig. 1.5). Similar to Spring Mountain, Wildcat Hill has not been dated so its age in relation to the other UWRB bodies is uncertain. Regional extrusives include Crescent Mountain, a 3.6 Ma (via K-Ar geochronology) volcano and lavas located north of the UWRB in the southern Absorakas, that erupted 60-90 m of basaltic trachyandesite to trachyandesite (Fig. 1.6) (Blackstone 1966).

Extensive faulting in the region is evident and includes several fault zones that extend south from Yellowstone toward Lava Mountain (Christiansen, 2001 [map]). These are likely a result of recent extension in the western United States that began in the early Cenozoic, which could either be Basin and Range-related or possibly due to Yellowstone hotspot-North America lithosphere interaction. This includes faulting along the Teton normal fault just west of the study area, which formed Jackson Hole, WY (Byrd et al., 1994). It is unclear how the normal faulting at Spring Mountain occurred, but it is likely related to this regional extension. Lava Mountain, Pilot Knob, and Wildcat Hill are all aligned along a southwest-trending fault zone (Fig. 1.3). Exposure of both extrusive and intrusive rocks suggests possible deep crustal fracturing in the area (Protska and Antweiler, 1979).

To summarize, the youngest local eruptions are from Lava Mountain at approximately 0.5 Ma. Pilot Knob an intrusive complex, and the Crescent Mountain volcano, are very similar in age at ~3.4-3.6 Ma. No age data has been reported for Spring Mountain basalts or the Wildcat Hill plug.

Previous Work

The UWRB volcanics were initially mapped by Keefer (1957) and Love et al. (1979), but aside from documenting their occurrence, no research has been undertaken to understand the petrogenesis of either Lava or Spring Mountain, including whether (or how) these lavas are related to Yellowstone volcanism. Spring Mountain has been mapped in depth by Miami University Instructors and their field camp attendees over several decades. A portion of the area was officially mapped in 1999 by M. Brueseke, W. K. Hart, C. Haley, and D. Snyder, showing the location of some of the exposed basalts and their relationship to high-angle faults that cut deformed Paleozoic sedimentary strata. While mapping, Brueseke, Hart, Haley, and Snyder observed large amounts of

scoria around certain faults, indicating fissural eruptions via the faults (Brueseke, personal communication); this was verified during my fieldwork. The Christiansen (2001) map of Yellowstone featured Quaternary basalts mapped at Lava Mountain's location on the USGS Yellowstone Quadrangle. However, this study demonstrates that no basalt is present at Lava Mountain; only basaltic andesite to dacitic lavas. K-Ar dating and petrography on Pilot Knob are reported in a 1978 USGS Professional Paper (Obradovich, 1978); Dodd (2015) has performed detailed geochemical and electron microprobe work on Pilot Knob. Blackstone (1966) analyzed the stratigraphy and mapped Crescent Mountain. I report in this thesis, chemistry from two samples, collected by D. Adams (2013) that shows the samples are basaltic andesitic to dacitic, respectively. Protska and Antweiler (1979) also briefly discuss Crescent Mountain, although they indicate that the lavas are basaltic and not andesitic, based only on geological mapping. No systematic study of Wildcat Hill has been completed but Dodd (2015) analyzed two samples from the intrusive body that are dacites. Overall, they are most geochemically similar to Lava Mountain magmas than to the other UWRB igneous complexes.

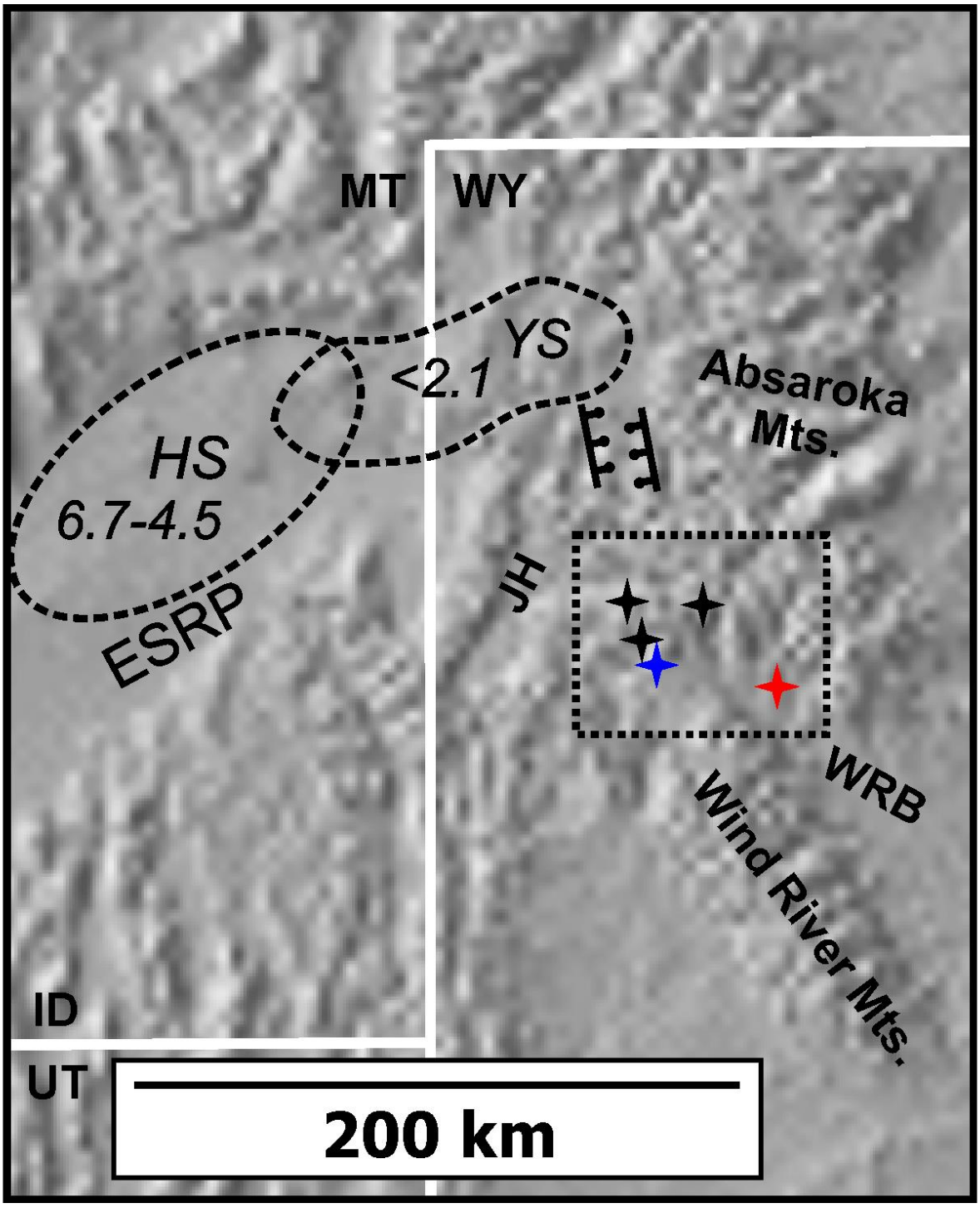

Figure 1.1 Map of Yellowstone hotspot progression through Eastern Snake River Plain. Digital elevation model showing the location of Snake River Plain-Yellowstone volcanic fields (dashed ovals), and study area; black dashed box). HS, Heise; Y, Yellowstone; numbers are ages, Ma, when the volcanic fields were active. JH, Jackson Hole, WY; WRB, Wind River Basin. Blue star is Lava Mountain, red star is Spring Mountain. Black stars are other relevant igneous bodies in the UWRB.

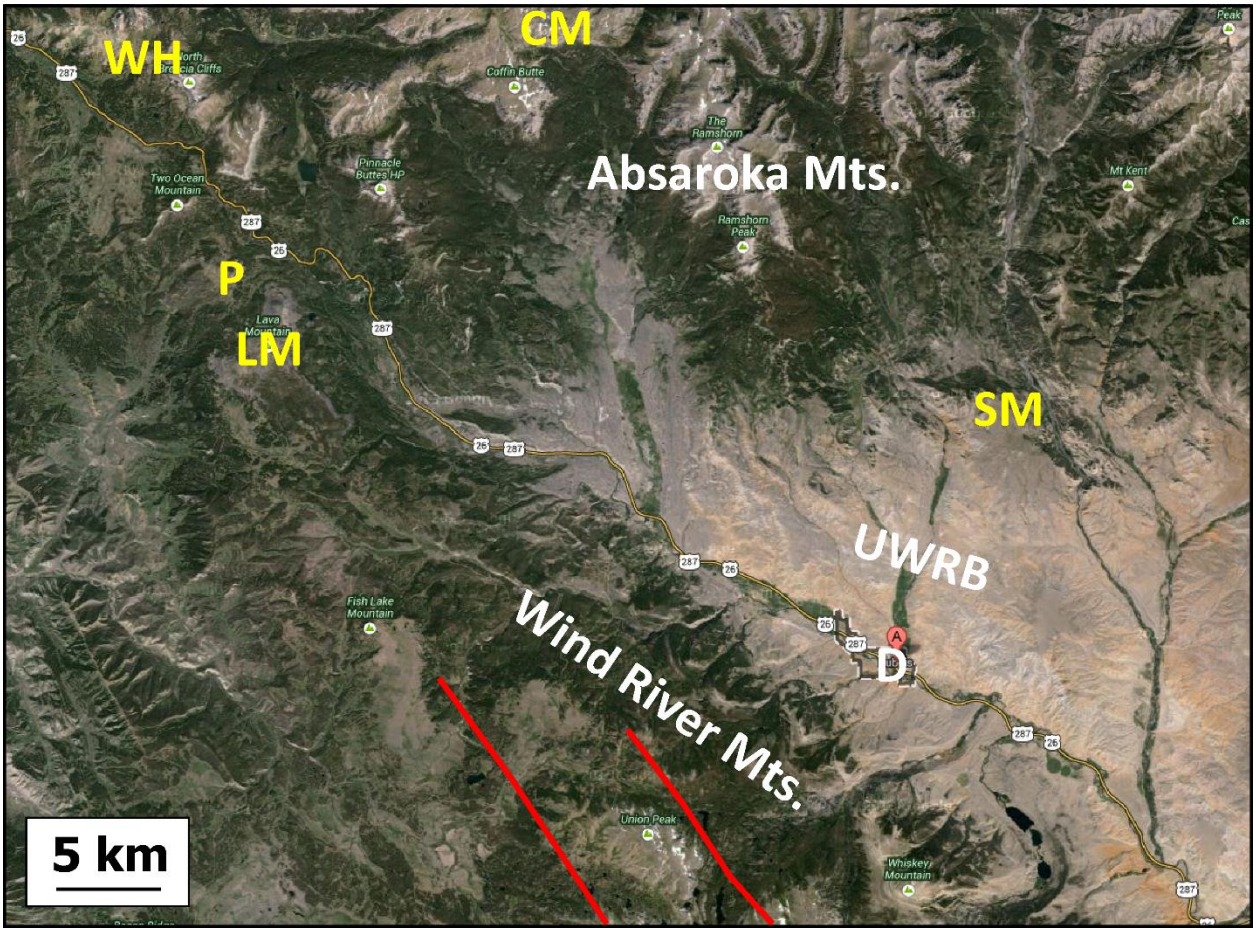

Figure 1.2 Google Earth satellite image showing study area (Black Box in Fig. 1) P, Pilot Knob; WH, Wildcat Hill; LM, Lava Mountain; SM, Spring Mountain; CM, Crescent Mountain; UWRB, Upper Wind River Basin. Red lines indicate normal faults projected from the south from J. D. Love map, 1979.

Figure 1.3 Lava Mountain A) Cinder cone facing southwest B) Side view facing west. Glacially truncated cliff exposes horizontal stratigraphy of lavas above Pellham Lake. Cliff is approximately 3000 m high.

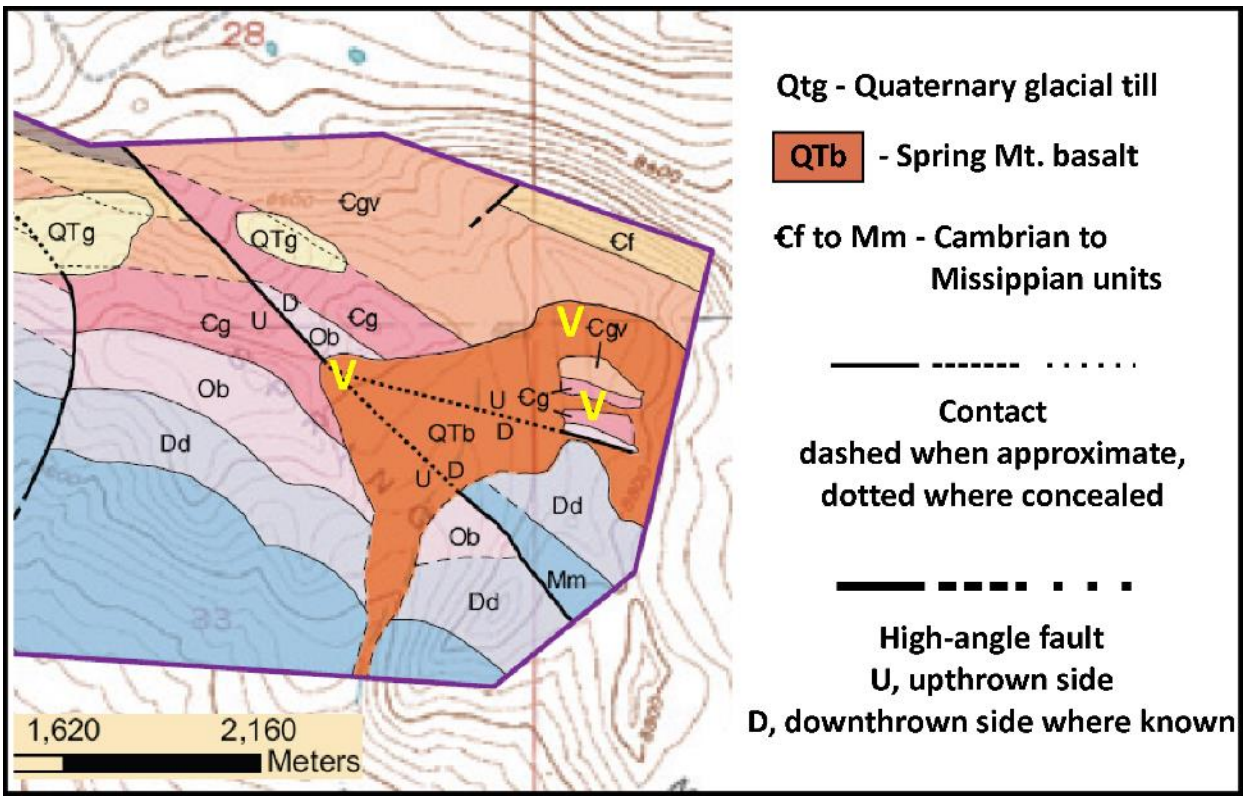

Figure 1.4 Geologic map of a portion of Spring Mountain, WY (M. Brueseke and W.K. Hart, unpublished), illustrating the location of some of the exposed basalts and their relationship to high-angle faults that cross-cut deformed Paleozoic sedimentary strata. One vent is located where the large NW-SE trending fault is intersected by another fault that trends more E-W (at contact with Ob, Ordovician Bighorn Fmn.); pervasively oxidized spatter is found at this location indicating explosive volcanism and partially defining the vent. The three major vents are marked with a yellow "V".

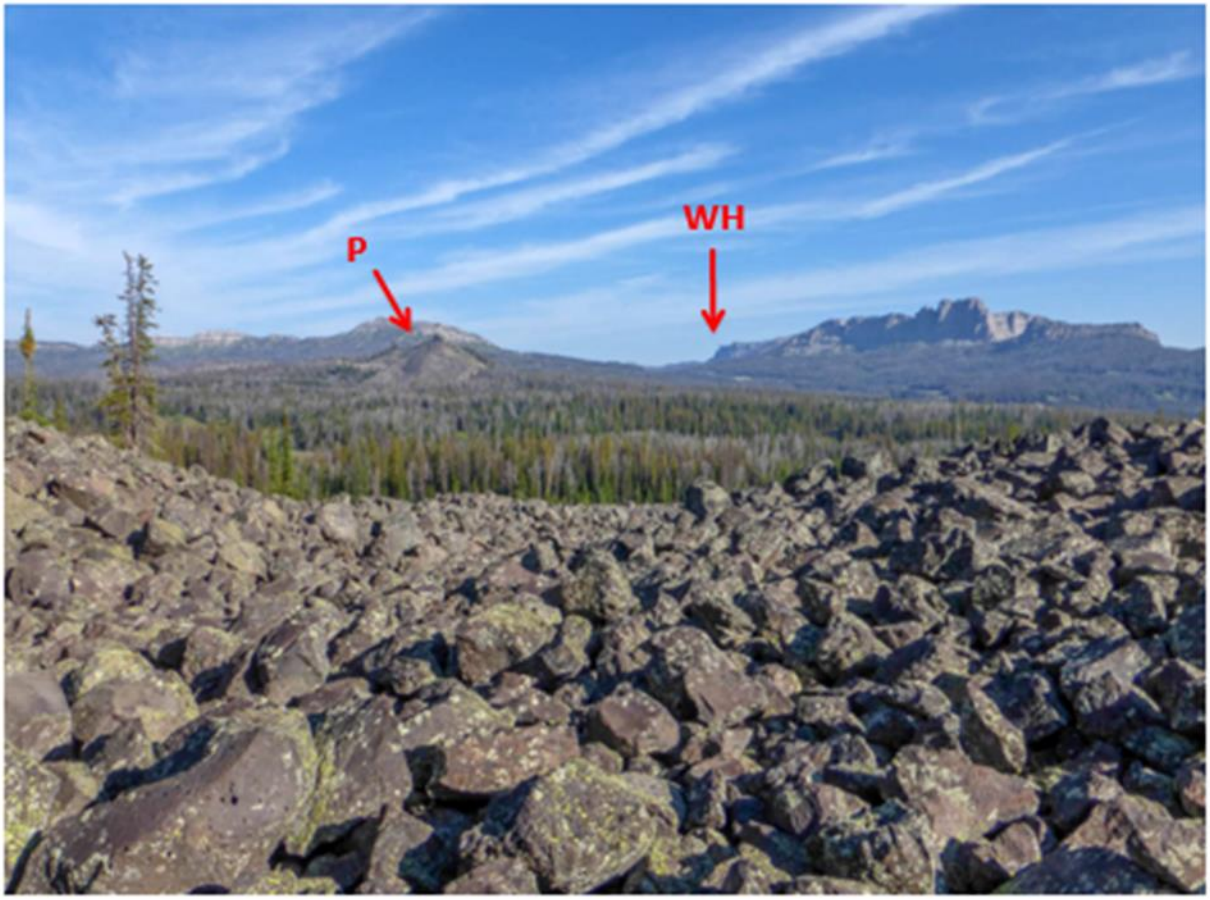

Figure 1.5 Pilot Knob (P), as an alkaline intrusive body is located ~5 km west of Wildcat Hill (WH). Northwest view from base of Lava Mountain. Large boulder in the left corner is approximately 1.5 m long.

Figure 1.6 Crescent Mountain. Google Earth satellite illustrating scoria cone that was built on a surface of Eocene Absaroka volcanics. Red arrow indicates scoria cone. The scoria cone is approximately 3467 m high.

Chapter 2 - Methods

Field Methods

Samples were collected from one field season spanning eleven days. Sampling locations were first determined based on observable physical differences in areal photographs that suggested potential geochemical diversity. At Lava Mountain, stratigraphic relationships between lavas and hand sample descriptions further distinguished sample areas. A few areas could not be samples due to lack of physical accessibility. For Spring Mountain, samples were chosen to document the eruptive loci and also outflow. For Lava Mountain, sampling began at the scoria cone and progressed down to the lowest lavas stratigraphically. Samples were taken where stratigraphic relationships were clear. All Lava Mountain samples were collected from the southeastern and northern portions of the lava field, on Spring Mountain proper. Keefer (1957) also mapped highly weathered basaltic lava to the south of Spring Mountain, extending down into the UWRB north of Dubois, WY. Only the freshest rocks were targeted for collection and analysis, as many had been subjected to weathering. Hand sample descriptions were recorded in the field. Coordinates for sample locations were taking using a Garmin GPS device using 1927 North American Datum (NAD27). Samples were also utilized from summer 2013 reconnaissance fieldwork. Both coordinates and field descriptions can be found in Appendix A.

Seventeen samples in total were collected from Lava Mountain and Spring Mountain, with two from Spring Mountain and fifteen from Lava Mountain. Three Pilot Knob and two Wildcat Hill samples were also collected for analysis for Zachary Dodd's thesis, totaling twenty-two samples collected from the summer 2014 field season. The suite of samples collected in 2013 include one Lava Mountain, one Pilot Knob, and three Spring Mountain samples. Additionally, nine Lava Mountain, two Pilot Knob, and six Crescent Mountain samples were previously collected by David Adams are utilized in this project. Altogether, twenty-five Lava Mountain, five Spring Mountain, six Pilot Knob, two Wildcat Hill, and six Crescent Mountain samples were analyzed for geochemistry and petrography; six were analyzed for Sr-Nd-Pb isotope characteristics. Crescent Mountain, Wildcat Hill, and Pilot Knob sample analyses are only briefly mentioned for local geology comparisons and are not the focus of this thesis.

Analytical Methods

Analytical, Trace, and Rare Earth Elements

Samples larger than fist size were first split into smaller sections using a RockLabs Hydraulic Press equipped with tungsten jaws. Weathered surfaces were removed from all samples in a two-stage process. The first step involved using a rock saw with a diamond-tipped blade to remove outer surfaces. Any weathered material not removed in this way was removed by grinding the rock against a 60 grit, 8" silicon carbide (sandpaper) disc on a grinding wheel, and then grinded again to ensure each sample had no remaining flaws. All samples were then bathed with distilled water and cleaned thoroughly using an ordinary toothbrush. After drying, the samples were crushed into pebble-sized pieces using the crushing jaws of the same RockLabs Hydraulic Press. Crushed samples were randomized using a cone-and-quarter method. A small amount of crushed sample was powdered using a Spec Industries Shatterbox machine with aluminum ring and puck pulverizers. The powders were stored in glass viles in preparation for shipping for analysis.

Inductively coupled plasma optical emission spectrometry (ICP-OES) analyses of the original seventeen samples were completed at Miami University. This included major (Si, Al, Ti, Fe, Mn, Mg, Ca, Na, K, and P) trace and rare-earth element (REE) analyses (Ni, Cr, Sc, V, Ba, Rb, Sr, Zr, Nb, Cu, Co, Zn, Pb, Y, La, Ce, Pr, Nd, Sm, Eu, Gd, Tb, Dy, Ho, Er, Tm, Yb, and Lu). LOI values were also measured for each sample. LOI data are reported along with major and trace element results in Appendix B. REEs (both LREE and HREE) for eleven samples were also analyzed at Miami University using ICP-OES. To prepare, 200 mg of all eleven samples was fused with 600 mg of $LiBO_2$. This was passed through a cation exchange resin to concentrate the REE and separate the Ba from the REE to reduce interferences during analysis.

All iron analyzed for the samples collected during summer 2014 fieldwork are reported as FeOtotal. An estimate of the Fe^{2+}/Fe^{3+} ratio has been determined using the methodology described by LaMaitre (1976) and all major element data used in diagrams and petrogenetic models are reported as anhydrous. Samples collected during the summer 2013 field season by Brueseke and Ingalls were prepared using similar methods to those described above. The five 2013 powders (MB13-1, MB13-2, MB13-3, MB13-4A, MB13-4B) were sent to Franklin and Marshall College for major and trace analysis using a Panalytical PW 4204 XRF spectrometer. The specific XRF methodology are outlined in Mertzman (2000).

The Lava Mountain, Pilot Knob, and Crescent Mountain samples provided by Dave Adams were analyzed for major, trace, and rare earth elements via XRF and ICP-MS at Washington State University using a ThermoARL Advant'XP+ sequential X-ray fluorescence spectrometer and an Agilent 7700 ICP-MS (REE) . (Gaschnig, et. al., 2011).

Sr-Nd-Pb Isotopes

Six samples were selected for isotope analysis: three from Lava Mountain, and one each from Spring Mountain, Pilot Knob, and Crescent Mountain. For Lava Mountain, one scoracious andesite, one dacite, and one basaltic andesite were chosen. Each sample was carefully selected to provide the best overall summary of the study area as a whole. Sr-Nd isotopes were analyzed at Washington State University using a ThermoFinnigan Neptune multicollector (MC)-ICP-MS. The effects of mass fractionation during calculations for Nd isotopes were corrected using $^{143}Nd/^{144}Nd = 0.7219$ and normalized to the Ames standard; Sr isotopes were corrected to $^{86}Sr/^{88}Sr = 0.1194$ and normalized using NBS-987. Data was presented as two standard errors, with an average reproducibility of two standard deviations. The average reproducibility for $^{87}Sr/^{86}Sr$ on the NBS-987 standard was 0.00005, and reproducibility for $^{143}Nd/^{144}Nd$ on the Ames standard was 0.00002. Sr and Nd isotope ratios are reported as measured values (e.g., no age correction is applied) because of the young age of the samples. Current values of 0.512630 for $^{143}Nd/^{144}Nd$ and 0.160 for $^{147}Sm/^{144}Nd$ were used to calculate εNd values. Pb isotopes were also analyzed on the same six samples at Washington State using the same (MC)-ICP-MS. Ratios measured were $^{206}Pb/^{204}Pb$, $^{207}Pb/^{204}Pb$, and $^{208}Pb/^{204}Pb$ for a reproducibility of two standard deviations. Reproducibility for $^{206}Pb/^{204}Pb$, $^{207}Pb/^{204}Pb$, and $^{208}Pb/^{204}Pb$ averaged 0.0015-0.0016, 0.0016-0.0017, and 0.0043-0.0044, respectively.

Microprobe Analysis

Microprobe work was completed at the University of Colorado during March 2015 by Zachary Dodd. Two thin sections were chosen for microprobe work, MB13-3 and MB13-4a. Both are Spring Mountain samples chosen for olivine chemistry determination. Microprobe analysis was performed on a JEOL JXA-8600 equipped with four wavelength-dispersive spectrometers and one energy-dispersive spectrometer. Analyses were acquired using Geller microprobe automation with a dQuant interface. Mg and Fe compositions for olivines from these two samples are reported in Table 4.1 and Appendix B.

Petrography

After splitting all samples, billets were created at KSU using a diamond-tipped blade saw. The pieces were chosen based on freshness and the potential for obtaining a good billet from the sample. All 17 billets for Lava Mountain and Spring Mountain from summer 2014 fieldwork were sent to Spectrum Petrographics, Inc. for thin section preparation. Thin sections had previously been created one year prior for the samples collected during August 2013 fieldwork for Lava Mountain and Spring Mountain. Three thin sections for Crescent Mountain were provided by Dave Adams at the end of the summer 2014 field season. Using all 24 thin sections (17 from summer 2014, 5 from summer 2013, and 3 from Dave Adams) ensured a solid petrographic analysis of Lava Mountain, Spring Mountain, and Crescent Mountain. Analysis included general petrography and more detailed point-counting of mineral abundances. Both were performed using a Nikon Eclipse E600 POL microscope. Point counts were completed with a target of 700-800 counts per thin section, stepping every 1 mm. Multiple photomicrographs were taken of each sample with the microscope, each image having both a PPL and XPL view at different scales. All general and point-count descriptions can be found in Appendix A.

Chapter 3 - Field Relationships, Physical Characteristics, and Petrography

Field Relationships

Lava Mountain is approximately 10,400 feet above sea level and total eruptions cover approximately 5.46 km^3. Area calculations were done using ArcGIS while making comparisons to field maps. There is evidence Lava Mountain was shaped by glacial activity, including truncated cliffs that expose the lavas (Fig. 1.5 and 3.2). The last major glacial maximum in northern Wyoming occurred about 21,000 years ago during the Holocene (Pierce, K. L., 2003). Field observations suggests there are compositional differences with elevation relative to the position of the scoria cone at the top of the section. Physical changes in rock type suggest alternating eruption of lavas ranging in composition from mafic to felsic, with more felsic and mafic rocks predominant lower in the section, and intermediate rocks near the top (Fig. 3.1). Geochemical characteristics (presented below) and field observations divide Lava Mountain lavas into three compositional groups: basaltic andesites, andesites, and dacites, and support the observed physical differences.

Andesite lavas cover approximately 4.56 km^3 and are volumetrically the largest rock type making up Lava Mountain. The youngest and stratigraphically highest unit on Lava Mountain, the scoria cone, is composed entirely of scoria blocks that are rounded in shape and are typically slightly oxidized (Fig. 3.3 a, b). The vent itself (e.g., the cone) is located on the eastern side of Lava Mountain. Although the andesite scoria has not been dated, field evidence suggests it is the youngest eruption to have occurred on Lava Mountain. Volcanic bombs are common (Fig. 3.3b). Andesite lavas seen in outcrop stratigraphically lower than the cinder cone exhibit both platy and blocky characteristics in cross-section. Most andesite lavas are platy and exhibit sheet jointing in those units immediately above a basal breccia, consisting of scoriaceous clasts. Outcrops of platy lavas range from 10-50-m-thick. Individual plates range up to 10 cm in thickness. Most are not horizontal throughout their lateral extent, but tend to ramp and curve due to flow (Fig. 3.4). Elongated vesicles 3 cm and smaller in maximum dimension are common in these lavas. Some andesite samples exhibit thin (1-3 mm) laminations defined by flattened vesicles, indicative of flow (Fig. 3.5). In contrast, some andesite lavas are blockier have contain smaller vesicles (Fig. 3.6).

Outcrops of blocky basaltic andesite lavas range up to 15-m-thick. Blocky basaltic andesite lavas are also associated with basal and upper portions of outcrops that show autobrecciation (Fig. 3.7, 3.8a). Some samples have vesicles that exhibit flow patterns (Fig. 3.8b). Dacitic lava also occur near the base of Lava Mountain and is characterized by upper and lower vitrophyre in hand specimen; petrographic examination, however, shows that groundmass glass makes up less than 15% of the rock, with the remainder being very fine grained plagioclase in groundmass. (Fig. 3.9). The same dacite lava was found on two separate areas on high ridges from the same lava.

The Spring Mountain lavas are largely hidden by an extensive amount of vegetation (Fig. 3.10). Based on flow patterns and chemical analysis (presented below), Spring Mountain lavas are the result of one eruption. The majority of lava is concentrated to the south (Keefer, 1955), and smaller volume lavas are seen associated with vents to the east. Three different textural varieties of basalt were discovered: fine grained, coarse grained, and highly vesicular (Fig. 3.11). Both the coarse and fine-grained varieties were located in the valleys in close proximity to one another. Oxidized vesicular basalt was found in the furthest saddle to the west, and the volume of this basalt increases to the north. Not every saddle observed in Fig. 1.4 has basalt, although the three saddles where pervasively oxidized scoria are present designate fissural vents (Fig. 1.4). No Spring Mountain samples have ever been dated, and due to time constraints, it was not possible to include their geochronology as part of this study.

Crescent Mountain volcano was not studied in detail as part of this study. All field descriptions included here are based on Blackstone (1966). D. Adams provided the thin sections and geochemical data used in this study. The basaltic trachyandesites from Crescent Mountain represent the lavas from the scoria cone that erupted prior to scoria cone formation. The individual lavas, collectively, are estimated to be around 200-m-thick. The dacites collected from Crescent Mountain are from a dike that intrudes the scoria cone.

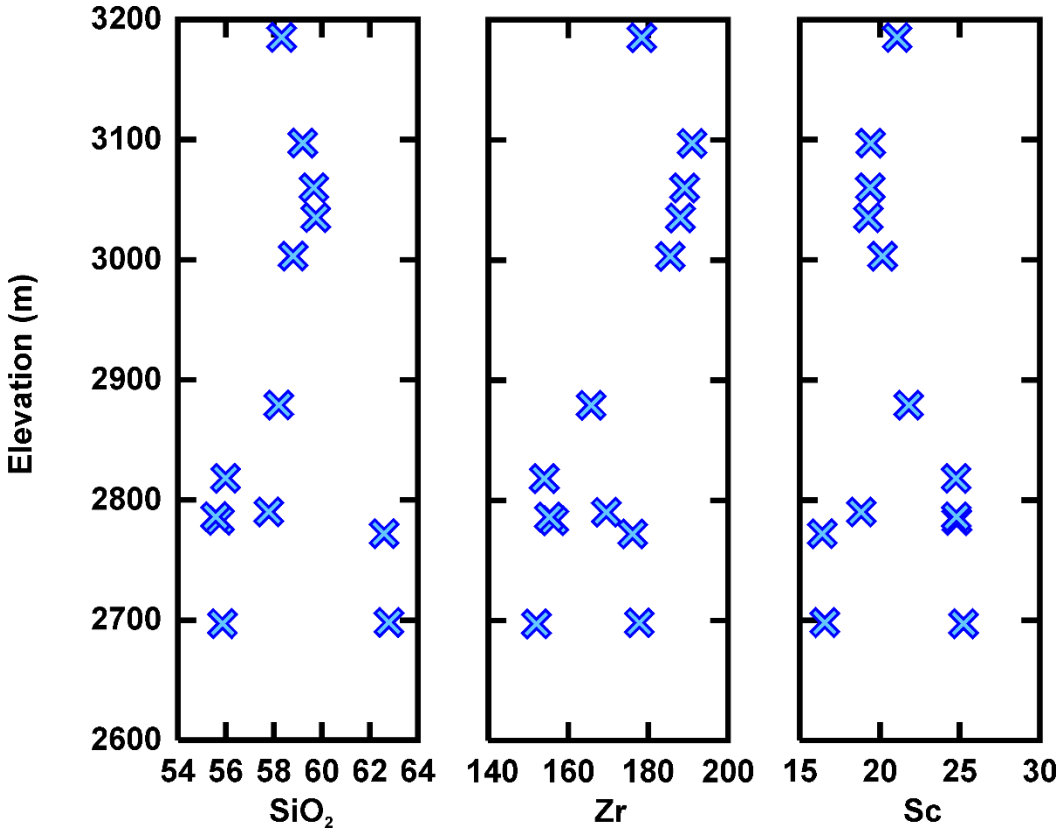

Figure 3.1 Chemostratigraphy of Lava Mountain. The base of the mountain is interstratified basaltic andesite and dacite. Above approximately 2774 m, the rest of the mountain is andesite.

Figure 3.2 Individual lavas on Lava Mountain, exposed through glaciation in the Pleistocene. Lavas are all horizontal. Evergreen trees on the mountain are approximately 20 m tall.

Figure 3.3 A) Scoria on top of Lava Mountain, AD14-4. Rock hammer is approximately 40 cm long. Scoria average about 15 cm. B) Volcanic bombs on cinder cone show glassy banding.

Figure 3.4 Platy andesite ridge, approx. 45-60-m-thick. Andesite is ramping upwards and highly contorted.

Figure 3.5 Platy andesite, AD14-5. Light gray laminations are observed across the center of a lava clast, and average about 1-3 mm thick. Hiking pole is approximately 60 cm in image.

Figure 3.6 Blocky, vesicular andesite at the NW base of Lava Mountain, AD14-18. Rock hammer for scale. Hammer is 33 cm long.

Figure 3.7 Blocky-jointed basaltic andesite, AD14-15. Rock hammer for scale is approximately 33 cm.

Figure 3.8 AD14-9 A) Outcrop 10-12 m thick, with individual plates 1-4 inches thick. Oxidized basal autobreccia (in box) on bottom grades into platy, stony lava above. B) Vesicles show flow patterns near basal breccia of same sample.

Figure 3.9 Dacite vitrophyre, AD14-10. Vesicles are flattened due to flow.

Figure 3.10 Spring Mountain topography. Sagebrush covers much of the basalt lava. Red arrow denotes large boulder-sized basalts in the front of the mountain. Low hills are Paleozoic sedimentary strata.

Figure 3.11 Three types of mafic rock at Spring Mountain. Highly oxidized scoria to the left (MB13-3), coarse-grained basalt to the right (MB13-4A) and fine-grained basalt on top (MB13-4B). Both basalts are found in the valley, where vesicular basalt is only found at topographic high along fissure vents.

Physical Characteristics and Petrography

The geochemistry of Lava and Spring Mountain magmas will be discussed in detail in Chapter 6. However, to classify the rocks and describe their petrography, initial classification has been made via a total alkali vs. silica diagram (Le Maitre, 1989) (Fig 3.1), Lava Mountain rocks plot as basaltic andesites, andesites and dacites, and Spring Mountain rocks are basalts. Although not discussed in detail as part of this study, Crescent Mountain rocks are basaltic andesites and dacites, while Pilot Knob samples plot as basaltic trachyandesites and Wildcat Hill rocks are dacitic.

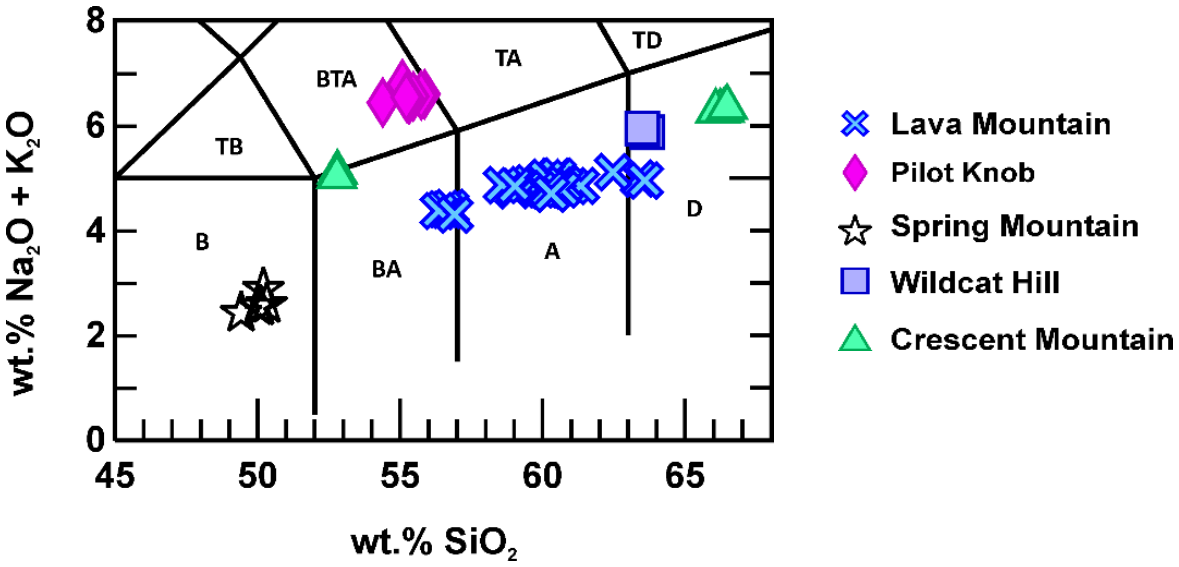

Figure 3.12 Total alkali silica diagram. Notice the diversity of compositions from all eruptive centers, including K-rich Pilot Knob.

Lava Mountain Basaltic Andesites

The basaltic andesites from Lava Mountain are all aphanitic with sparse phenocrysts. Black euhedral orthopyroxene phenocrysts range from 0.25 - 2.00 mm in size in some rocks. Round vesicles averaging 1-4 mm in size are <5% modally in all rocks. Two groups of basaltic andesites were observed. One consists of light tan to gray rocks that show light banding and contain ca. 5% orthopyroxene phenocrysts. Rocks of the other group are blocky, contain more phenocrysts (up to 10%) but fewer vesicles.

Petrographically, all basaltic andesites have subhedral to anhedral orthopyroxene phenocrysts, many of which exhibit resorbed textures (Fig 3.13b). The major distinguishing

petrographic feature separating the basaltic andesites from other Lava Mountain volcanics is the presence of olivine phenocrysts in all samples. Although not very abundant (~3-7% modally), the olivines range from euhedral to anhedral and average 0.3-0.6 mm in size; some exhibit skeletal morphologies (Fig 3.13a, c). Almost all olivines, regardless of morphology, have thin brown iddingsite rims. Some subhedral olivines are surrounded by thin, opaque rims of oxide minerals. Some orthopyroxenes tend to have a brown to bright green pleochroism. These orthopyroxenes have a 2V of 45 and above and are biaxial negative, suggesting the composition is more Mg-rich than groundmass orthopyroxene and could be between bronzite and hypersthene. Groundmass ranges from 75 to 90% of the rocks and consists of plagioclase, orthopyroxene (approx. 85%), and (<10%) oxide minerals that are approximately 0.05 mm in size. Feldspars are observed in small clots in several areas averaging 0.5 mm, identified by their twinning and biaxial interference figure. Additionally, one single large xenocrystic quartz crystal that is 4.55 mm in length and 1.60 mm wide is observed in AD14-14 accounting for 3.29% modally. No other quartz is observed in any other Lava Mountain basaltic andesite or andesite. The quartz is highly fractured and partially surrounded by secondary opaque minerals (Fig 3.13f).

Lava Mountain Andesites

All but two Lava Mountain andesites have an aphanitic groundmass with pyroxene phenocrysts up to 3 mm in size in some samples. Two andesite samples appear vitrophyric in hand sample. They are black and glassy on fresh surfaces, with sparse vesicles. All of the andesites are vesicular and contain anywhere from ca. 6-24% orthopyroxene phenocrysts modally; none contain olivine. Vesicles are asymmetrical, demonstrating flow textures, and average about 3-5 cm in maximum dimension. They can be separated into two subgroups based on mode of eruption: scoriaceous andesite and andesite lava. The scoria sample is highly vesicular (~45% modally), containing equant orthopyroxene phenocrysts that average 0.1 mm (up to 6.7% of the mode), many of which display sieve textures. Andesites with interstitial textures contain phenocrysts of euhedral to subhedral orthopyroxenes, some of which are slightly resorbed (2-4 mm in size), and rounded plagioclase (2-6 mm in size). Petrographically, the groundmass percentage in all Lava Mountain samples range between 65%-98%, with the dacites on the order of 96%-98%. Disequilibrium textures are observed in andesites in the form of resorbed and, in some cases, zoned plagioclase phenocrysts (Fig. 3.14d), zoned and resorbed orthopyroxene phenocrysts, and reaction rims

surround orthopyroxenes (Fig. 3.14e). The specific zones plagioclase crystal in Fig. 3.14d is approximately 0.7 mm wide. Select orthopyroxenes, such as the rimmed orthopyroxene in AD14-16, exhibit the same bright green pleochroism found in the basaltic andesites, in smaller quantity (Fig. 3.14e). The green color is primarily observed in orthopyroxenes that are zoned and/or resorbed. Some orthopyroxenes remain colorless in plane-polarized light, which could be due to higher iron content. The same feldspar/phlogopite mineral fill that are seen in the basaltic andesites are also observed in the andesites, but in a much smaller number and volume. In addition, sparse xenocrysts are observed in andesite thin sections. Major xenocrysts include an anhedral and partially resorbed alkali feldspar that is 0.6 mm in length (Fig. 3.14c), and two plagioclase crystals with full reaction rims that together are 0.64 mm (Fig. 3.14f).

Lava Mountain Dacites

The most silica-rich samples collected at Lava Mountain are dacitic (Fig. 3.12), Similar to the andesites described above that have intersertal groundmass, these vitrophyric rocks are black and appear glassy in hand specimen, although sparse individual grains can be identified with a hand lens. Petrographically, their texture is clearly intersertal, as glass makes up only about 15% of the rock. Vesicles in hand sample are filled with white zeolite crystals. In thin section, trachytic plagioclase is apparent in the groundmass. The dacites are dominated by groundmass because the collected samples are vitrophyric (~96-97% modally) and both samples contained fewer than 2% phenocrysts. The majority of trachytic groundmass plagioclase has a swallowtail texture in thin section. Thin section textures include extremely rounded and resorbed plagioclase phenocrysts averaging between 0.40-0.60 mm (<2% modally) (Fig. 3.15 a,c,d) and one sparse clinopyroxene averaging 1.8 mm across and 0.025 mm in length, rimmed by few oxides and additional high bifringence clinopyroxene (<1% modally) (Fig. 3.15b).

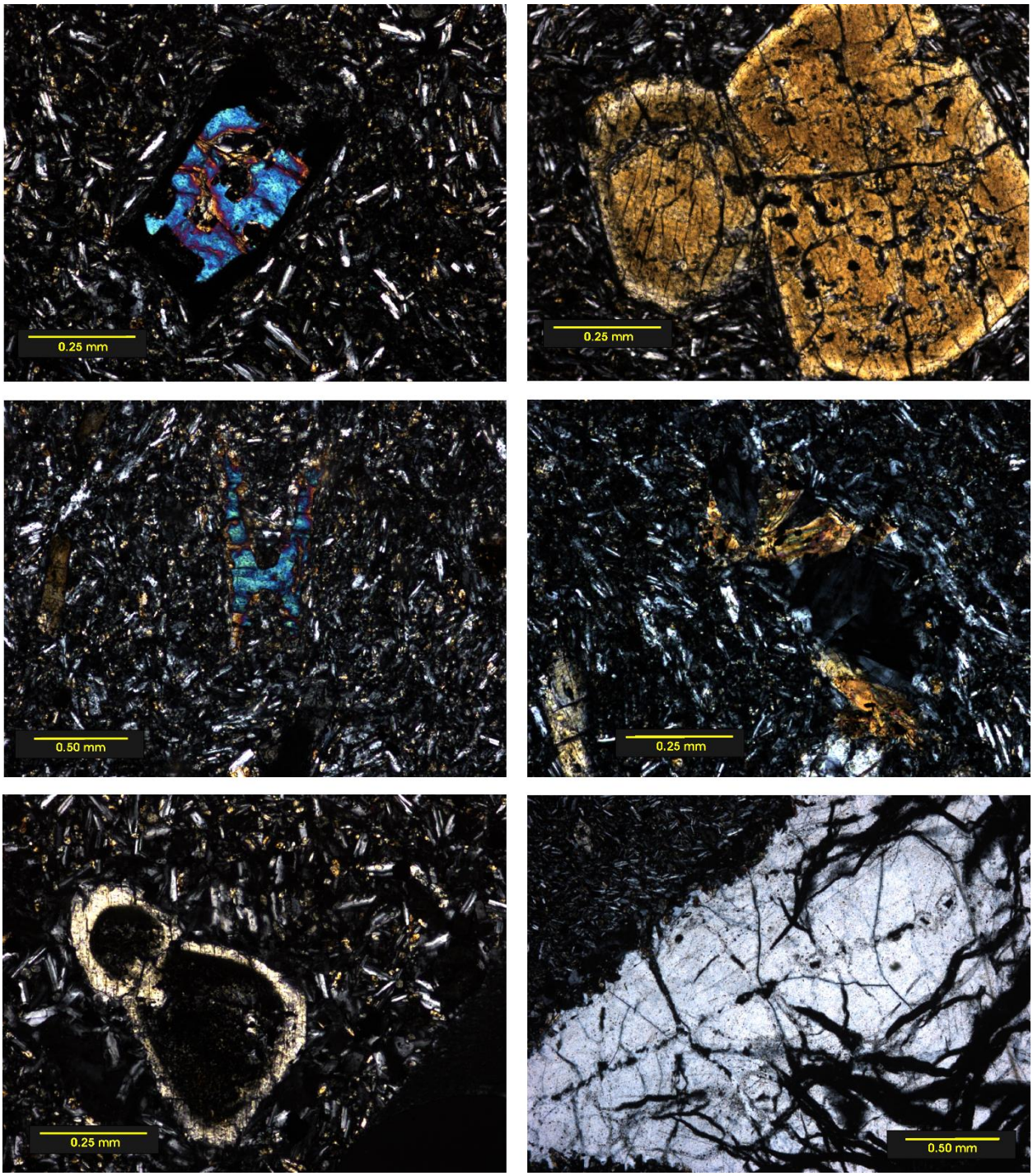

Figure 3.13 Lava Mountain basaltic andesite thin sections. A) Skeletal olivine with oxide rim in basaltic andesite AD14-17; B) Sieved and zoned orthopyroxene in basaltic andesite AD14-15; C) Skeletal olivine in equilibrium, AD14-11; D) Vesicle surrounded by plagioclase laths, AD14-11; E) Extremely resorbed orthopyroxene in AD14-17; F) Severely fractured quartz xenocryst, AD14-14

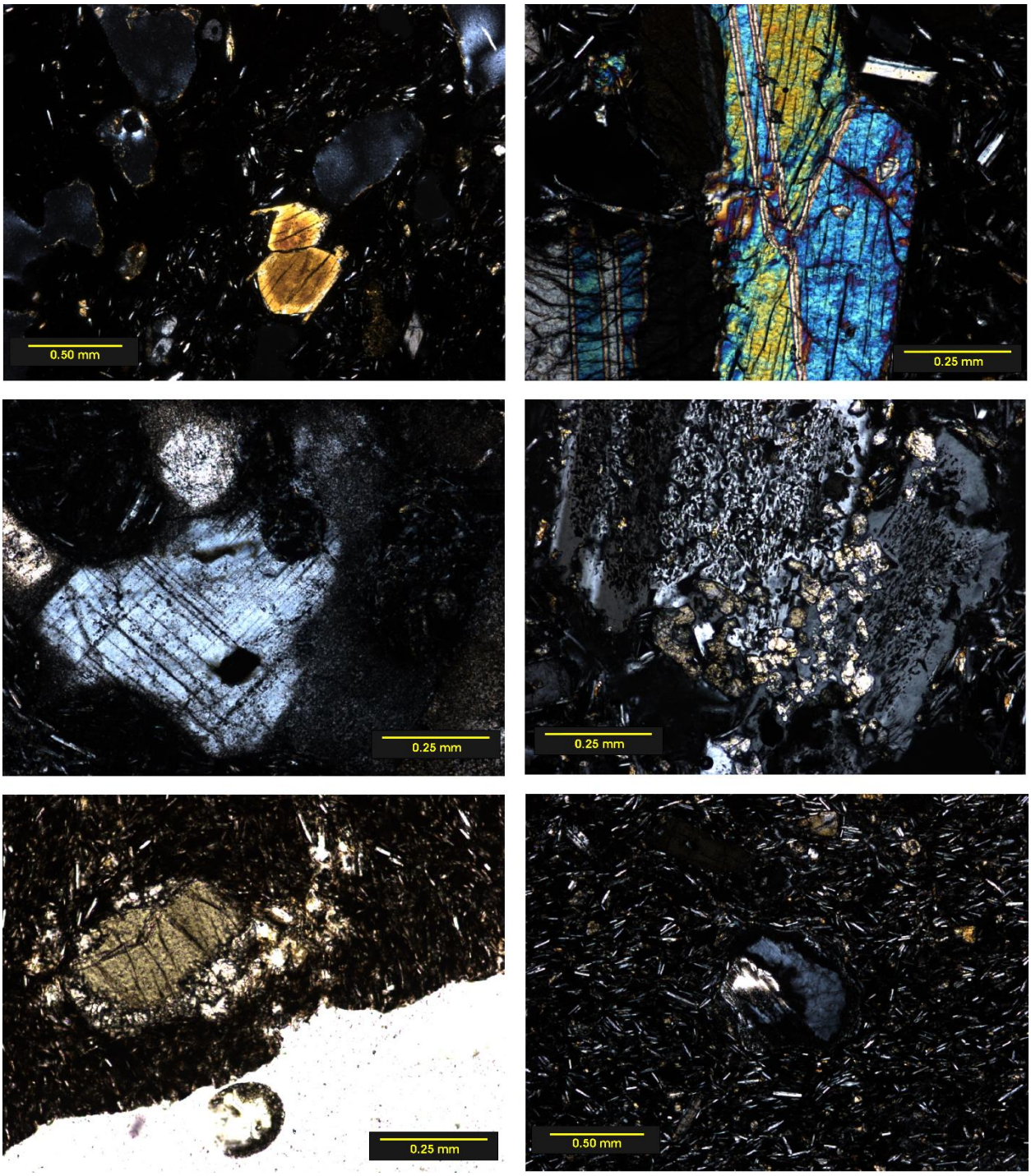

Figure 3.14 Lava Mountain andesite thin sections. A) Zoned orthopyroxene surrounded by vesicles in AD14-4 scoria; B) Clinopyroxene clots in platy andesite AD14-5; C) Alkali feldspar xenolith in AD14-7 andesite; D) Sieved plagioclase with pyroxene inclusions in andesite, MB13-1; E) PPL image of orthopyroxene with pyroxene halo exhibiting deep green pleochroism, AD14-16; F) Plagioclase xenocryst in AD14-6 indicated by red arrow.

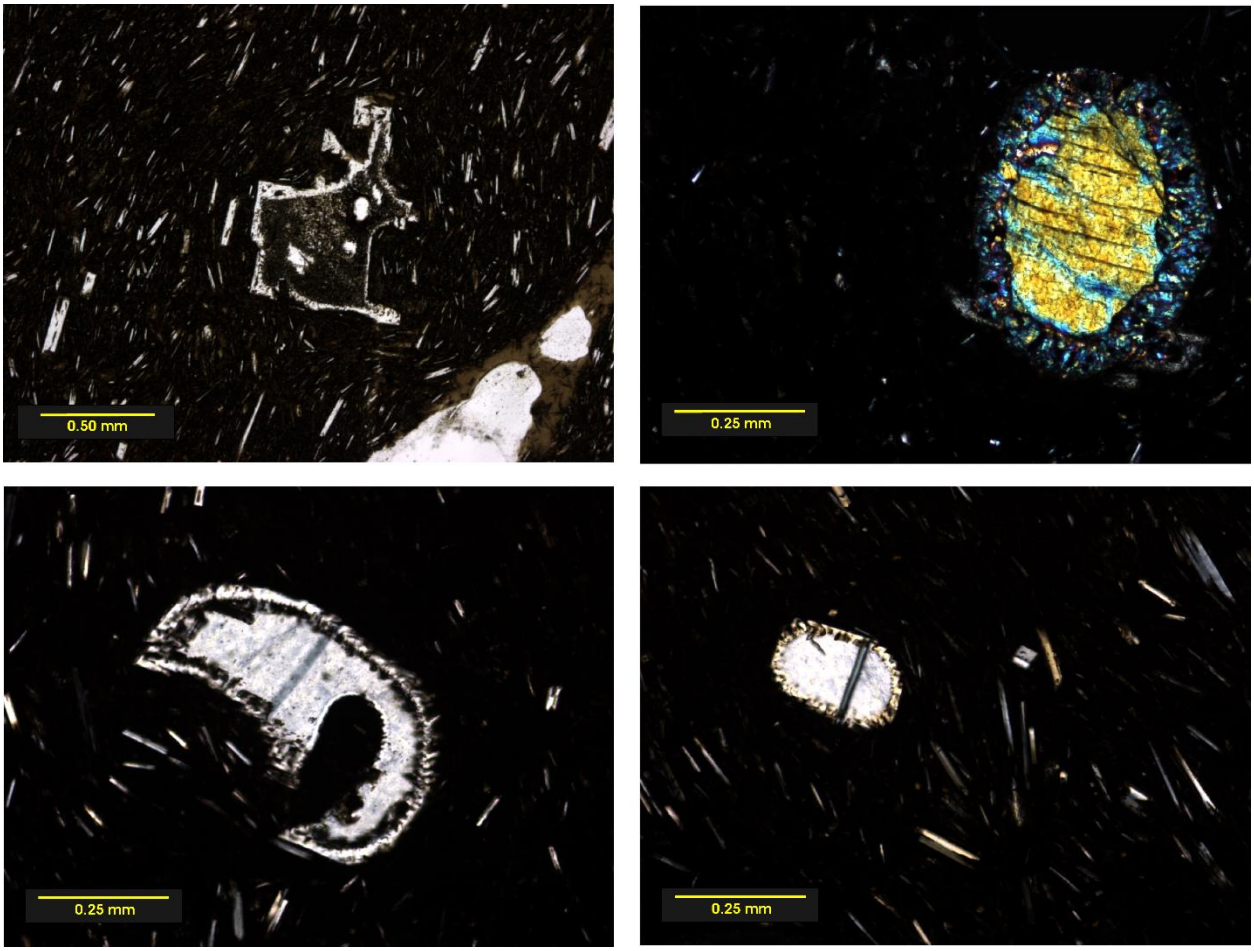

Figure 3.15 Lava Mountain dacite thin sections A) Anhedral and resporbed feldspar in AD14-12; B) Clinopyroxene with corona of pyroxene in AD14-10; C) Resorbed plagioclase crystals in AD14-10 and; D) AD14-12

Spring Mountain Basalts

The basalts are exposed in several parts of the field area, including both on topographic highs and downslope toward Dubois. Most lavas are concentrated to the south, with basalts exposed (Keefer, 1955). Although all of the material sampled at Spring Mountain is basaltic, there is some textural variation among the sample locations. Coarse-grained samples average 0.25-0.50 mm olivine phenocrysts and is approximately 50% vesicles in hand sample. The fine grain variety, MB13-4B, is porphyritic with an aphanitic groundmass, olivine phenocrysts that average 0.5 mm, and almost no vesicles. In hand sample, olivines appear highly iridescent.

In thin section, Spring Mountain basalts are primarily holocrystalline, with subhedral to euhedral olivine phenocrysts in a fine-grained groundmass that averave 0.02-0.05 mm in size (Fig 3.16f). Olivine is observed in both the groundmass and as phenocrysts for all samples. It is common to find euhedral, resorbed (Fig 3.16e), and skeletal olivines (Fig 3.16b) in the same Spring Mountain thin section for all samples. Some olivines are skeletal and surrounded by oxides. These olivines most likely originated in a separate melt where another composition was subsequently introduced, leading to the olivines no longer being in equilibrium. There are other olivines in Spring Mountain basalts that are skeletal with iddingsite rims. These olivines originated in the melt and cooled quickly. Plagioclase demonstrates a trachytic texture in the groundmass. Poikilitic (Fig 3.16c), ophitic (Fig. 3.16a), and subophitic textures are abundant with plagioclase enclosing both clinopyroxene and olivine in one clot (Fig 3.16d). Clinopyroxenes are smaller than olivines, averaging only 0.01-0.013 mm in size. All Spring Mountain samples contain vesicles 1-13% modally, although this may be an underestimate for MB13-4A.

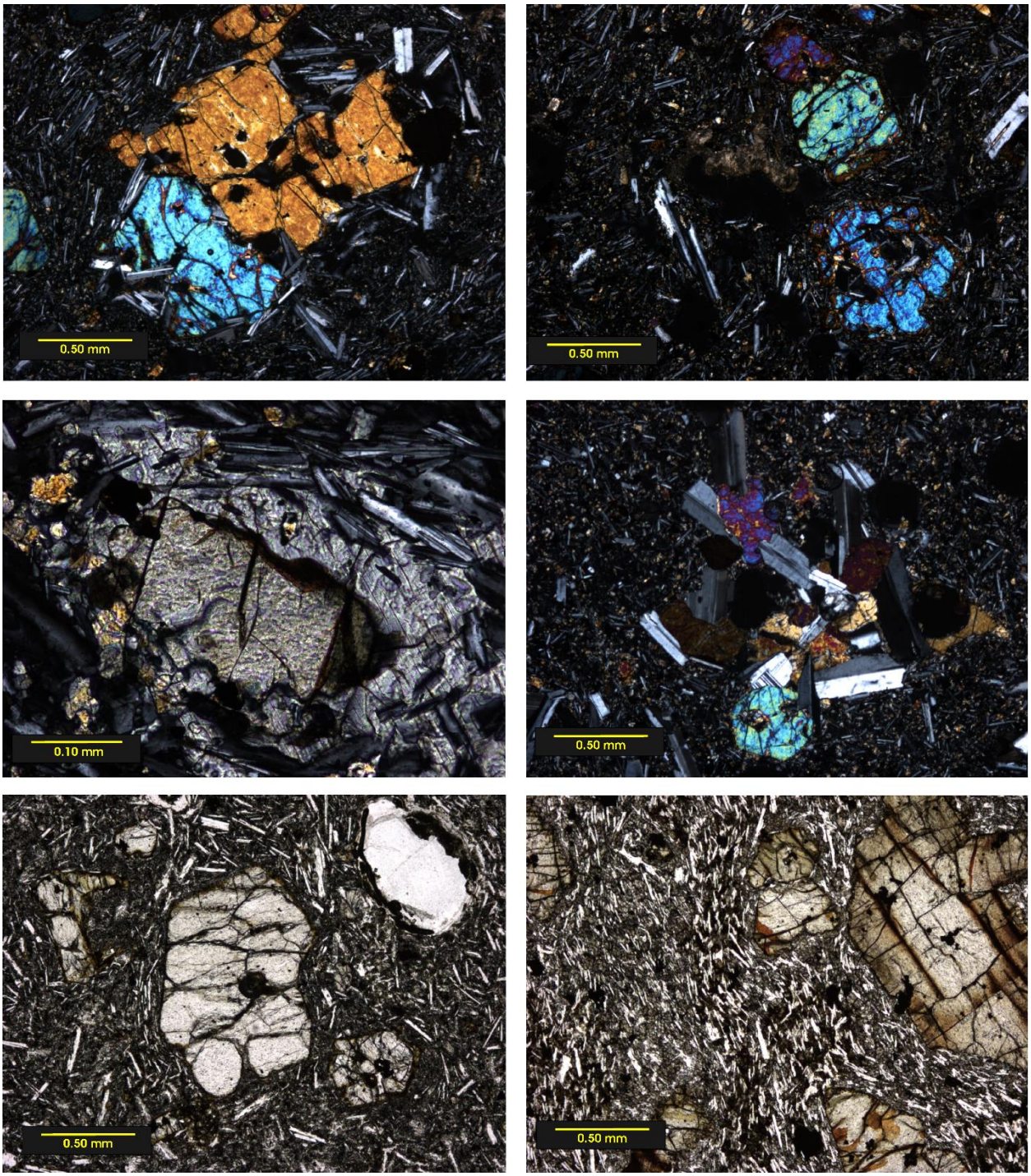

Figure 3.2 Spring Mountain Thin Sections A) Plagioclase laths surrounding olivine phenocryst in vesicular basalt, MB13-3; B) Olivine phenocrysts, one skeletal in equilibrium, surrounded by vesicles, MB13-3; C) Poikilitic texture of olivine crystal in MB13-4A with an orthopyroxene and skeletal olivine in fine-grained sample; D) Subophitic texture in coarse-grained variety MB13-4B; E) PPL image of partially resorbed olivines in AD14-1; F) PPL image of iddingsite around olivine rims and within fractures in AD14-2.

Evidence for Open System Processes

Evidence for open-system petrogenetic processes in the generation of the Lava Mountain andesites is the presence of abundant disequilibrium textures in thin section (e.g., the high percentage of sieved and resorbed crystals). Indeed, nearly every thin section studied contains phenocrysts with sieve textures, especially orthopyroxene (Fig. 3.13b, e), indicating these crystals were not in equilibrium with the melt that brought them to the surface. Dacites contain highly resorbed feldspars (Fig. 3.15a, c, d). Basaltic andesites contain a range of olivine morphologies. Some are skeletal (Fig. 3.13c), but many have been partially replaced with oxide minerals (Fig. 3.13a), indicating that these olivines were not in equilibrium with the host basaltic andesite. Xenocrysts include alkali feldspar in andesite (Fig. 3.14c) and quartz in basaltic andesite (Fig. 3.13f). Similar open system textures are present in some Spring Mountain olivines (Fig. 3.16a, b, e).

Chapter 4 - Geochemistry and Isotope Characteristics

For geochemical analysis, all twenty-two samples collected during summer 2014 were used (Lava Mountain, Spring Mountain, Pilot Knob, Crescent Mountain, Wildcat Hill), as well as the five collected from summer 2013 (Lava Mountain and Spring Mountain) and the eighteen provided by Dave Adams are discussed. For this study, only Lava Mountain and Spring Mountain results will be described in detail; the data for other localities are used here for comparative purposes. Major elements are reported as weight percent (wt. %) and trace elements as ppm (parts per million); all analyses are reported as anhydrous. A Table of select sample results is listed in Table 4.2. The data set for this study is reported in Appendix B.

Major Element Geochemistry of Lava Mountain Extrusives

Rocks found on Lava Mountain plot from basaltic andesite to dacite on a total alkali vs silica diagram (Fig. 3.12); SiO_2 ranges between 55.50% - 62.80 wt. % and averages 58.01 wt. %. They follow a calc-alkaline trend on an AFM diagram (Fig. 4.1). Harker diagrams (Fig. 4.2) show major element trends with SiO_2. CaO ranges from 5.65 - 10.38 wt. %, FeO from 6.09 - 7.44 wt. %, MnO from 0.09 – 0.13 wt. %, P_2O_5 from 0.21 – 0.28 wt. % and MgO from 2.24 - 6.64 wt.%. All decrease with increasing silica. Na_2O ranges from 2.76 - 3.35 wt. % and K_2O from 1.64-2.00 wt. %. Both increase with increasing silica. Al_2O_3 ranges from 15.15 – 16.02 wt.%, and TiO_2 from 0.79 - 0.92 wt. %. No trend is observed with silica against Al_2O_3, TiO_2, and Fe_2O_3. Mg # ranges from 39.5 - 61.6. LOI values range from 0.1 - 4.2. Samples with the highest MgO were found near the base of the volcano and are basaltic andesites. Those with the highest SiO_2 values are vitrophyric dacite in hand sample, from one basal lava that is also found near the stratigraphic base of the volcano. Therefore, both the most silica-rich and silica-poor samples crop out at the base. Although there are smaller chemical and textural differences between flows, about 4.56 km^3 plots as andesite on a total alkali silica diagram (Fig. 3.12).

Fig. 3.1 outlines the general stratigraphy of Lava Mountain as a whole. From the bottom of the volcano until about 2774 m, the lavas are diverse chemically. Basaltic andesite is interstratisfied with dacite. Above 2774 m, the compositional range is more limited.

Major Element Geochemistry of Spring Mountain Basalts

Spring Mountain rocks plot as subalkaline basalt on a total alkali vs silica diagram,

averaging ~50 wt% SiO_2 (Fig. 3.12). An AFM diagram shows they are tholeiitic rather than calc-alkaline (Fig. 4.1) and they are classified as olivine tholeiites via their normative mineralogy. TiO_2 ranges from 0.71 – 0.92 wt.%, Fe_2O_3 from 1.65 – 3.03 wt.%, FeO from 5.93 – 7.35 wt.%, MnO from 0.15 – 0.15 wt.%, MgO from 7.7 – 11.8 wt.%, CaO from 10.38 – 11.34 wt.%, Na_2O from 1.98 – 2.27 wt.%, K_2O from 0.45 – 0.61 wt.%, and P_2O_5 from 0.16 – 0.20 wt.%. Mg # ranges from 60.8 – 69.9. LOI values range from 0.69 – 1.26. Major elements show no obvious correlation with SiO_2 (Fig. 4.2). Compared to Lava Mountain samples, Spring Mountain samples on average show higher concentrations of FeO, MnO, MgO, CaO, lower concentrations of SiO_2, TiO_2, Al_2O_3, Na_2O, K_2O, and about equal Fe_2O_3.

Trace and Rare Earth Element Analysis

For Lava Mountain, select trace and REE ranges are as follows: Ni 12 – 119 ppm; Cr 26 – 308 ppm; Sc 16.1 – 24.8; V 132 - 173 ppm; Ba 1134 – 1571 ppm; Rb 19 – 38 ppm; Sr 541 – 759 ppm; Zr 152 – 200 ppm; Y 21 – 29 ppm; Nb 8.5 – 17.8 ppm; La 54.5 – 48.5 ppm; Ce 97.4 – 107.9 ppm; Pr 10.68 - 11.95 ppm; Nd 38.44 - 42.99 ppm; Sm 6.69 – 7.69 ppm; Eu 1.66 – 1.77 ppm; Lu 0.33 – 0.35 ppm.

Spring Mountain basalt select trace and REE ranges are as follows: Ni 95 – 322 ppm; Cr 255 – 977 ppm; Sc 28.0 – 30.5 ppm; V 180 – 231 ppm; Ba 412 – 544 ppm; Rb 4 – 11 ppm; Sr 391 – 490 ppm; Zr 81 – 105 ppm; Y 17 – 25 ppm; Nb 3.8 – 6.0 ppm; La 23.1 – 30.1 ppm; Ce 45.2 – 58.8 ppm; Pr 5.11 – 6.41; Nd 18.23 – 22.93 ppm; Sm 3.70 – 4.36 ppm; Eu 1.03 – 1.24 ppm; Lu 0.25 – 0.29 ppm. Aside from major differences in Ni and Cr that are accounted for based on modal olivine, the basalts are nearly geochemically identical; the only exception being MB13-4B, which has slightly lower Mg, Fe, with higher V, Zr, and Sr.

Unlike Spring Mountain, where all samples are basaltic, three specific rock types are identified on Lava Mountain: basaltic andesites, andesites, and dacites. These three rock types can be distinguished from one another by their trace element concentrations (Fig. 4.3).

Lava Mountain dacites have the lowest overall Ni (<12 ppm) and Cr (<27 ppm) concentrations, which contrasts strongly with the basaltic andesites which have Ni concentrations >115 ppm and Cr concentrations exceeding 240 ppm. Overall, compatible elements Cr, V, Co, Sc, and Ni all decrease with silica, as expected. Positive correlations are observed between Sc, Ni, and Cr, suggesting clinopyroxene fractionation. The dacites have the lowest Rb, Nb, Sc, Cu, and Co

concentrations of the three groups. The basaltic andesites have the lowest concentrations of Y (<9 ppm) and Pb (<18 ppm).

All Lava Mountain REEs show a small increase in concentration against SiO_2, which is consistent with fractional crystallization of phases excluding REEs (Fig. 4.4). Multi-element diagrams show the suite is depleted relative to MORB in HREE (Fig. 4.5). A MORB-normalized multi-element diagram also reveals enrichment in the incompatible elements Ba, Th, Ce, Sm, and Y, with relative depletions in Rb, Nb, and Ti for both Lava Mountain and Spring Mountain samples. The observed relative depletions in Nb and Ti for Lava Mountain and Spring Mountain are reminiscent of island-arc basalts or for basalts derived from lithospheric mantle enriched by prior subduction processes (Kempton et al. 1991). Primitive-mantle-normalized diagrams show similar relative enrichments in Ba, Th, Ce Pb, Nd, and Sm, along with relative depletions in Nb, P, and Ti (Fig. 4.6). Compared to a typical OIB, the Spring Mountain thoeiites are very similar, and are enriched in LILEs, LREEs. However, Spring Mountain basalts are depleted in HFSE, indicating a subduction influence on the area. A REE diagram normalized to chondrites shows all samples are enriched in LREE with flat patterns for HREE (Fig. 4.7). Such LREE enrichment and flat HREE in relatively primitive rocks (e.g., basalt) is typically attributed to partial melting in the presence of spinel peridotite, where clinopyroxene controls the distribution of HREEs. The degree of LREE enrichment is also consistent with melting of LREE-enriched, lithospheric mantle.

Radiogenic Isotope Results

$^{87}Sr/^{86}Sr$ values for Lava Mountain rocks range from 0.70700 to 0.70751. The Spring Mountain sample (which one- state sample number) analyzed has a lower $^{87}Sr/^{86}Sr$ value than Lava Mountain rocks at 0.70608. The Crescent Mountain sample has the highest $^{87}Sr/^{86}Sr$ value at 0.70883. All rocks analyzed have $^{143}Nd/^{144}Nd$ ratios ranging from 0.51149 to 0.51169. The highest εNd value is the Spring Mountain basalt (-18.3) and the lowest is the Crescent Mountain basalt (-22.2). Such low εNd values are associated with ancient cratons. For example, the Archean Wyoming craton and cratonic lithospheric mantle in North America has εNd values less than -20 (Leeman, 1985; Downes et. al., 2004). Lava Mountain andesites and basaltic andesites decrease linearly with $^{143}Nd/^{144}Nd$ as $^{87}Sr/^{86}Sr$ values increase (Fig. 4.8). For comparison, $^{143}Nd/^{144}Nd$ isotope ratios for Yellowstone and SRP olivine thoeiites range from 0.51237 to 0.51250, while Sr values range from 0.7058-0.7078 (Menzies, et. al., 1983). The Yampa volcanics, a series of late

Miocene to Quaternary alkaline eruptions of basanite, trachybasalt, and basalt dating from 6-4.5 Ma, have isotopic signatures from a Proterozoic subcontinental lithospheric mantle source. They have similar isotopes to rocks of the Green Mountain arc terrane, which is a Proterozoic subduction zone complex that extends from Colorado into southwest Wyoming. The Yampa rocks have slightly lower Sr and higher Nd ratios compared to the UWRB, as $^{87}Sr/^{86}Sr$ values for the Yampa rocks range from 0.70414-0.70517, and $^{143}Nd/^{144}Nd$ values range from 0.51233-0.51256 (Cosca, et. al., 2014). Additionally, the Leucite Hills lamproites isotopically represent a lithospheric mantle source origin that has undergone stages of both depletion and enrichment. Isotope values for the Leucite Hills are more compatible to UWRB rocks than the Colorado Yampa volcanics. $^{87}Sr/^{86}Sr$ values for the Leucite Hills lamproites range from 0.70534-0.70608, and $^{143}Nd/^{144}Nd$ values range from 0.51178-0.51211 (Mirnejad and Bell, 2006).

Lava Mountain samples are slightly more radiogenic than Spring Mountain samples. Pb isotope ratios for Lava Mountain plot as $^{206}Pb/^{204}Pb$ = 16.34-16.46, $^{207}Pb/^{204}Pb$ = 15.41 – 15.42, and $^{208}Pb/^{204}Pb$ = 37.21 – 37.66. Spring Montain values plot as $^{206}Pb/^{204}Pb$ = 16.39, $^{207}Pb/^{204}Pb$ = 15.41, and $^{208}Pb/^{204}Pb$ = 37.64. Pb isotope ratios for all samples studies plot to the left of the 4.65 Ga geochron, but above the Stacey and Kramers growth curve. Typically, plotting to the left of the Geochron is often interpreted as evidence for either direct interaction with ancient lower crust or derivation from ancient lithospheric mantle. Furthermore, all samples plot along a 2.8 Ga Beartooth isochron representative of when this portion of the Wyoming Craton stabilized (Wooden and Mueller, 1988; Hanan, Shervais, and Vetter, 2008) (Fig. 4.9) Crescent Mountain has the most radiogenic Pb isotope composition for all three isotope ratios, at $^{206}Pb/^{204}Pb$ = 16.51, $^{207}Pb/^{204}Pb$ = 15.46, and $^{208}Pb/^{204}Pb$ = 38.29 . Interestingly, the Spring Mountain basalt plots within the field of Lava Mountain rocks and thus does not form a compositional end member in Pb isotope space, as suggested by most of the major and trace element data (Fig. 4.10). It does not plot within the field of Lava Mountain and Spring Mountain rocks in $^{87}Sr/^{86}Sr$ and $^{143}Nd/^{144}Nd$ isotope space. For comparison, Colorado Yampa alkaline volcanics have Pb isotopes values of: $^{206}Pb/^{204}Pb$ = 17.516-17.998, $^{207}Pb/^{204}Pb$ = 15.439-15.513, and $^{208}Pb/^{204}Pb$ = 37.309-37.612. The Leucite Hills lamproites have isotope ratios of $^{206}Pb/^{204}Pb$ = 17.182-17.583, $^{207}Pb/^{204}Pb$ = 15.459-15.508, and $^{208}Pb/^{204}Pb$ = 37.130-37.523.

Microprobe Analysis

Slide	Olivine #	Fo	Fa
MB-13-4a	Ol1-1	77.7	21.7
MB-13-4a	Ol1-2	74.4	24.9
MB-13-4a	Ol4-2	74.0	25.3
MB-13-4a	Ol4-1	78.9	20.6
MB-13-4a	Ol2-1	82.8	16.8
MB-13-4a	Ol3-2	74.0	25.3
MB-13-4a	Ol5-1	78.1	21.3
MB-13-4a	Ol2-2	76.0	23.5
MB-13-4a	Ol5-2	73.4	25.9
MB-13-4a	Ol3-1	79.5	19.9
MB13-3	Ol6-1	88.7	10.9
MB13-3	Ol8-2	89.1	10.5
MB13-3	Ol7-1	89.4	10.2
MB13-3	Ol9-2	89.4	10.1

Table 4.1 Olivine microprobe analysis results from two separate Lava Mountain polished thin sections, both from 2013.

Olivines analyzed in MB13-3 had higher Mg values than those in MB13-4a. MB13-3 is a vesicular basalt collected from one of the vents at Spring Mountain, whereas MB13-4a is a fine-grained basalt found adjacent to another fissural vent. MB13-4a has a much larger range of fosterite values than MB13-3, ranging from 73.4 to 82.8 over various crystals. MB13-3 fosterite values exhibit a small range of 88.7 to 89.4. The average forsterite value for MB13-4a is 76.9, where the average for MB13-3 is 89.1. Olivines that are Mg-rich, such as those found in MB1-3, are typical of mantle peridotite. In thin section, several Spring Mountain olivines are euhedral with very little evidence of alteration. The most Mg-rich olivines, however, are subhedral to anhedral and this, coupled with their Mg-rich compositions, suggest these olivines are xenocrystic.

Sample	AD14-4	AD14-9	AD14-10	AD14-14	AD14-17	MB13-3
Unit	Lava Mtn.	Lava Mtn.	Lava Mtn.	Lava Mtn.	Lava Mtn.	Spring Mtn.
Type	Andesite Scoria	Andesite	Dacite	Basaltic Andesite	Basaltic Andesite	Basalt
SiO2	58.06	57.94	62.35	55.70	55.29	50.23
TiO2	0.79	0.88	0.89	0.83	0.84	0.71
Al2O3	15.60	15.91	15.97	15.66	15.60	14.44
Fe2O3	7.24	7.66	6.74	8.00	7.99	2.38
FeO	-	-	-	-	-	6.62
MnO	0.11	0.12	0.10	0.12	0.12	0.15
MgO	5.20	4.72	2.27	6.38	6.49	11.41
CaO	7.10	7.25	5.64	8.06	8.04	10.37
Na2O	2.95	3.07	3.33	2.78	2.74	2.01
K2O	1.91	1.72	1.69	1.68	1.65	0.58
P2O5	0.26	0.27	0.21	0.28	0.28	0.17
Total	**99.22**	**99.53**	**99.19**	**99.50**	**99.05**	**100.26**
LOI	0.78	0.47	0.81	0.50	0.95	1.19
Ni	87	69	11	119	115	295
Cr	215	126	27	264	271	955
Sc	21.1	21.8	16.4	24.8	24.8	28
V	146	160	127	170	169	210
Ba	1481	1520	1141	1571	1563	544
Rb	33	22	21	22	22	10
Sr	633	759	600	666	666	430
Zr	178	166	176	154	155	95
Y	23	22	23	21	21	25
Nb	14.7	16.7	8.7	18.7	18.5	4.2
Ga	-	-	-	-	-	14
Cu	34	42	22	37	32	66
Co	28	29	18	33	33	58
Zn	77	79	88	94	77	75
Pb	18	16	17	16	15	14
U	-	-	-	-	-	<0.5
Th	-	-	-	-	-	<0.5
Cs	-	-	-	-	-	-
Hf	-	-	-	-	-	-
Ta	-	-	-	-	-	-
La	54.5	53.2	42.7	49.8	49.9	23.2
Ce	107.9	104.3	85.5	97.7	97.4	45.2
Pr	11.95	11.52	9.73	10.69	10.68	5.13
Nd	43.0	41.5	36.0	38.4	38.4	18.2
Sm	7.69	7.12	6.77	6.77	6.69	3.70
Eu	1.76	1.77	1.79	1.69	1.66	1.04
Gd	5.40	4.95	5.10	4.82	4.76	3.06
Tb	0.86	0.79	0.82	0.78	0.77	0.53
Dy	4.56	4.25	4.48	4.17	4.12	3.04
Ho	0.88	0.78	0.84	0.77	0.80	0.59
Er	2.45	2.30	2.44	2.29	2.25	1.73
Tm	0.34	0.31	0.34	0.31	0.30	0.24
Yb	2.40	2.27	2.41	2.29	2.26	1.72
Lu	0.35	0.33	0.35	0.34	0.33	0.25
$^{87}Sr/^{86}Sr$	0.70723	-	0.70751	-	0.70700	0.70608
$^{144}Nd/^{143}Nd$	0.51157	-	0.51149	-	0.51163	0.51169
epsilon Nd	-20.69	-	-22.15	-	-19.47	-18.32
$^{206}Pb/^{204}Pb$	16.40	-	16.34	-	16.46	16.39
$^{207}Pb/^{204}Pb$	15.42	-	15.41	-	15.42	15.41
$^{208}Pb/^{204}Pb$	37.66	-	37.42	-	37.59	37.64

Table 4.2 Representative raw geochemical and isotopic data from Lava Mountain and Spring Mountain

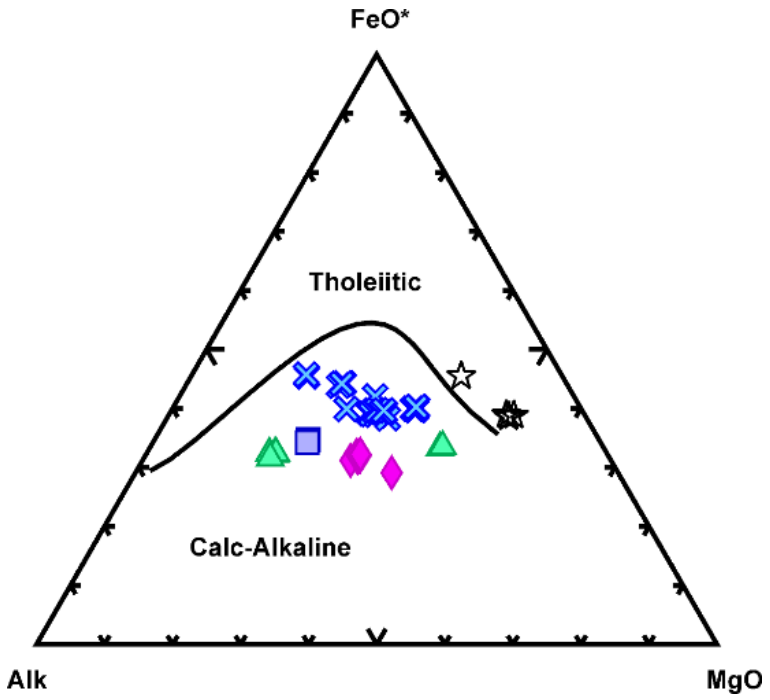

Figure 4.1 AFM diagram. Samples follow a calc-alkaline differentiation trend, though Spring Mountain samples are tholeiitic consistent with their bulk major element chemistry. Basalts are olivine tholeiites.

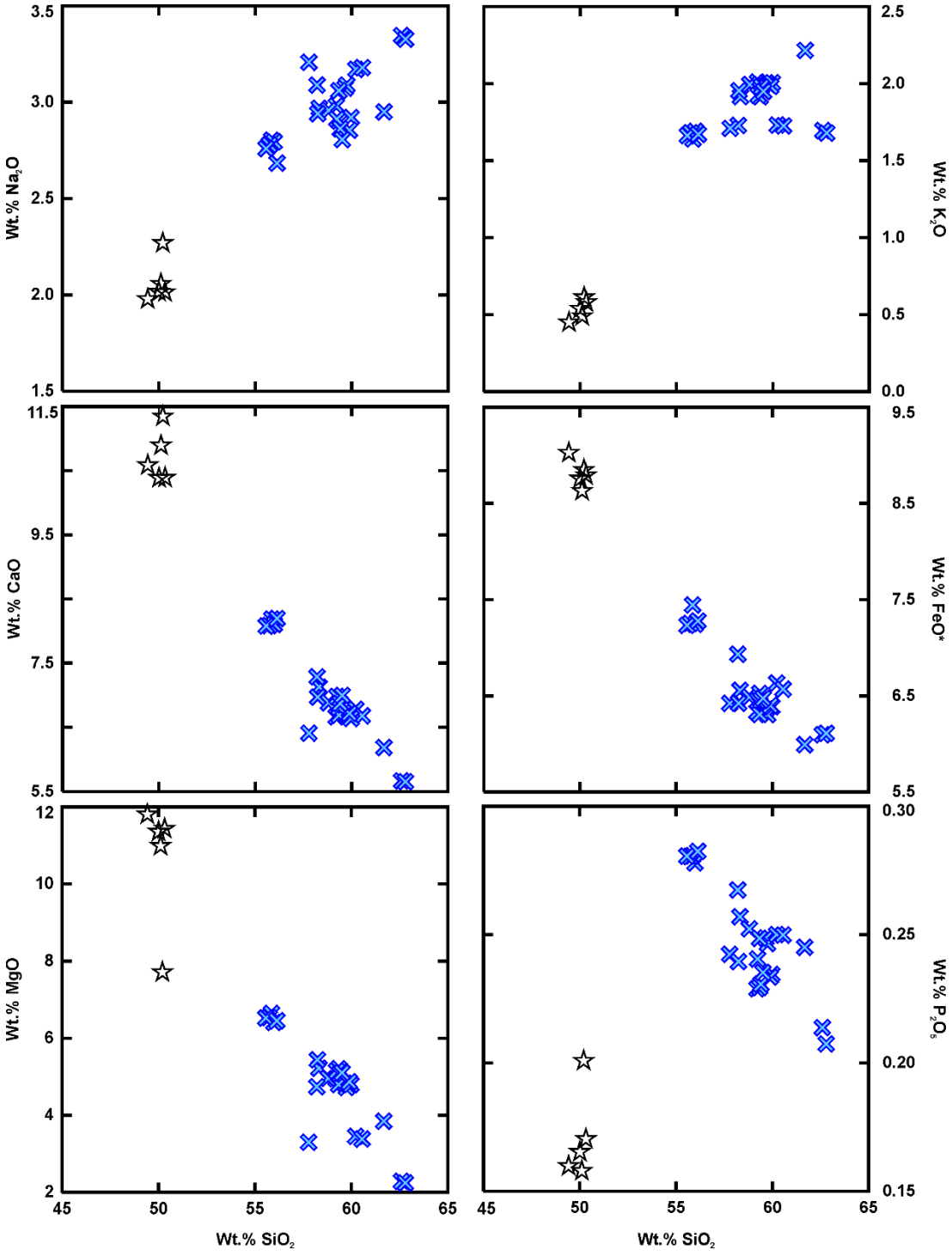

Figure 4.2 Harker diagrams for major element oxides Na_2O, K_2O, CaO, FeO, MgO, and P_2O_5. Na_2O and K_2O increase with silica, while CaO, FeO, MgO, and P_2O_5 decrease with increasing silica on Lava Mountain. The Spring Mountain samples always cluster near the same compositions.

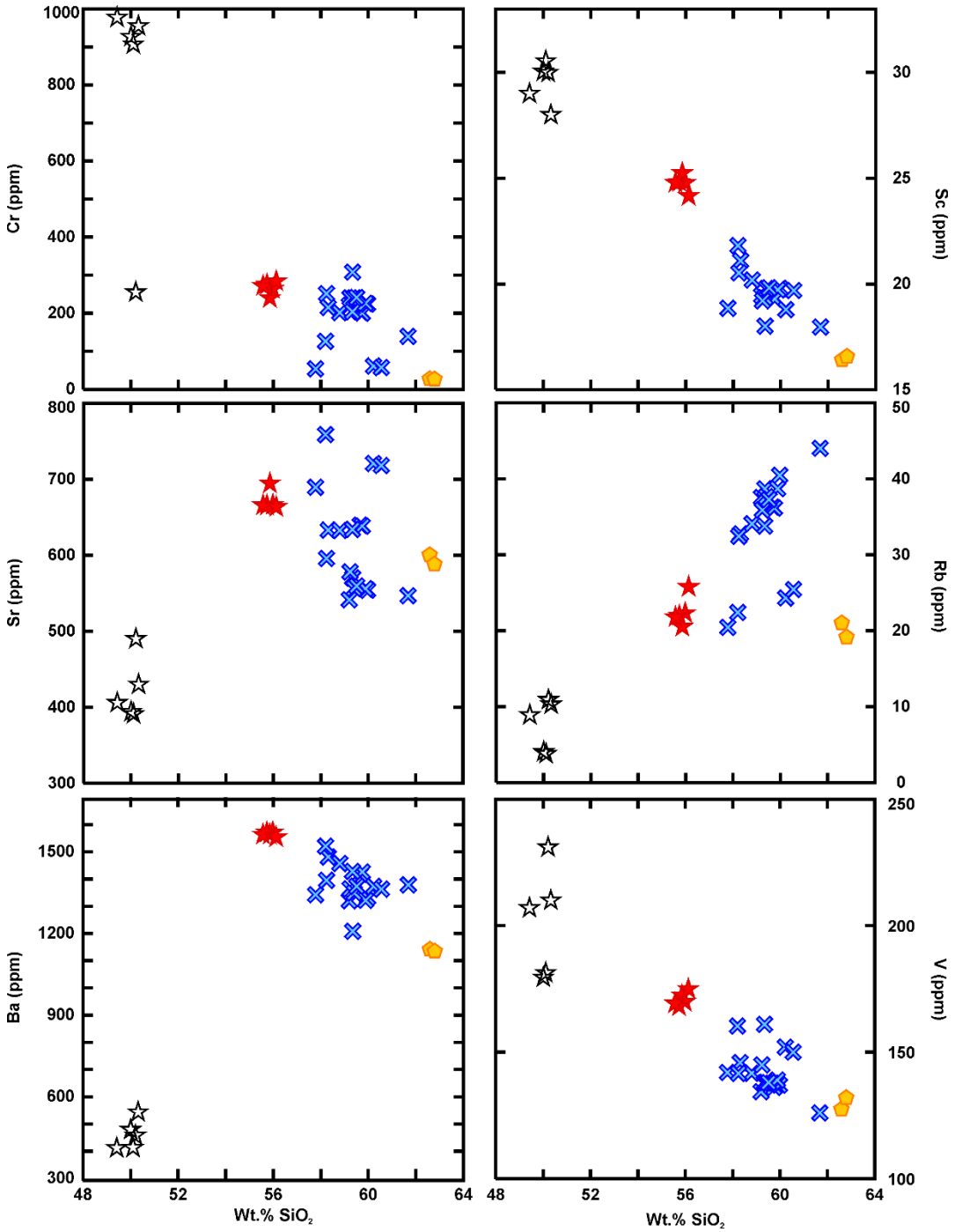

Figure 4.3 Trace elements plotted against SiO_2. Compatible elements Cr, Sc, and V all decrease with increasing silica, while incompatible elements Rb and Nb decrease. Ba decreases as well. In this figure the different Lava Mountain compositional groups are distinguished using different colors to draw out the compositional differences between the three groups. Red stars: LM basaltic andesites, Blue X's: LM andesites, Yellow dots: LM dacites

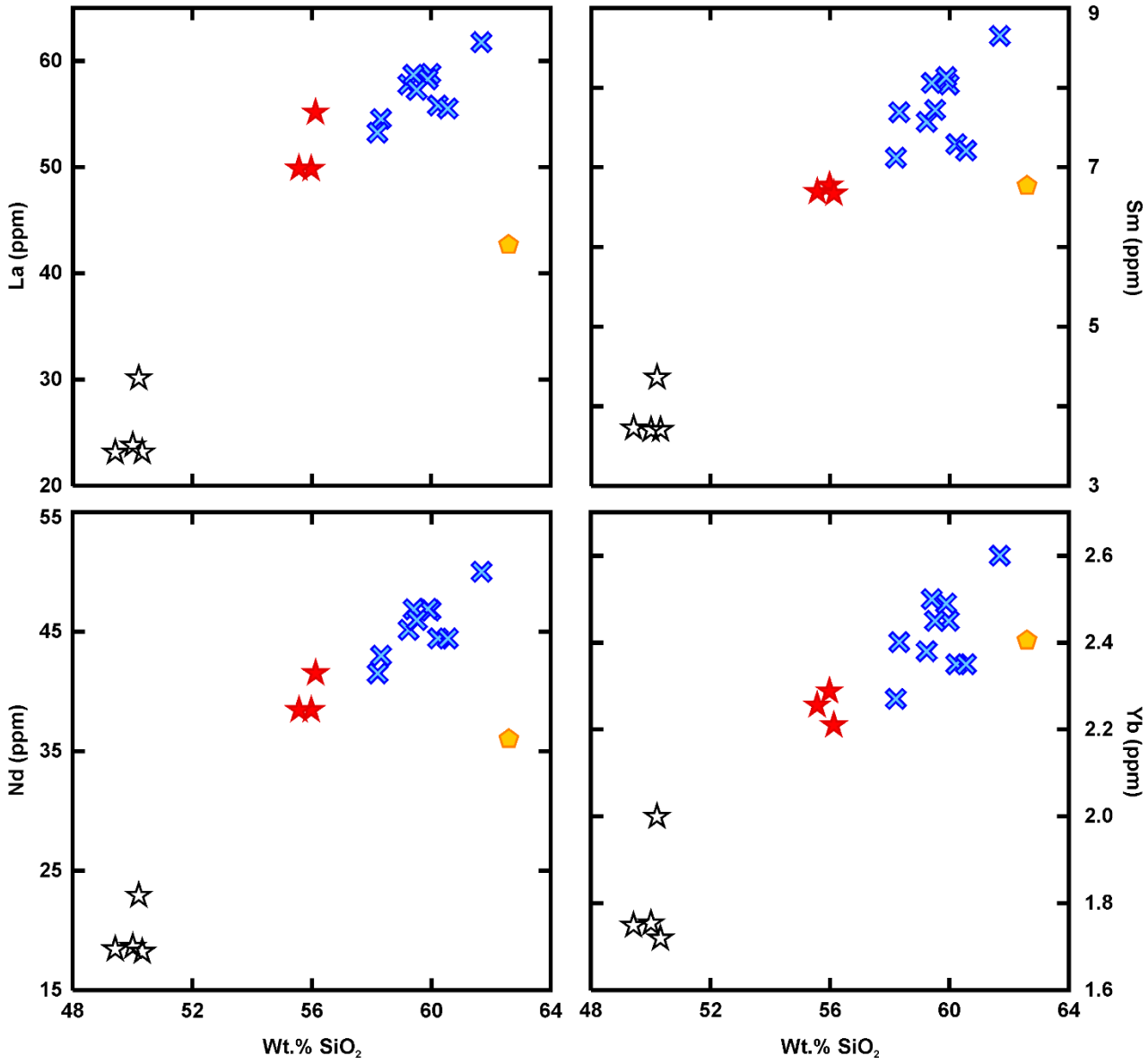

Figure 4.4 Select REE against SiO_2. Red stars: basaltic andesites, Blue X's: andesites, Yellow dots: dacites

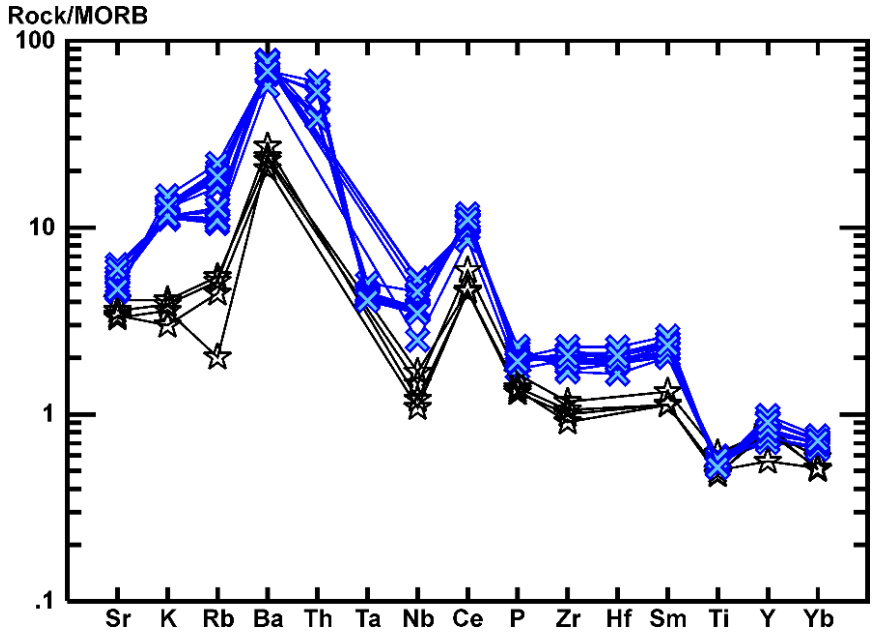

Figure 4.5 Multi-element diagram normalized to MORB, from Pearce 1983.

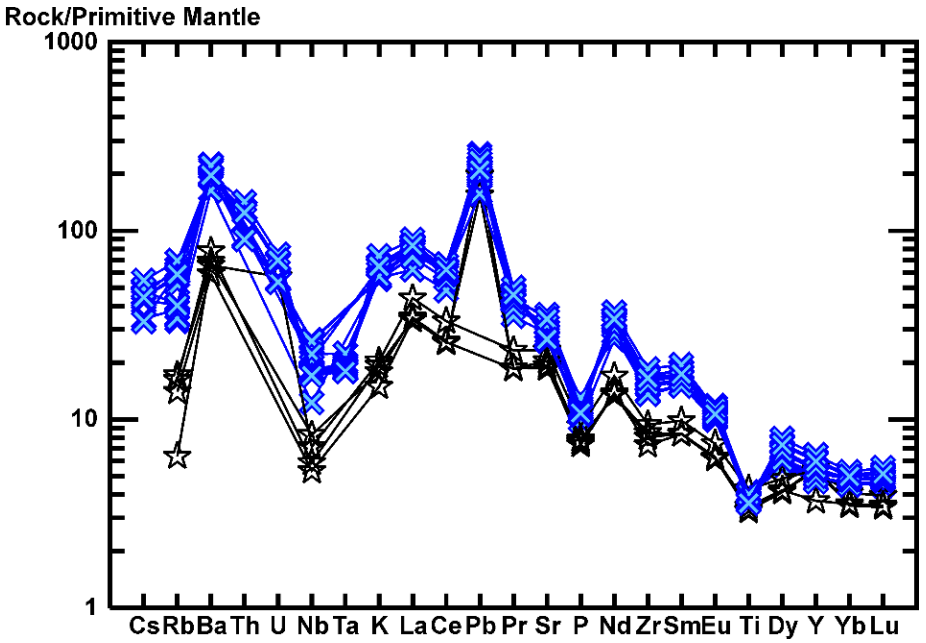

Figure 4.6 Multi-element diagram normalized to primitive mantle, from Sun and McDonough, 1989.

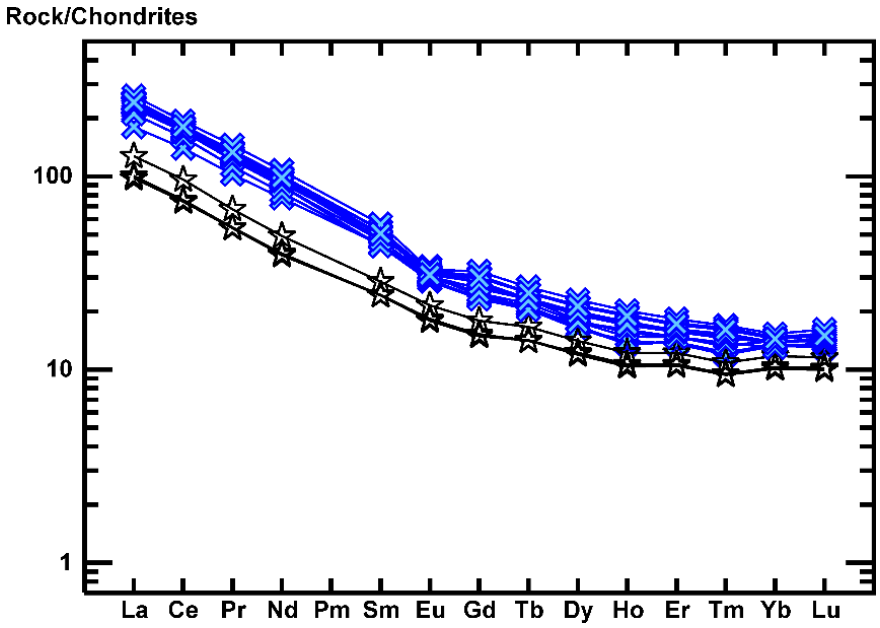

Figure 4.7 Rare Earth Element (REE) diagram normalized to chondrites, from Sun and McDonough, 1989.

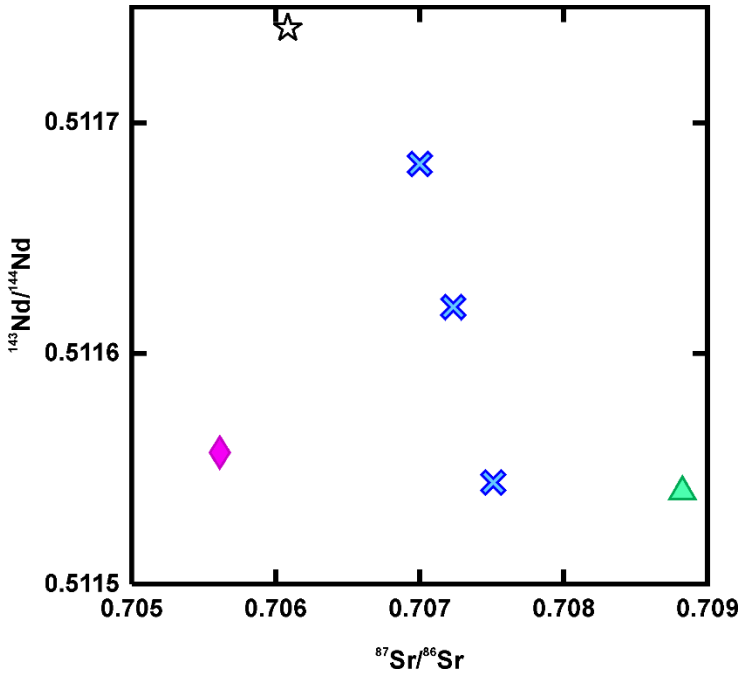

Figure 4.8 $^{87}Sr/^{86}Sr$ vs. $^{143}Nd/^{144}Nd$

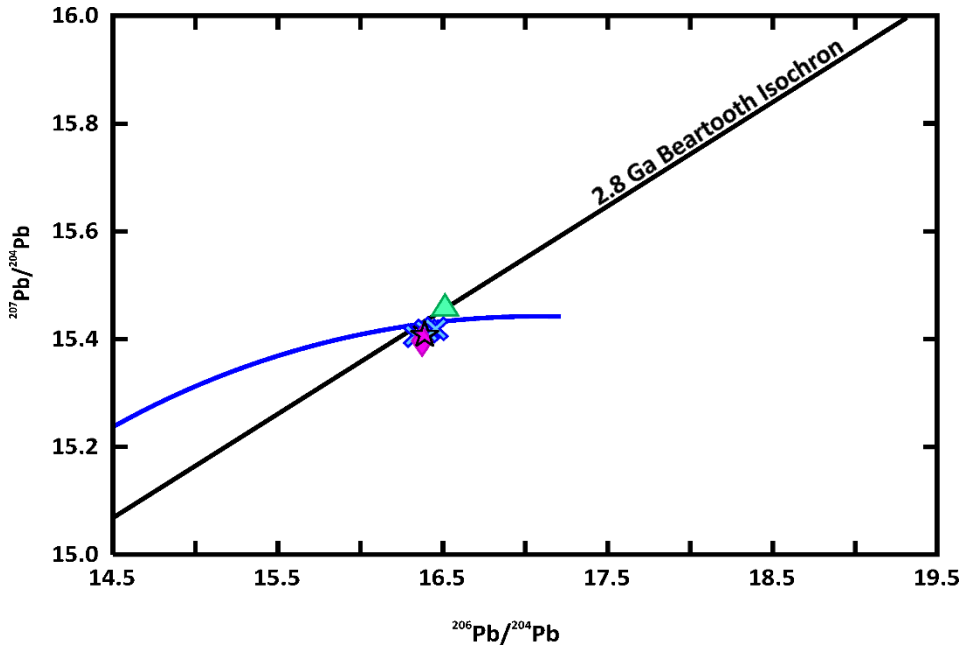

Figure 4.9 $^{207}Pb/^{204}Pb$ vs. $^{206}Pb/^{204}Pb$. UWRB samples plot directly on the 2.8 Ga Beartooth Isochron and directly on the Stacey Kramers growth curve (1975).

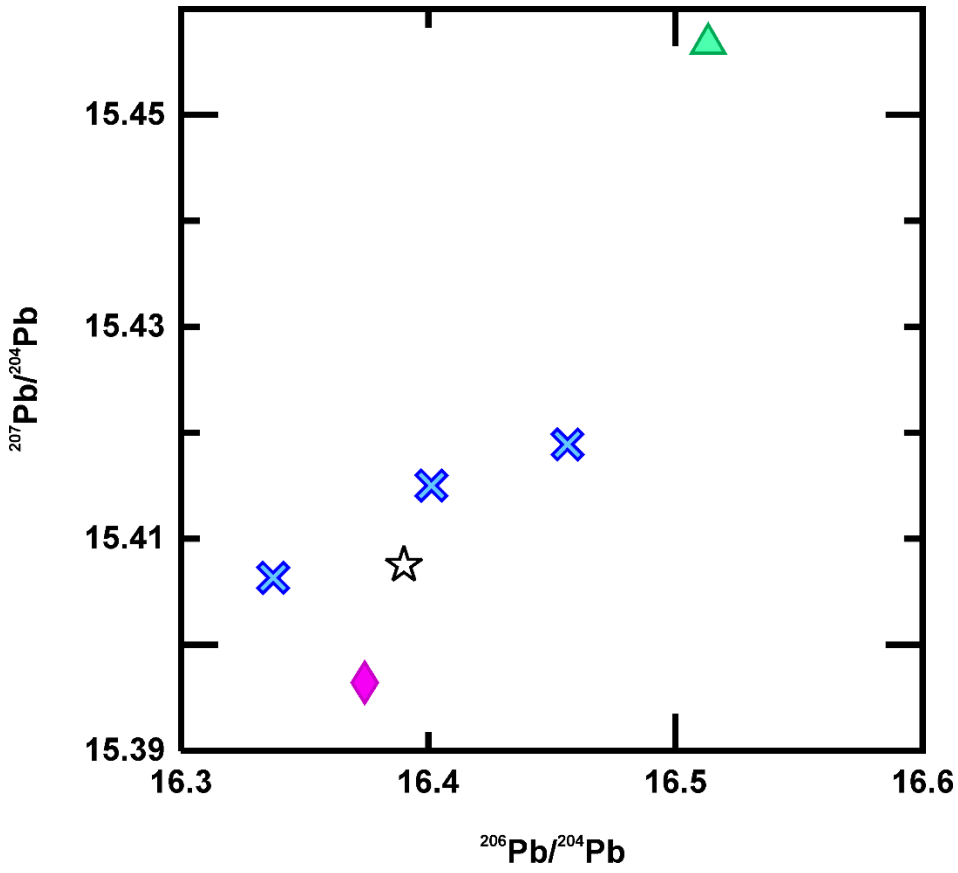

Figure 4.10 $^{207}Pb/^{204}Pb$ vs. $^{206}Pb/^{204}Pb$. Spring Mountain plots among Lava Mountain in Pb isotope space

Chapter 5 - Petrogenetic Modeling

Petrographic evidence argues for open-system magmatic processes at both Lava Mountain and Spring Mountain (e.g., fractional crystallization combined with magma mixing and possible crustal assimilation). Isotopic data suggest that crustal contamination may have been involved, though the isotope results affirm the involvement of Achaean lithospheric mantle. A first-order petrogenetic model has been developed that includes components of both magma mixing and fractional crystallization (FC). This model aims to: [1] account for the generation of basaltic andesite, andesite, and dacite magmas at Lava Mountain and [2] conform to field, petrographic, and geochemical/isotope constraints on magma generation.

For simplicity, Spring Mountain basalt (MB13-4B) is assumed to be the mafic endmember for generation of the Lava Mountain basaltic andesite. As discussed later in detail and alluded to earlier, the isotope characteristics and some trace element results from the Spring Mountain basalts suggest that this exact basalt type was not actually the mafic endmember. However, basalt had to be involved in the generation of Lava Mountain magmas and the Spring Mountain basalts satisfy the overall criteria for incorporation into such a model: [1] they represent locally erupted basalt and are the most primitive regional magma type; [2] overall their bulk chemistry and isotope characteristics are broadly appropriate as endmembers (e.g., high $^{87}Sr/^{86}Sr$, low $^{143}Nd/^{144}Nd$, and appropriate Pb isotope values that demonstrate they originated from ancient lithospheric mantle). MB13-4B is the basalt used in the model and is the least primitive of all five Spring Mountain basalt samples. It has the lowest Mg, Ni, and Cr, while having the highest Al_2O_3, TiO_2, Na_2O, and V. Since all four Lava Mountain basaltic andesite samples are extremely similar to one another geochemically, AD14-17 was selected as the basaltic andesite endmember because it is the only basaltic andesite with isotope analysis for later comparison. The Lava Mountain dacites are the most silica-rich rock types found on the volcano, and thus represent the most evolved endmember. For the model presented below, AD14-10 represents the Lava Mountain dacite sample.

Fig 3.1 outlines the basic stratigraphy of Lava Mountain. Both the most and least evolved material is found at the base of the Lava Mountain eruptive package. Overlying these lavas, at approximately 9100 m elevation, the composition of erupted magma becomes andesitic. On a total alkali silica diagram (Fig 3.1), all samples above 9100 m plot as andesites.

Modeling was completed using the MIX model from IgPet 2014 with the goal of quantifying the relative contributions of fractional crystallization, magma-mixing, and mixing+FC to the formation of the Lava Mountain volcanic rocks. Analysis from the MIX program shows that there are multiple methods to describe how Lava Mountain formed.

Model Overview

Step One

For this model to work, a mafic magma chamber must have existed below Lava Mountain. Step One includes fractional crystallization of basalt (MB13-4B) to basaltic andesite (AD14-17), and then basaltic andesite to dacite (AD14-10). The fractional crystallization models for both basalt to basaltic andesite and then basalt to dacite were completed using a fractionating mineral assemblage of magnetite (Ti_{10}), plagioclase (An_{67}), clinopyroxene (Wo_{42}-Mg_{44}-Fe_{14}), and olivine (Fo_{78}). For basalt to basaltic andesite, the proportions are as follows: mt 6.1%, An 52.4%, cpx 32.0%, and 9.5% ol. The fractionating assemblage proportions for basalt to basaltic andesite results in a sum of squares of residuals of 0.271 (Table 5.1). This indicates an acceptable fit to the data, as the sum of squares of residuals should be as close to zero as possible. F equals 0.64, indicating 36% crystal fractionation. For basalt (MB13-4B) to dacite (AD14-10) the proportions are as follows: mt 5.2%, An 51.1%, cpx 30.9%, and 12.9% ol. The sum of squares of residuals is 1.018, and F equals 0.58, indicating 42% fractionation.

In this model, the less-dense dacite, could have risen to the top of the magma chamber during fractionation and erupted sparingly. Subsequently, less evolved basaltic andesite magma from beneath the dacite was also able erupt, either going around or through partially solidified dacite. Separate eruptions of basaltic andesite and smaller dacite eruptions from the same magma chamber created the interstratified base of Lava Mountain.

Step Two

Step two of the model involves andesite creation through the mixing of basaltic andesite and dacite while fractional crystallization is ongoing. This second step was completed using a fractionating mineral assemblage of magnetite (Ti_{10}), plagioclase (An_{67}), clinopyroxene (Wo_{42}-Mg_{44}-Fe_{14}), and olivine (Fo_{72}), resulting in a sum of squares of residuals of 0.014 and a very small amount of fractional crystallization (F equals 0.91).

Step two involves open-system processes. Petrographic and isotopic evidence proves that Lava Mountain is not a closed system. In order for andesite to be generated, the chamber must be homogenized. This can happen through recharge of less-evolved basalt. When more magma is introduced to the system, it creates turbulence needed for mixing between the basalt/basaltic andesite and dacite, which may be enough force to trigger surface eruptions. Magma chamber disruption can also occur via faulting. Johnson et al., (2000) attributed magma mixing at the Miocene Duck Butte Eruptive Center in Oregon to extensive magmatism directly along a major Basin and Range normal fault. Although the lavas in the Duck Butte study are more silica-rich, the same mechanisms can apply to Lava Mountain. Brueseke and Hart (2009) proposed a similar mixing-induced faulting scenario to explain the genesis of some of the intermediate magmas in the mid-Miocene Santa Rosa-Calico volcanic field (NV). There are not nearly as many identified faults in the UWRB as there are near Duck Butte, however Lava Mountain does lie along the extension of a NW trending fault zone that extends through Pilot Knob and Wildcat Hill (Fig. 1.2).

In summary, this simplest model for Lava Mountain andesite creation involves the fractional crystallization of basalt to basaltic andesite (Fig 5.1), and basalt to dacite (Fig 5.2). This is followed by magma mixing and fractional crystallization of the basaltic andesite and dacite (Fig 5.3), as well as the homogenization of the chamber to create crystal-poor andesites. The calc-alkalic character of the evolved Lava Mountain andesites and dacites likely also reflects the interaction of these magmas with local crust (e.g., Archaen granitoid and gneiss), even though assimilation of local crust was not formally incorporated in the petrogenetic model. While mixing was the dominant process forming the andesites, crustal interaction did occur as manifested by the documented xenocrysts and some of their isotopic characteristics. Brueseke and Hart (2009) and Steiner and Streck (2013) documented similar interactions between tholeiitic parental magmas and calc-alkaline crust to generate mid-Miocene intraplate calc-alkaline intermediate magmas in the Pacific Northwest (U.S.A).

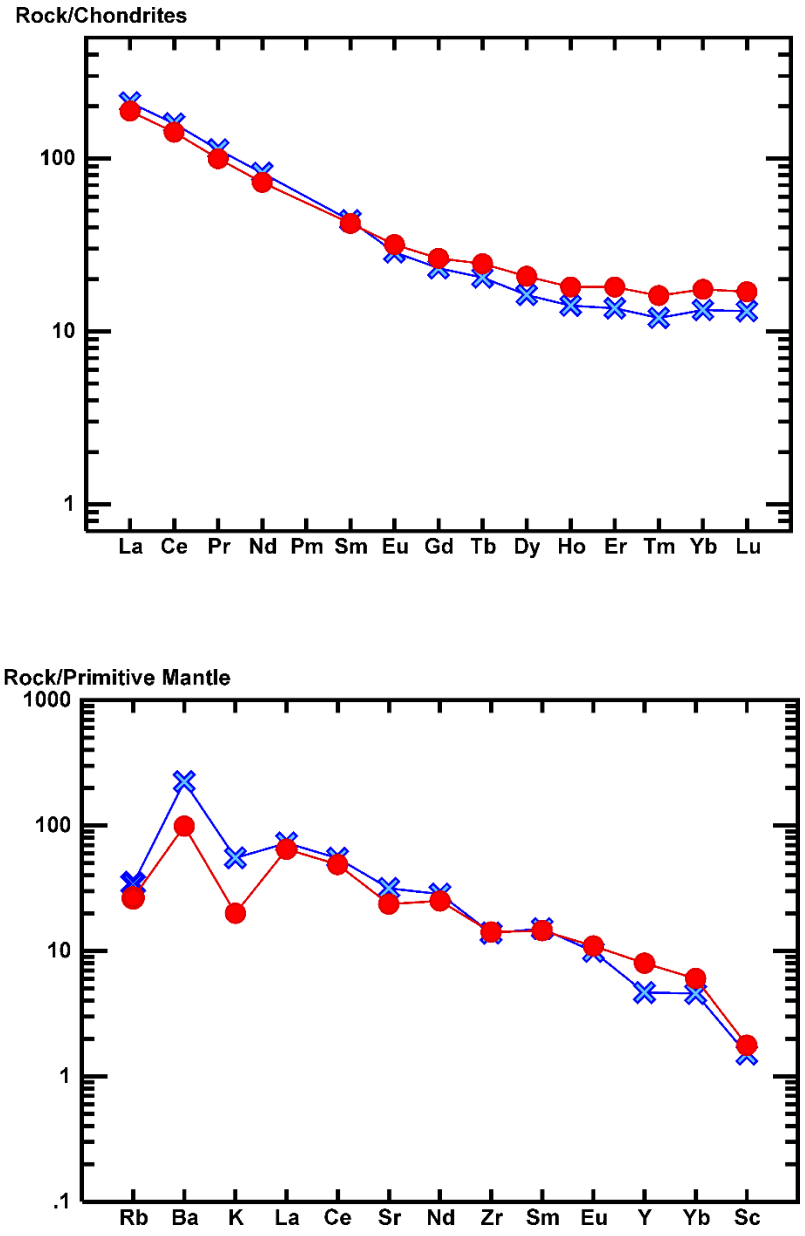

Figure 5.1 Diagrams for Step One, FC of basalt to basaltic andesite. Multi-element diagrams normalized to chondrites and primitive mantle (Sun and McDonough, 1989).Blue crosses are basaltic andesite Lava Mountain sample AD14-17. Red circles are calculated modeling results from the fractional crystallization of basalt MB13-4B to basaltic andesite AD14-17.

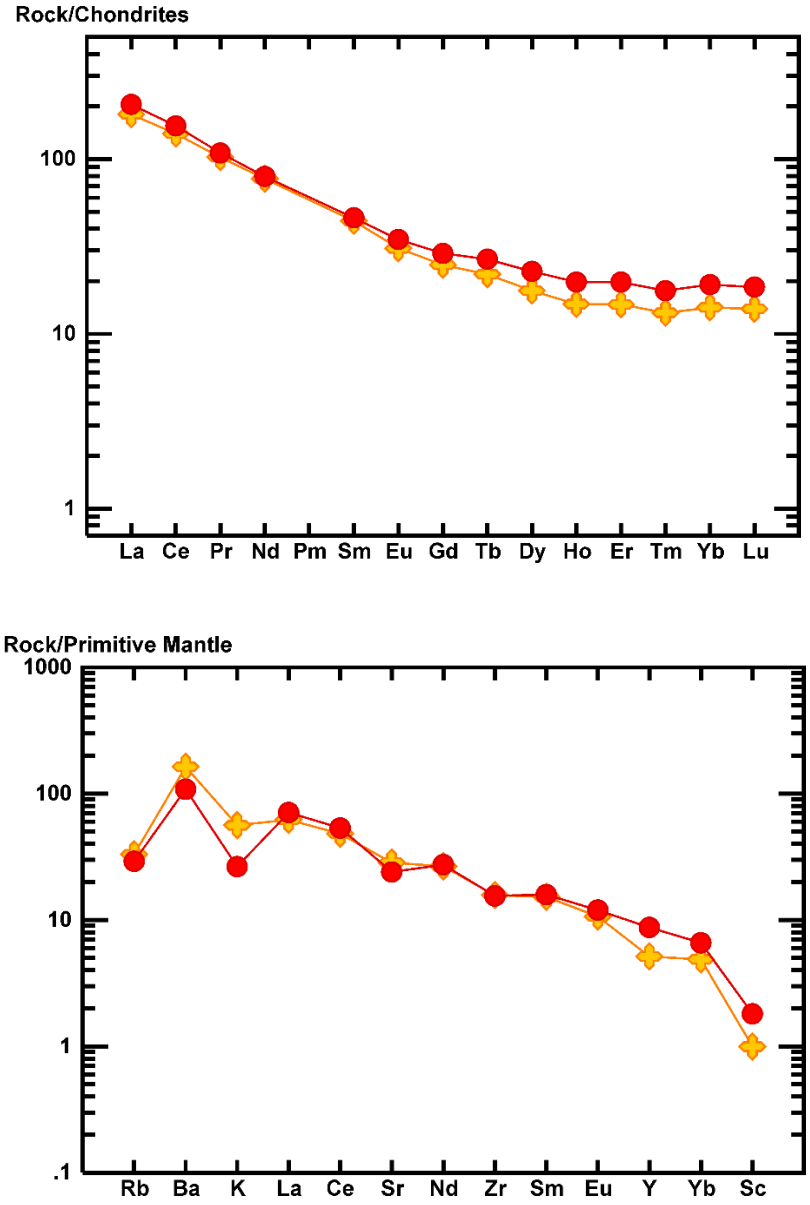

Figure 5.2 Diagrams for Step One, FC of basalt to dacite. Multi-element diagrams normalized to chondrites and primitive mantle (Sun and McDonough, 1989). Yellow crosses are dacite Lava Mountain sample AD14-10. Red circles are calculated modeling results from the fractional crystallization of basalt MB13-4B to dacite AD14-10.

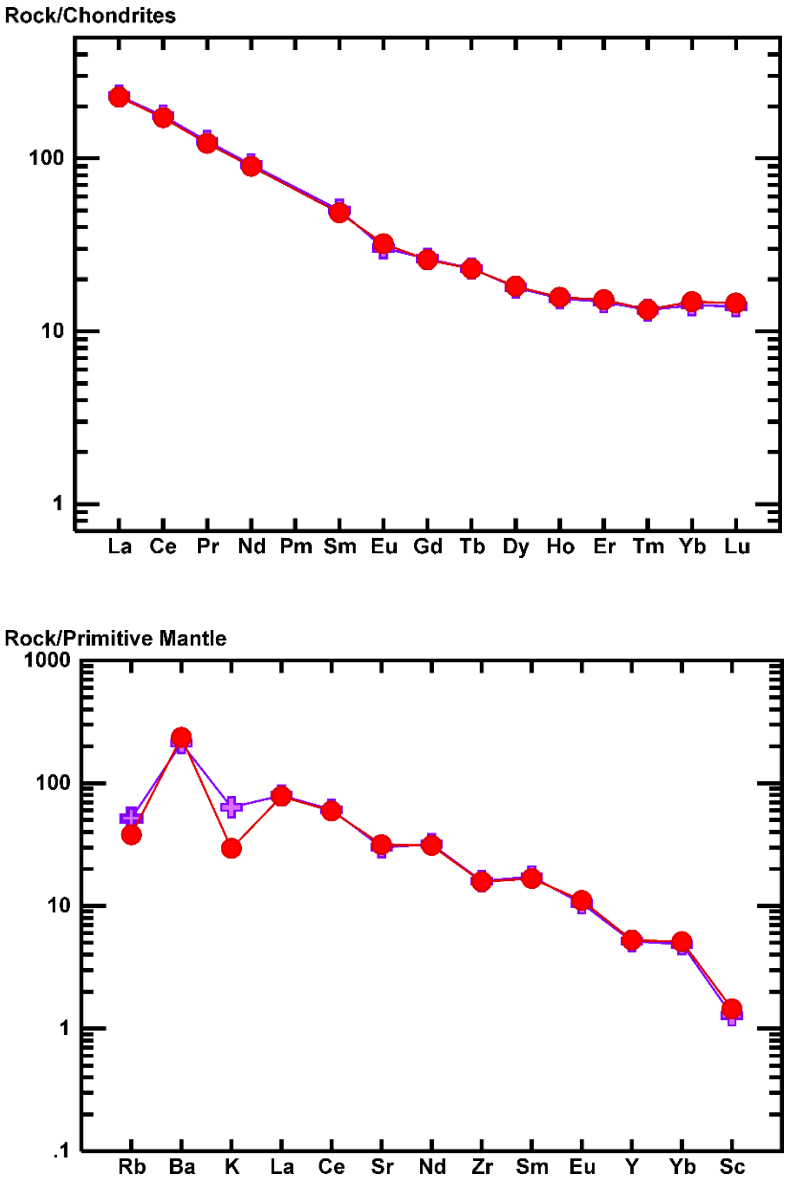

Figure 5.3 Diagrams for Step Two. Mixing of basaltic andesite AD14-17 and dacite AD14-10 to create andesite AD14-4. Multi-element diagrams normalized to chondrites and primitive mantle (Sun and McDonough, 1989). Purple crosses are andesite sample AD14-4. Red circles are calculated modeling results from the mixing of basaltic andesite and dacite to make andesite.

	Fractional Crystallization			Fractional Crystallization			FC + Magma Mixing		
Endmember A	MB13-4B		F = 0.643	MB13-4B		F = 0.581	AD14-17		F = 0.906
Endmember B	-			-			AD14-10		
Hybrid Magma	AD14-17			AD14-10			AD14-4		
	Obs.	**Calc.**	**R**	**Obs.**	**Calc.**	**R**	**Obs.**	**Calc.**	**R**
SiO2	56.28	56.33	1.00	63.29	62.29	0.98	58.95	58.91	1.00
TiO2	0.86	1.12	1.30	0.90	1.57	1.74	0.81	0.89	1.10
Al2O3	15.87	15.88	1.00	16.21	16.05	0.99	15.83	15.81	1.00
FeO	7.32	7.28	0.99	6.15	5.95	0.97	6.62	6.60	1.00
MnO	0.13	0.20	1.54	0.10	0.23	2.30	0.11	0.12	1.09
MgO	6.60	6.60	1.00	2.31	2.31	1.00	5.28	5.28	1.00
CaO	8.18	8.15	1.00	5.73	5.69	0.99	7.21	7.20	1.00
Na2O	2.79	2.71	0.97	3.38	3.28	0.97	3.00	3.01	1.00
K2O	1.68	1.28	0.76	1.71	2.00	1.17	1.94	1.88	0.97
P2O5	0.28	0.46	1.64	0.22	0.73	3.32	0.26	0.30	1.15
Σr2			**0.271**			**1.018**			**0.014**
Rb	22.10	16.80	0.76	21.20	18.50	0.87	33.10	24.10	0.73
Ba	1583.00	690.70	0.44	1153.70	758.30	0.66	1497.10	1650.40	1.10
Sr	674.10	498.80	0.74	606.80	506.40	0.83	639.70	665.70	1.04
V	171.50	181.50	1.06	128.90	190.60	1.48	147.50	159.90	1.08
Cr	274.80	74.00	0.27	27.30	62.00	2.27	217.30	188.70	0.87
Ni	116.50	42.30	0.36	10.70	27.90	2.61	88.10	73.10	0.83
Zr	157.30	158.40	1.01	178.10	173.80	0.98	180.40	176.20	0.98
Sc	25.10	29.20	1.16	16.60	29.80	1.80	21.30	23.90	1.12
Cu	32.00	46.10	1.44	21.90	50.90	2.32	34.10	33.00	0.97
La	50.50	44.50	0.88	43.20	48.70	1.13	55.10	45.40	0.82
Ce	98.60	86.70	0.88	86.50	94.80	1.10	109.00	88.60	0.81
Pr	10.80	9.46	0.88	9.83	10.30	1.05	12.10	9.73	0.80
Nd	38.90	33.90	0.87	36.40	37.10	1.02	43.50	35.00	0.80
Sm	6.78	6.44	0.95	6.84	7.05	1.03	7.77	6.10	0.79
Eu	1.68	1.84	1.10	1.81	2.01	1.11	1.78	1.51	0.85
Gd	4.82	5.42	1.12	5.15	5.93	1.15	5.46	4.34	0.79
Tb	0.78	0.92	1.18	0.83	1.00	1.20	0.87	0.70	0.80
Dy	4.17	5.28	1.27	4.53	5.78	1.28	4.61	3.76	0.82
Ho	0.81	1.02	1.26	0.85	1.12	1.32	0.88	0.73	0.83
Er	2.28	2.98	1.31	2.46	3.27	1.33	2.47	2.05	0.83
Tm	0.31	0.41	1.32	0.34	0.45	1.32	0.34	0.28	0.82
Yb	2.28	2.97	1.30	2.43	3.25	1.34	2.43	2.06	0.85
Lu	0.34	0.43	1.26	0.36	0.47	1.31	0.36	0.30	0.83
Y	21.50	36.30	1.69	23.60	39.70	1.68	23.60	23.90	1.01

Table 5.1 For all major elements, the sum of the squared residuals is shown in bold and Obs.= observed concentrations; Calc.=calculated concentrations; R=the ratio of calculated daughter to the observed values; F=% liquid remaining. For simplicity, an assemblage of magnetite (Ti_{10}), plagioclase (An_{67}), and pyroxene (Wo_{42}-Mg_{44}-Fe_{14}) were used, along with olivine (Fo_{78}) for Step One and (Fo_{72}) for Step Two. AD14-10 is a dacite, AD14-17 is a basaltic andesite, and AD14-4 is an andesite scoria, all from Lava Mountain. Calculations were completed using the MIX module of IgPet 2014.

Problems Associated with the Model

The model does not address the issue of crustal contamination because of its simplicity. Both isotope and petrographic evidence prove that although minimal, Lava Mountain magmas were definitely affected by crustal interaction. This most likely occurred through assimilation from the walls of the magma chamber, and is further explained in Chapter 6.

It is clear that the Spring Mountain basalt is not the mafic endmember of the Lava Mountain system. Since the Spring Mountain basalts are the most mafic rocks sampled in the UWRB, it was originally assumed they would fill this role. However, the Pb isotope data refutes the idea of the exact basalt type found at Spring Mountain being the mafic endemember because the basalts fall directly in the middle of a field defined by the intermediate rocks. However, a mafic endmember is required by the fact that the volcano exists and the bulk major and trace element chemistry of the Spring Mountain basalts are a decent approximation for such an endmember, at least from the standpoint of a first-order model. Furthermore, the isotope characteristics of the evolved rocks also indicate that the mafic endmember involved had to have formed via melting of Archean lithosphere, thus ruling out the potential involvement of asthenosphere or plume-derived basalt (e.g., related to Yellowstone or other).

According to REE plots (Fig. 4.7), there is a small negative Eu anomaly for the andesites which is consistent with plagioclase fractionation in the fractional crystallization + mixing models. Overall, REE diagrams show trace element patterns do not significantly change from basalt to dacite, but simply become more enriched. So, even though fractional crystallization is occurring, no individual phases are strongly fractionating one element over another.

Problems are observed with trace elements Ni, Cr, Sr, and Ba. Sr and Ba can partially be explained through the presence of crustal assimilation, which is not modeled. The calculated Ni and Cr values for the model are much lower compared to the observed values. The amount of olivine fractionation in these samples does not correlate with the high amount of calculated olivine in the andesites. This could suggest that there is a lower percent of Ni fractionation in the andesites. Compared to Ni, olivine generally does not have nearly as high Cr values, although all calculated whole rock Cr values are greater than the Ni values.

Chapter 6 - Discussion

The main focus of this thesis has been to understand the petrogenesis of intermediate-composition volcanics from Lava Mountain, WY. Geochemical data further allow us to examine geodynamic models for the origin of the UWRB volcanism—in particular, whether there is a causal relationship with the Yellowstone hotspot and the role of ancient vs modern subduction zone processes. These aspects of the data are discussed in the latter sections of the discussion.

Petrography and Open System Processes

A number of mechanisms could be responsible for the disequilibrium textures observed. An influx of mafic magma into an evolving magma chamber would over time lead to disequilibrium textures, as mafic magmas periodically escape and interact with the more-evolved melts on their way to the surface. Conversely, disequilibrium textures could also be associated with rapid ascent of magma to the surface (Feineman, et. al., 2010). It is possible that the disequilibrium textures observed in the more primitive basaltic andesites were generated in this way. However, the textures observed in the andesites and andesite/dacites and their essentially aphyric nature (e.g., ~85-90% groundmass) are more likely the result of magma mixing, coupled with relatively quick ascent and eruption (Johnson et al., 2000; Brueseke and Hart, 2009).

Disequilibrium textures are also observed elsewhere in the UWRB. At Crescent Mountain, orthopyroxenes display disequilibrium textures similar to those in pyroxenes from Lava Mountain volcanics. Crescent Mountain basaltic trachyandesites are also sufficiently evolved and silica saturated to contain quartz in the groundmass, while also containing highly altered olivines, i.e. the olivines appear not to be in equilibrium with the host basaltic trachyandesite.

At Spring Mountain, there is substantial evidence to suggest that some olivines are xenocrystic. Olivines that are Mg-rich are typical of depleted upper mantle from which basaltic melts have been extracted (Embey-Isztin and Dobosi, 2007; Downes et. al., 2004). The study from Downes et al. (2004) provides data on olivines from peridotite xenoliths from the Bearpaw Mountains in Montana that have Fo values ranging from 91.8 to 77.4. These values are very similar to the Spring Mountain olivine Fo contents. Our microprobe results indicate that Spring Mountain basalts contain olivines with compositions up to Fo_{90} (MB13-3) (Table 4.1). MB13-4a, the fine-grained sample, has only Fo_{77} olivines that are subhedral. Olivines from the Bearpaw

peridotites have very similar NiO concentrations (Downes et al., 2004), ie. ranging from 0.26 – 0.40 wt. %. By comparison, NiO concentrations for Spring Mountain olivines range from 0.17 – 0.38 wt. %. Thus, it is likely that the Mg-rich olivines (e.g., ~Fo_{90}) found in the basalts at Spring Mountain are either the product of crystallization of a primitive parental basalt precursor deep within the mantle or lower crust, or disaggregation of mantle-derived peridotites incorporated into the basalt as they ascended to the surface. The complete absence of other xenocrystic phases—such as spinel, orthopyroxene or clinopyroxene—suggests the former explanation may be more reasonable.

Although geochemical evidence, particularly isotopic data (see below) and their calc-alkaline nature, suggest that some crustal assimilation probably occurred during the petrogenesis of Lava Mountain andesites/dacites, little petrographic evidence for this process was observed. Furthermore, major element modeling presented in Chapter 5 demonstrates that the petrogenesis of Lava Mountain volcanic rocks does not require assimilation of a crustal component. Nonetheless, anhedral, partially resorbed xenocrystic microcline is observed in andesite sample AD14-7 (Fig. 3.14c). It is the only microcline crystal observed in all Lava Mountain thin sections, and suggests interaction with lower to middle crust. Two plagioclase crystals with reaction rims are found in andesite sample AD14-6. They are interpreted to be xenocrystic based on their larger size and thick reaction rims, suggesting they were not in equilibrium with the host andesite. Basaltic andesite AD14-14 contains a single large quartz xenocryst (~3.2% modally) in a rock that contains olivine and orthopyroxene phenocrysts (Fig. 3.13e). Since it was only one crystal that was anhedral, partially resorbed, and much larger than other crystals in the sections, it was most likely assimilated from a felsic rock.

Geochemical Data and Open System Processes

Although the previous map compilation by Christiansen (2001) suggested that Lava Mountain is a basaltic volcano, major element chemistry completed as part of this study proves the rocks are more evolved. As previously stated, all samples plot as basaltic andesites to dacites on a total alkali silica diagram (Fig 3.1). Major element trends for Lava Mountain also show primarily positive or negative linear trends with SiO_2 with weak to no inflection in the data (Fig. 4.2), consistent with an origin dominated by fractional crystallization processes.

Modeling results presented in Chapter 5 are consistent with the interpretation that primitive basalts, like those present at Spring Mountain, fractionated variable proportions of plagioclase, clinopyroxene, olivine and magnetite to create basaltic andesites. Lava Mountain andesites were created through a combination of fractional crystallization and magma mixing processes, with minor crustal contamination influence. A linear trajectory with steep vectors on a trace element diagram highlights patterns commonly associated with two-component mixing. This is evident in plots such as La/Sm vs. La and Nb/La vs. La/Yb (Fig 6.1a,b). Based on stratigraphic field evidence—in particular, the observation that the initial and basal eruptions at Lava Mountain alternated between basaltic andesitic and dacite (Fig 3.2)—the model proposed here is one of continuous fractionation of the basaltic andesites and mixing with dacitic magma to produce the andesitic lavas that form the greatest volume of the volcano. This process continued until volcanism ceased with the pyroclastic eruption(s) that formed the capping andesite scoria cone.

Isotopic Evidence for a Lithospheric Mantle Source

Lithospheric mantle has a radiogenic εNd isotope composition, i.e εNd values <<0, similar to all the εNd values of the UWRB samples. εNd values decrease linearly with increasing silica across Lava and Spring Mountain samples, with Spring Mountain samples having the lowest silica and highest εNd (Fig. 6.2). The isotope data for Spring Mountain provide important evidence for the petrogenesis of the rocks from the UWRB. In Sr-Nd isotope space, the analyzed sample plots below the value for CHUR and well below the composition of asthenospheric mantle—represented in this region by the composition of Basin and Range basalts that have Sr values from 0.70331 to 0.70658, and Nd values from 0.51243 to 0.51305 (Kempton et al., 1991).

Pb isotopes of the upper crust, upper mantle, and mantle plumes typically plot to the right of the Geochron. Archean lower crust in some cratonic areas has unradiogenic Pb, where post-Archean lower crust does not (Rudnick, 1990), although the lower crust of the Colombia supercontinent (which includes the Wyoming Craton) appears to have preserved radiogenic Pb isotope compositions (Kempton et al., 2001; Kempton, 2015). According to Rudnick and Goldstein (1990), only areas that have remained tectonically stable for a long period of time (e.g., cratons) can preserve Pb isotope compositions that are distinct from convecting upper mantle. All of the samples from this study plot to the left of the 4.5 Ga Geochron and directly on to above the Stacey and Kramers growth curve. This includes the Spring Mountain basalts, indicating they are

distinct from convecting upper mantle (Fig 4.9). It further shows they were not greatly affected by the Sevier or Laramide Orogenies and associated subduction processes, or the Pb isotope values would be higher. Pb isotopes that plot to the left of the geochron indicate involvement of a reservoir that has evolved for a significant proportion of earth history with a low U/Pb ratio, such as ancient lithospheric mantle or depleted continental crust. As illustrated in Fig 4.9, the UWRB samples plot on the 2.8 Ga Bearthooth isochron, as would be expected if their Pb isotope character was derived primarily from ancient lithospheric mantle. This is in contrast to basalts from the Basin and Range, which have much more radiogenic values at $^{206}Pb/^{204}Pb$ = 18.596-19.397, $^{207}Pb/^{204}Pb$ = 15.530-15.594, and $^{208}Pb/^{204}Pb$ = 38.063-38.799 (Kempton, et. al., 1991). The relatively primitive compositions of the Spring Mountain basalts (e.g., high Mg #s, Cr and Ni contents due to large amounts of olivine) would appear to preclude significant amounts of crustal contamination in their petrogenesis and instead indicate derivation from lithospheric mantle.

Similarities to Other Areas

UWRB isotope concentrations can be compared to samples analyzed in the Leucite Hills, which are located in southwest/south central Wyoming. In general, the Leucite Hills have slightly higher values for $^{143}Nd/^{144}Nd$, lower values for $^{87}Sr/^{86}Sr$, and similar εNd. Like the UWRB, the lithospheric mantle beneath the Leucite Hills has undergone both depletion and enrichment events. Depletion took place with the creation of Archean crust, followed by metasomatism as a result of Eocene subduction leading to high Nb and Ta anomalies (Mirnejad and Bell, 2006). UWRB rocks are also similar to transition zone basalts around the Colorado Plateau, although their Pb isotopes plot below the Stacy-Kramer growth curve as opposed to on or above it (Stacey and Kramers, 1975). Transition zone basalts were most likely derived from lithospheric mantle. Nd isotopes further support the enrichment theory, since compared to Nd isotopes in other Cenozoic basalts, transition zone basalts have lower $^{143}Nd/^{144}Nd$ isotopes (Fitton, J. G. et. al., 1988).

Petrographic evidence and isotope signatures prove that UWRB rocks were affected by small degrees of crustal contamination. In the UWRB, the range of Sr and Nd isotopes suggests all samples did not originate from a single homogenous source. Based on highly negative εNd isotope signatures and high Sr concentrations in the UWRB samples, one option, as mentioned earlier, is Archean Wyoming Craton crust, which consists of a combination of gneiss, granodiorite, and metasedimentary rock (Foster, et. al., 2006). The xenocrysts found in the Lava Mountain

andesite thin sections (quartz and microcline) are consistent with the mineralogy of granodiorite. Further, a plot of $^{87}Sr/^{86}Sr$ vs. SiO2 shows a positive trend between rocks of the UWRB, indicating some crustal involvement (Fig 6.3). However, more detailed modelling is needed to decipher whether this is lower vs. upper-crustal involvement and to what specific degree.

The Role of Ancient vs. Recent Subduction Processes

A continental magmatic arc was present in the vicinity of the UWRB in the Eocene and it is possible that subduction-related magmatism affected the region during the Proterozoic (Mueller and Wooden, 1988). A MORB-normalized multi-element diagram shows Lava Mountain andesites are heavily depleted in the immobile elements Nb and Ta, while enriched in Ba, Ce, and Sm, which are all highly incompatible. Nb and Ta depletion suggests a possible link to a shallow subduction zone component. Modern subduction processes tend to produce magmas that are enriched in LREE, depleted in HREE, and depleted in HFSE (Smithies et. al., 2004).

Geochemical signatures of the rocks of the UWRB show a subduction influence and indicate that the prior history of subduction in northwest Wyoming imparted geochemical signatures to the magmas in this study. Although subduction events took place both during the Proterozoic and Cenozoic, an ancient subduction event would be consistent with isotope data. Th and U are usually enriched in crustal material and depleted in mantle material because they are so highly incompatible; Lava Mountain, Crescent Mountain, and Pilot Knob all have a Th enrichment relative to Nb, P, and Ti (Fig. 4.5). A diagram of Th/Yb vs. Ta/Yb shows an enrichment of Th with respect to Ta, which is usually characterized by source regions that have been metasomatized by a subduction event (Fig. 6.4). A negative relationship between $^{143}Nd/^{144}Nd$ and Ba/Nb (Fig 6.5a) and a positive correlation between $^{87}Sr/^{86}Sr$ and Ba/Nb (Fig. 6.5b) suggests that an ancient subduction experience may have had an effect on isotope ratios. Ratios in the melts may have been derived from the partial melting of enriched lithospheric mantle and mixed with magmas from the asthenosphere (Kempton, et. al., 1991). In order for these elements to maintain their geochemical characteristics for such a long period of time, they must have been isolated from convecting mantle (Mirejad and Bell, 2006).

Relationship to Yellowstone Volcanics

One goal of this study was to determine whether UWRB volcanism is petrogenetically linked to the end of the third Yellowstone volcanic cycle. The new Sr-Nd-Pb isotope data reported

here suggests that such a link is not supported (Fig 6.6, 6.7). The εNd values are considerably lower than those of Yellowstone basalts, which range from -7.9 to -2.4. Yellowstone $^{87}Sr/^{86}Sr$ ratios range from 0.7038 to 0.7088, where UWRB values are slightly higher and range from 0.7056 to 0.7088. Additionally, Snake River Plain olivine tholeiites are characterized by $^{87}Sr/^{86}Sr$ values between 0.7058 and 0.7079, with almost no correlation between $^{87}Sr/^{86}Sr$ and Sr, suggesting little to no crustal contamination (Menzies et al., 1984). $^{143}Nd/^{144}Nd$ ratios for the least fractionated olivine tholeiites of the Snake River Plain range from 0.51252 to 0.51245, above than UWRB concentrations. $^{206}Pb/^{204}Pb$ ratios for Snake River Plain olivine tholeiites fall between Hawaiian Island alkaline and tholeiitic magmas (Menzies et al., 1984). $^{206}Pb/^{204}Pb$ and $^{207}Pb/^{204}Pb$ values for Snake River Plane basalts range from 17.6 to 18.3 and 15.57 to 15.63, respectively (Hanan, Shervais, and Vetter, 2008). Yellowstone $^{206}Pb/^{204}Pb$ and $^{207}Pb/^{204}Pb$ values range from approximately 16.1 to 17.4, and 15.3 to 15.51, respectively (Hildreth, et. al., 1990). These data indicate that the mantle source for the Spring Mountain basalts (and by analogy, Lava Mountain evolved rocks and other Cenozoic volcanics in the UWRB) is different from that of Yellowstone basalts. It is therefore unlikely that the UWRB volcanics are related directly to Yellowstone magmatism.

Magma Generation

Melting for volcanic genesis was most likely triggered by magma upwelling during lithopheric extension. Locally, the UWRB exhibits evidence of recent extension. For example, Love, et. al. (1979) mapped normal faults that extend to the southeast of the UWRB in the Wind River Range. Although not shown directly on a map, it is possible these faults connect with other extension-related faults along which lie Lava Mountain, Wildcat Hill, and Pilot Knob to the northwest of the UWRB and to the south of Yellowstone (Fig. 1.2). The Teton fault, to the west, is also near the UWRB, and shows evidence for two separate extension events: one between 16.33 and 10.3 Ma, and the second which initiated at 3 Ma and continues to the present (Anders, et al., 2009). It is possible that the more recent extension event, which is local Basin and Range extension, may have been caused by a thermal effect from migration over the Yellowstone Plume (Anders, et al., 2009; Camp, Pierce, and Morgan, 2015).

Underneath the Snake River Plain and Yellowstone, an anomaly exists at approximately 200-250 km deep, which has been interpreted to be the mantle plume causing Yellowstone melting.

The effect on the anomaly on the North American lithosphere is parabolic in shape, which is typical for plumes (Obrebski, et. al., 2011). Pierce and Morgan, (1992) and Anders et al. (2009) suggest there was a wave of extensional activity before volcanism began at any given location along the Snake River Plain hotspot track that is attributed to the outward migration of the Yellowstone plume, which caused continued extension as the North American plate migrated over the Yellowstone plume. The thinning of the adjacent lithosphere through extension provided room for magma upwelling to occur. In this model, heating of the lithosphere by the upwelling plume would also occur, which could, along with decompression due to extension, facilitate lithospheric melting.

Just like the rocks of the UWRB, olivine tholeiite basalts of the Snake River Plain have REE signatures that suggests melting began within spinel-lherzolite facies, or at shallower depths (no deeper than 100 km). Snake River Plain melting temperatures most likely do not succeed 1450°C (the solidus temperature 75 km; Wang, et. al. 2002) which is similar to temperature estimates for the southern and central Basin and Range province. Although this temperature range is representative of the asthenospheric mantle, it can also represent parts of the lithospheric mantle. The thermal conditions of the mantle beneath the Snake River Plain and parts of the Basin and Range provinces are more typical of conditions affected by lithospheric extension than mantle plume upwelling (Leeman et al., 2009). Although upwelling of plume could potentially cause mantle melting solely on the basis of heating the lithospheric mantle under the UWRB, it is not required. There is not significant evidence that the Yellowstone Plume is hot enough to melt and erode a lithospheric plate (Leeman et al., 2009). Further work needs to be completed to directly determine if the volcanic rocks of the UWRB are directly thermally related to deep plume volcanism, or if they are the result of melting from recent extension (which was caused by the upwelling plume, or not)

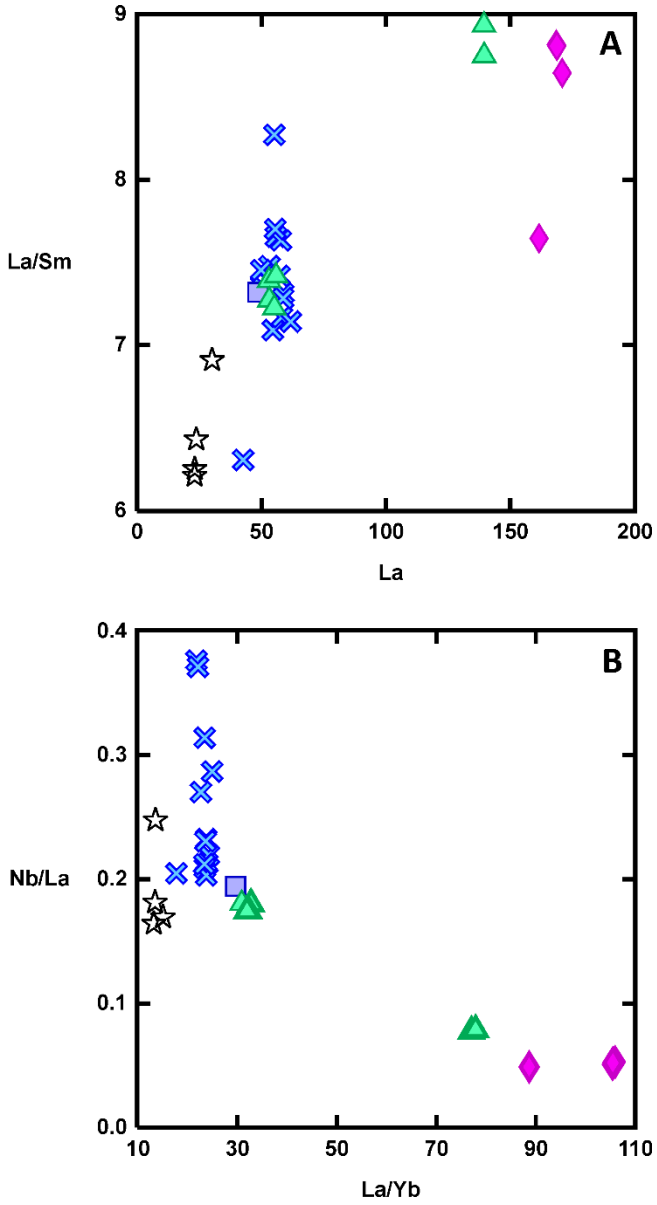

Figure 6.1 A) La/Sm vs. La and B) Nb/La vs. La/Yb

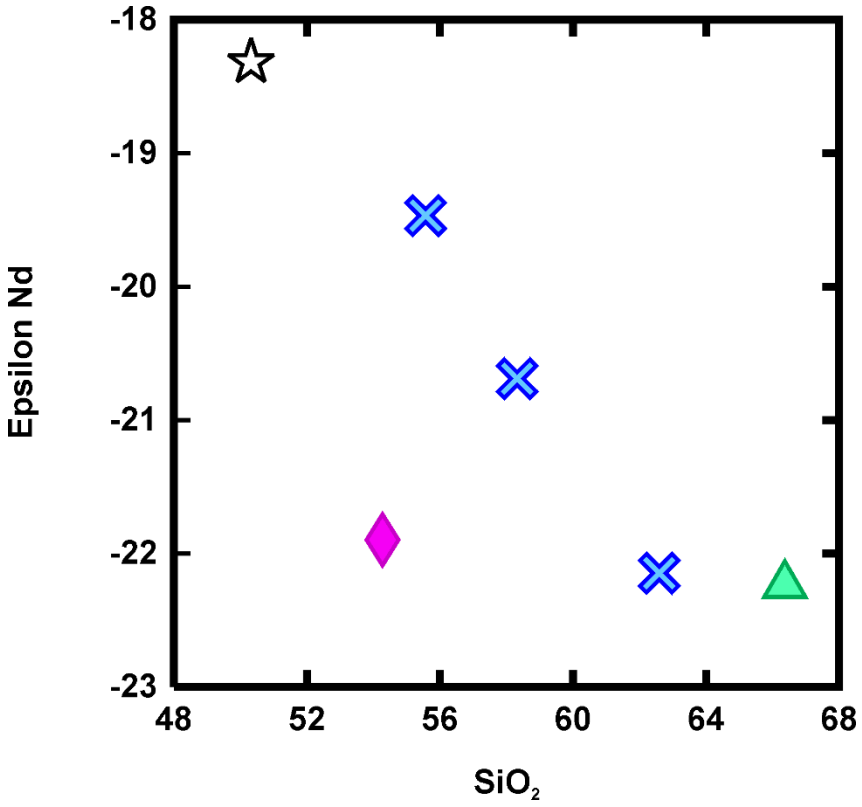

Figure 6.2 Epsilon Nd values decrease linearly with increasing silica

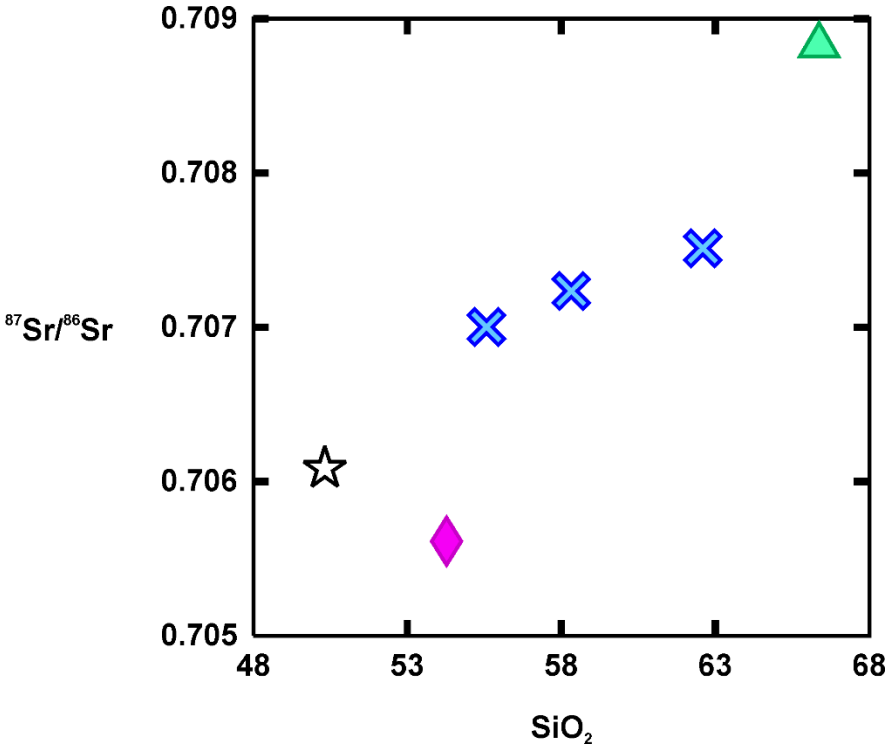

Figure 6.3 $^{87}Sr/^{86}Sr$ vs. SiO_2

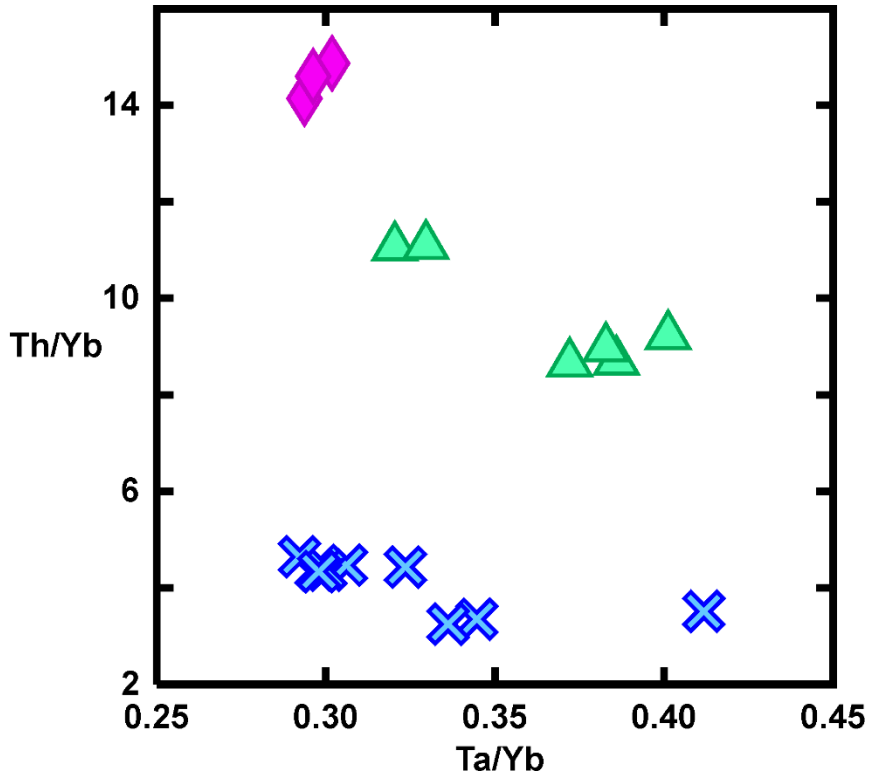

Figure 6.4 Th/Yb vs. Ta/Yb. Th is enriched relative to Ta

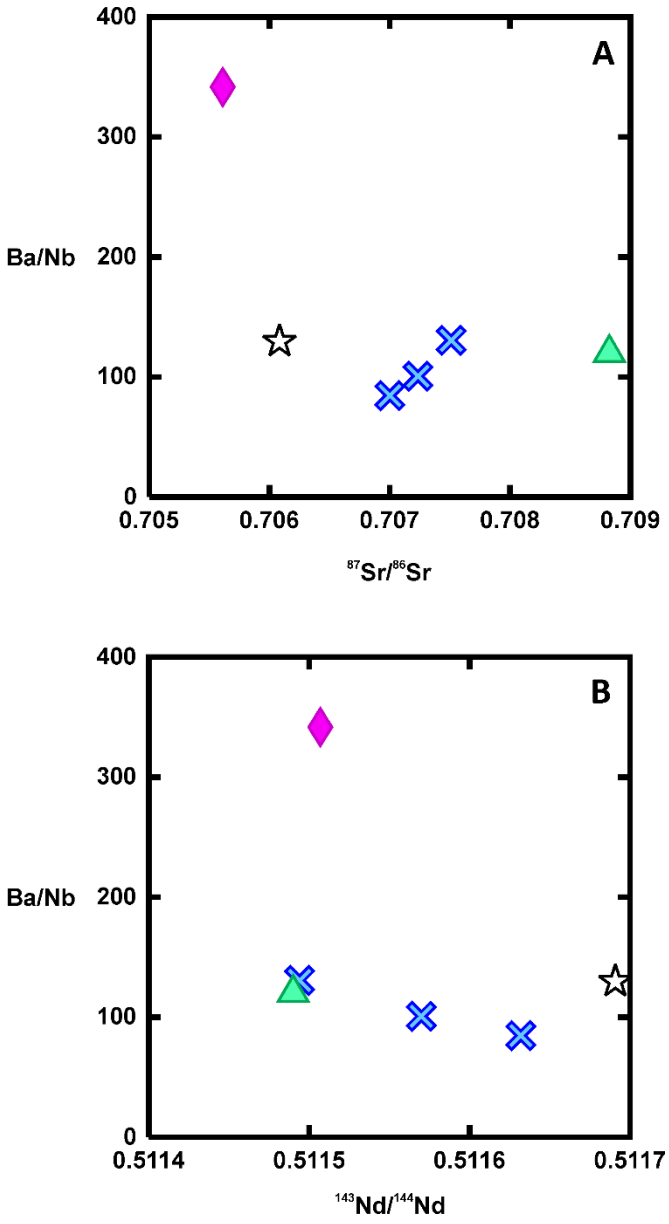

Figure 6.5 A) A negative relationship of Ba/Nb and $^{143}Nd/^{144}Nd$ and a positive relationship between Ba/Nb and $^{87}Sr/^{86}Sr$ suggests an ancient subduction event may have affected the UWRB, as opposed to more recent events.

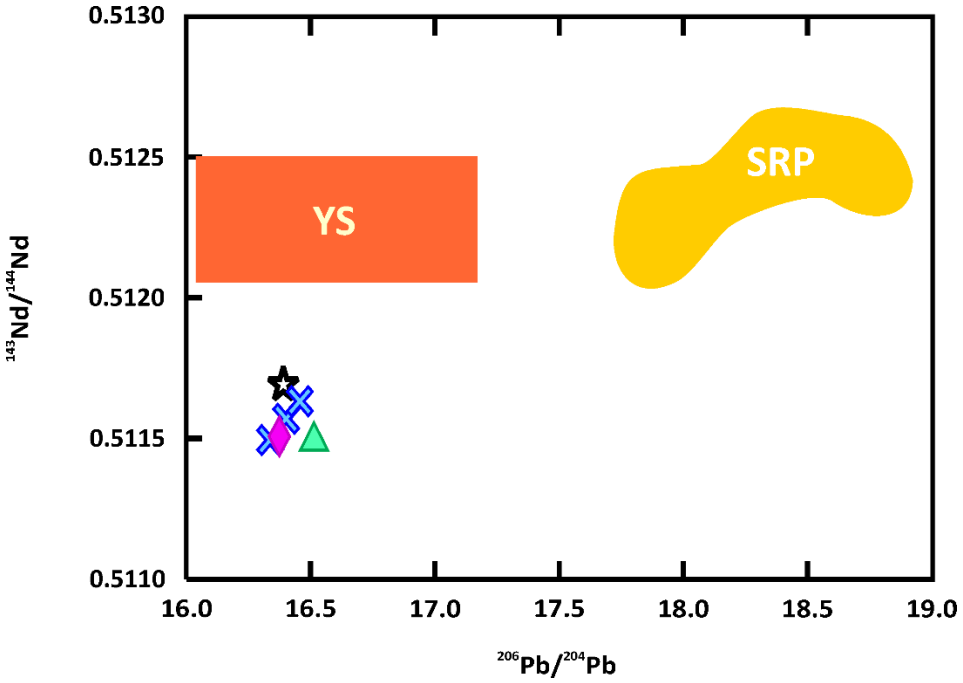

Figure 6.6 $^{143}Nd/^{144}Nd$ vs. $^{206}Pb/^{204}Pb$

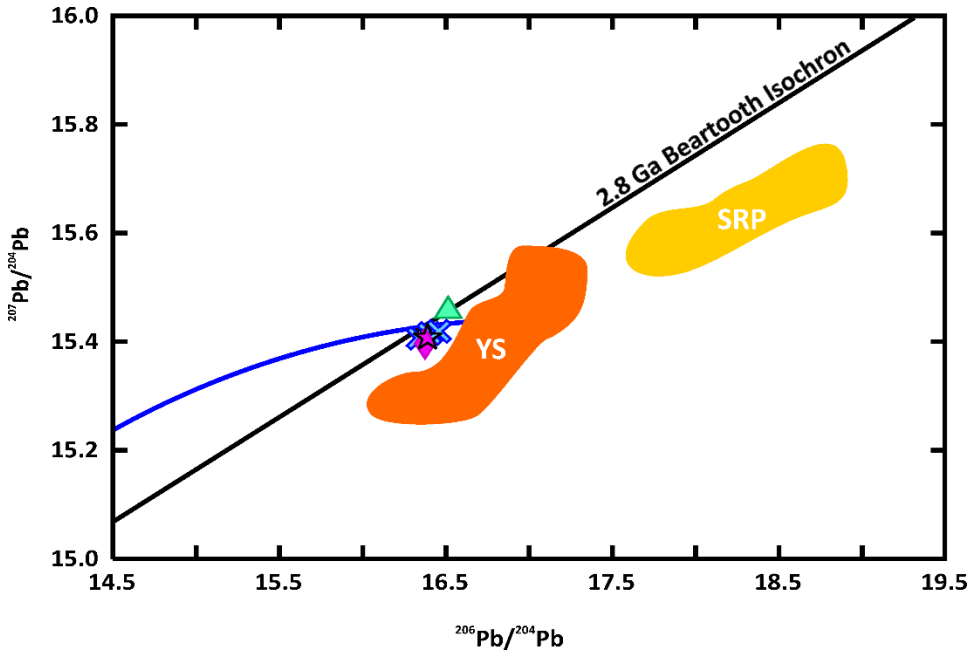

Figure 6.7 $^{207}Pb/^{204}Pb$ vs. $^{206}Pb/^{204}Pb$

Chapter 7 - Summary

The similarities of various signatures between the rocks of the UWRB suggest there is a potential for the rocks to be related to one another, both isotopically and chemically. Three types of rocks are observed on Lava Mountain: basaltic andesite, andesite, and dacite, Open system textures such as sieved, anhedral, and resorbed crystals, in combination with sparse xenoliths of alkali feldspar and quartz, imply magma mixing assisted with UWRB rock petrogenesis. Trace and REE subduction signatures coupled with isotopic data suggests the UWRB rocks were influenced by an ancient subduction event that affected the Wyoming craton during the Proterozoic.

Lava Mountain was created through the fractional crystallization of basalt to produce basaltic andesite and dacite, coupled with volcanism. Although it must have been a basalt fractionating to produce basaltic andesite and dacite, isotope data rules out the possibility that Spring Mountain is the mafic endmember of the system. The mixing of basaltic andesite and dacite combined with continuous fractional crystallization produced the approximate 4.6 km^3 of andesite found on Lava Mountain. This model is further supported by the crystal-poor nature of Lava Mountain andesites, suggesting they were almost or fully liquid before eruption. The fact that the Spring Mountain basalt has higher $^{87}Sr/^{86}Sr$ and lower $^{143}Nd/^{144}Nd$ values and is still an accurate fit to the model supports the theory that the actual basalt endmember for the system originated from the lithospheric mantle. Although crustal assimilation is not required for the model to work, petrographic and isotope evidence suggest a small amount of assimilation occurred, most likely from local parts of the Wyoming Craton.

REE patterns and other similarities suggest the rocks of the UWRB were produced by relatively shallow melting in spinel-lherzolite facies in the mantle and the melting that caused UWRB magma generation initially, more than likely originated via extension that was either related to Basin and Range tectonism or the Yellowstone hotspot.

References

Abedini, A. A., Calvert, A. T., and Hurwitz, S. (2007). New 40Ar/39Ar age determinations of basalts from the Yellowstone Plateau Volcanic Field [Abstract]. American Geophysical Union, Fall Meeting, abstract #V53B-1321.

Adams, D. C. (2014). Intermediate Volcanism Associated with the Yellowstone Hotspot, Southeastern Idaho and Western Wyoming [Abstract]. Geological Society of America, Rocky Mountain and Cordilleran Joint Meeting.

Anders, M. H., Saltzman, J., and Heming, S. R. (2009). Neogene Tephra Correlations in Eastern Idaho and Wyoming: Implications for Yellowstone Hotspot-Related Volcanism and Tectonic Activity. Geological Society of America Bulletin, 121, 837-856.

Blackstone, D. L. (1966). Pliocene Volcanism, Southern Absaroka Mountains, Wyoming. Contributions to Geology, 5(1), 21-30.

Brueseke, M. E. and Hart, W. K. (2009). Intermediate Composition Magma Production in an Intracontinental Setting: Unusual Andesites and Dacites of the mid-Miocene Santa Rosa-Calico Volcanic Field, Northern Nevada. Journal of Volcanology and Geothermal Research, 188, 197-213.

Brueseke, M. E., Heizler, M. T., Hark, W. K., and Mertzman, S. A. (2007). Distribution and Geochronology of Oregon Plateau (U.S.A.) Flood Basalt Volcanism: The Steens Basalt Revisited. Journal of Volcanology and Geothermal Research, 161, 187-214.

Camp, V. E., Pierce, K. L., and Morgan, L. A. (2015). Yellowstone Plume Trigger for Basin and Range Extension, and Dike Injection Oblique to Regional Stress along the Nevada-Columbia Basin Magmatic Belt. Geosphere, 11(11).

Camp, V. E. and Ross, M. E. (2004). Mantle Dynamics and Genesis of Mafic Magmatism in the Intermontane Pacific Northwest. Journal of Geophysical Research, 109, B08204

Carlson, R. W., and Hart, W. K. (1987). Crustal Genesis on the Oregon Plateau. Journal of Geophysical Research, 92(B7), 6191-6206.

Christiansen, E. H. and McCurry, M. (2008). Contrasting Origins of Silicic Volcanic Rocks from the Western Cordillera of the United States. Bulletin of Volcanology, 70, 251-267.

Christiansen, R. L., Lowenstern, J. B., Smith, R. B., Heasler, H., Morgan, L. A., Nathanson, M., Mastin, L. G., Muffler, L. J. P., and Robinson, J. E. (2007). Preliminary Assessment of Volcanic and Hydrothermal Hazards in Yellowstone National Park and Vicinity. United States Department of the Interior, USGS, Open-File Report 2007-1071.

Christiansen, R. L., Foulger, G. R., and J. R. Evans. (2002). Upper-mantle origin of the

Yellowstone hotspot. Geological Society of America Bulletin, 114(10), doi: 10.1130/0016-7606(2002)114<1245:UMOOTY>2.0.CO;2

Christiansen, R. L. (2001). The Quaternary and Pliocene Yellowstone Plateau volcanic field of Wyoming, Idaho, and Montana. United States Geological Survey, Professional Paper 729-G.

Christiansen, R. L. (2001). Upper Cenozoic Geologic Map, Yellowstone Plateau Volcanic Field [map]. 1:500,000. United States Department of the Interior, USGS. From USGS Professional Paper 729-G.

Christiansen, R. L. (1984). Yellowstone Magmatic Evolution: Its Bearing on Understanding Large-Volume Explosive Volcanism. Explosive Volcanism: Inception, Evolution, and Hazards. National Academy Press, Washington DC, 84-95.

Christiansen, R. L. and Blank, R., Jr. (1972) Volcanic Stratigraphy of the Quaternary Rhyolite Plateau in Yellowstone National Park. Geological Survey Professional Paper 729-B. Washington, D.C.: US Government Printing Office.

Colgan, J.P., and Henry, C.D. (2009) Rapid Middle Miocene Collapse of the Mesozoic Orogenic Plateau in North-Central Nevada: International Geology Review, 51(9-11), 920–961.

Cosca, M. A., Thompson, R. A., Lee, J. P., Turner, K. J., Neymark, L. A., and Premo, W. R. (2014). 40Ar/30Ar Geochronology, Isotope Geochemistry (Sr, Nd, Pb), and Petrology of Alkaline Lavas Near Yampa, Colorado: Migration of Alkaline Volcanism and Evolution of the Northern Rio Grande Rift. Geosphere, 10(2), 1-27.

Dodd, Z. C. (2015). Petrogenesis and Rare Earth Element Economic Potential of Pilot Knob, a Pliocene(?) Alkaline Intrusive Complex in the Togwotee Pass Region, Northwestern Wyoming (USA). M.S. Thesis. Kansas State University, Manhattan, Kansas.

Downes, H., MacDonald, R., Upton, B. G. J., Cox, K. G., Bodinier, J., Mason, P. D. R., James, D., Hill, P. G., and Hearn, B. C. Jr. (2004). Ultramafic Xenoliths from the Bearpaw Mountains, Montana, USA: Evidence for Multiple Metasomatic Events in the Lithospheric Mantle Beneath the Wyoming Craton. Journal of Petrology, 45(8), 1631-1662.

Downey, A. C., Dodd, Z.C., Brueseke, M. E., and Adams, D. C. (2014). Geochemical Constraints on Cenozoic Intraplate Magmatism in the Upper Wind River Basin, Wyoming, USA [Abstract]. American Geophysical Union, Fall Meeting.

Embey-Isztin, A. and Dobosi, G. (2007). Composition of Olivines in the Young Alkali Basalts and their Peridotite Xenoliths from the Pannonian Basin. Annales Historico-Naturales Musei Nationalis Hungarici, 99, 5-22.

Feeley, T. C. (2003). Origin and Tectonic Implications of Across-Strike Geochemical Variations in the Eocene Absaroka Volcanic Province, United States. The Journal of Geology, 111(3), 329-346.

Feeley, T. C. and Cosca, M. A. (2003). Time vs. Composition Trends of Magmatism at Sunlight Volcano, Absaroka Volcanic Province, Wyoming. Geological Society of America Bulletin, 115(6), 714-728.

Feeley, T. C., Cosca, M. A., and Lindsay, C. R. (2002). Petrogenesis and Implications of Calc-Alkaline Cryptic Hybrid Magmas from Washburn Volcano, Absaroka Volcanic Province, USA. Journal of Petrology, 43(4), 663-703.

Feineman, M. D., Sruoga P., Drew, D., and Murray, T. (2010). Disequilibrium Phenocryst Textures in an Andean Volcanic Complex: Mixing or Rapid Decompression? American Geophysical Union, Fall Meeting 2010, abstract #V43C-2389

Finn, T. M. (2007). Subsurface Stratigraphic Cross Sections of Cretaceous and Lower Tertiary Rocks in the Wind River Basin, Central Wyoming. Petroleum Systems and Geologic Assessment of Oil and Gas in the Wind River Basin Province, Wyoming. U.S. Geological Survey Digital Data Series DDS-69-J, Reston, Virginia.

Foster, D. A., Mueller, P. A., Mogk, D. W., Wooden, J. L., and Vogl, J. J. (2006). Proterozoic Evolution of the Western Margin of the Wyoming Crayton: Implications for the Tectonic and Magmatic Evolution of the Northern Rocky Mountains. Can. J. Earth Sci., 43, 1601-1619

Gaschnig, R. M., Vervoort, J. D., Lewis, R. S., and Tikoff, B. (2011). Isotopic Evolution of the Idaho Batholith and Challis Intrusive Province, Northern US Cordillera. Journal of Petrology, 52(12), 2397-2429.

Hanan, B. B., Shervais, J. W., and Vetter, S. K. (2008). Yellowstone Plume-Continental Lithosphere Interaction Beneath the Snake River Plain. Geology, 36(1), 51-54

Hildreth, W., Halliday, A. N., and Christiansen, R. L. (1990). Isotopic and Chemical Evidence Concerning the Genesis and Contamination of Basaltic and Rhyolitic Magma Beneath the Yellowstone Plateau Volcanic Field. Journal of Petrology, 32(1), 63-138.

Johnson, J., and Grunder, A. L. (2000). The Making of Intermediate Composition Magma in a Bimodal Suite: Duck Butte Eruptive Center, Oregon, USA. Journal of Volcanology and Geothermal Research, 95, 175-195.

Jurdy, D. (1984). The Subduction of the Farallon Plate Beneath North America as Derived from Relative Plate Motions. Tectonics, 3(2), 107-113.

Keefer, W. R. (1970). Structural Geology of the Wind River Basin, Wyoming. Geological Survey Professional Paper 495-D. Washington, D.C.: US Government Printing Office.

Keefer, W. R. (1957). Geology of the DuNoir area, Fremont County, Wyoming. Geological Survey Professional Paper 294-E. Washington, DC: US Government Printing Office.

Kempton, P. D., Downes, H., Neymark, L. A., Wartho, J. A., Zartman, R. E., and Sharkov, E. V. (2001). Garnet Granulite Xenoliths from the Northern Baltic Shield – The Underplated Lower Crust of a Palaeoproterozoic Large Igneous Province? Journal of Petrology, 42(4), 731-763.

Kempton, P. D., Fitton, J, D., Hawkesworth, C. J., and Ormerod, D. S. (1991). Isotopic and Trace Element Constraints on the Composition and Evolution of the Lithosphere beneath the Southwestern United States. Journal of Geophysical Research, 96(B8), 13,713-13,735.

Leeman, W. P., Schutt, D. L., and Hughes, S. S. (2009). Thermal Structure Beneath the Snake River Plain: Implications for the Yellowstone Hotspot. Journal of Volcanology and Geothermal Research, 188, 57-67.

Leeman, W. P., Menzies, M. A., Mattey, D. J., and Embree, G. F. (1985). Strontium, Neodymium, and Lead Isotopic Compositions of Deep Crystal Xenoliths from the Snake River Plain: Evidence for Archean Basement. Earth and Planetary Science Letters, 75, 354-368.

Love, J. D., Christiansen, A. C., Preliminary Geologic Map of the Thermopolis 1°X2° Quadrangle, Central Wyoming [map]. 1:250,000. United States Department of the Interior, USGS.

Menzies, M. A., Leeman, W. P., Hawkesworth, C. J. (1984). Geochemical and Isotopic Evidence for the Origin of the Continental Flood Basalts with particular Reference to the Snake River Plain, Idaho, USA. Phil. Trans. R. Soc. Lond., 310, 643-660.

Menzies, M. A., Leeman, W. P., Hawkesworth, C. J. (1983). Isotopic Geochemistry of Cenozoic Volcanic Rocks Reveals Mantle Heterogeneity Below Western USA. Nature, 303.

Mirnejad, H., and Bell, K. (2006). Origin and Source Evolution of the Leucite Hills Lamproites: Evidence from Sr-Nd-Pb-O Isotopic Compositions. Journal of Petrology, 47(12), 2463-2489.

Mueller, P.A., and Wooden, J.L. (1988). Evidence for Archean Subduction and Crustal Recycling, Wyoming Province, USA. Geology, 16, 871–874

Obradovich, J.D. (1978). Age of volcanism at Togwotee Pass area in Wyoming. US Geological Survey Research 1978 (USGS Professional Paper No. 1100). Washington, DC: US Government Printing Office.

Obrebski, M., Allen, R. M., Pollitz, F., and Hung, S. (2011). Lithosphere-Asthenosphere Interaction beneath the Western United States from the Joint Inversion of Body-Wave Traveltimes and Surface-Wave Phase Velocities. Geophysical Journal International, 185, 1003-1021.

Payne, S. J., McCaffery, R., and Kattenhorn, S.A. (2013). Extension-driven right-lateral shear in

the Centennial shear zone adjacent to the eastern Snake River Plain, Idaho. Lithosphere, 5(4), 407-419.

Pierce, K. L. (2003). Pleistocene Glaciations of the Rocky Mountains. Development in Quaternary Science, 1, 63-77.

Pierce, K. L., and Morgan, L. A. (1992). The Track of the Yellowstone Hotspot: Volcanism, Faulting, and Uplift, in Link, P. K., Kuntz, M. A., and Platt, L. B., eds., Regional Geology of Eastern Idaho and Western Wyoming: Geological Society of America Memoir 179.

Pritchard, C. J., and Larson, P. B. (2013). Eruption-Triggered Mixing of Extra-Caldera Basalt and Rhyolite Complexes Along the East Gallatin–Washburn Fault Zone, Yellowstone National Park, WY, USA. Lithos, 175-176

Protska, H. J. and Antweiler, J. C. (1979). Mineral Resources of the Du Noir Addition, Washakie Wilderness, Freemont County, Wyoming. Washington, DC: US Government Printing Office

Ray, R. R. and Keefer, W. R. (1985). Wind River Basin, central Wyoming, in Gries, R., and Dyer, R. C. Seismic Exploration of the Rocky Mountain Region. Rocky Mountain Association of Petroleum Geologists and Denver Geophysical Society, 201-212.

Rudnick, R. L. (1990). Nd and Sr Isotopic Compositions of Lower Crustal Xenoliths from North Queensland, Austraila: Implications for Nd model ages and Crustal Growth Processes. Chemical Geology, 83, 195-208.

Rudnick, R.L. and Goldstein, S.L. (1990). The Pb Isotopic Composition of Lower Crustal Xenoliths and the Evolution of Lower Crustal Pb. Earth and Planetary Science Letters, 98, 192-207.

Seeland, D. A. and Brauch, E. F. (1975). Status of Mineral Resource Information for the Wind River Indian Reservation, Wyoming. BIA Administrative Report 8

Stacey, J.S. and Kramers, J.D. (1975). Approximation of Terrestrial Lead Isotope Evolution by a 2-Stage Model. Earth and Planetary Science Letters, 26(2), 207-221.

Steiner, A., and Streck, M. J. (2013). The Strawberry Volcanics: Generation of 'Orogenic' Andesites from Thoeiite within an Intra-Continental Volcanic Suite Centered on the Columbia River Flood Basalt Province, USA. Geological Society, London, Special Publications, 385(1), 281-302

Smithies, R. H., Champion, D. C., and Sun, S-.S. (2004). Evidence for Early LREE-Enriched Mantle Source Regions: Diverse Magmas from the c. 3.0 Ga Mallina Basin, Pilbara Craton, NW Australia. Journal of Petrology, 45(8), 1515-1537

Wang, K., Plank, T., Walker, J. D., Smith, E. I. (2002). A Mantle Melting Profile Across the Basin

and Range, SW USA. Journal of Geophysical Research, 107(B1).

Wooden, J. L. and Mueller, P. A. (1988). Pb, Sr, and Nd Isotopic Compositions of a Suite of Late Archean, Igneous Rocks, eastern Beartooth Mountains: Implications for Crust-Mantle Evolution. Earth and Planetary Science Letters, 87(1-2), 59-72.

Appendix A - Sample Locations and Petrographic Descriptions

All locations are presented in UTM coordinates based off the NAD27 CONUS datum with all samples plotting in UTM Zone 12. Rock type classifications are based on total alkali vs. silica classification from LeBas et. al. 1986. Descriptions contain field and hand sample information. All samples have been point counted. Modes are listed underneath each thin section description.

Sample ID: MB13-1 **Easting:** 0576911
Rock Type: Andesite **Northing:** 4840086

Hand Sample: Light gray, aphanitic rock with sparse, small vesicles averaging 1-2 mm in diameter and no observable phenocrysts.

Thin Section: Aphanitic, holocrystalline fine grained rock. Subhedral pyroxene and plagioclase crystals. Elongate orthopyroxene outnumber smaller, more spherical clinopyroxene. Vesicles are circular and rare. Orthopyroxene crystals have low relief and very low interference colors. Groundmass is about 70% plagioclase mixed with small orthopyroxenes and oxides. Ophitic textures observed. Poikilitic texture observed where orthopyroxenes are found within a sieved plagioclase. Most orthopyroxene phynocrysts are sieved and partially resorbed.

Mode: Matrix 69.04%, orthopyroxene 27.06%, Vesicles 2.23%, clinopyroxene 0.98%, Plagioclase 0.70%

Sample ID: MB13-3 **Easting:** 0615287
Rock Type: Vesicular Basalt **Northing:** 4834259

Hand Sample: Light to medium gray, aphanitic rock with sparse iridescent olivine phenocrysts.

Thin Section: Aphanitic, holocrystalline, extremely fine-grained matrix with sparse trachytic plagioclase. Crystals are euhedral to anhedral, especially the olivines. Olivines average 0.75 mm in diameter. Larger plagioclase laths average 0.75 mm. Groundmass is approximately 25-30% trachytic plagioclase laths mixed with olivine and possibly pyroxene. Anhedral olivines have been partially resorbed and several are skeletal. All olivines have iddingsite rims. Vesicles are >8% of section.

Mode: Matrix 71.73%, Olivine 19.74%, Vesicles 8.24%, Plagioclase 0.43%

Sample ID: MB13-4B **Easting:** 0615290
Rock Type: Basalt **Northing:** 4834043

Hand Sample: Dark gray basalt with green olivine phenocrysts. Vesicles average 3-4 mm in diameter.

Thin Section: Aphanitic, holocrystalline rock. Fine-grained phenocrysts include subhedral to euhedral plagioclase, clinopyroxene, and olivine. Abundant vesicles, some as large as 2.25 mm. Very fine-grained groundmass; matrix is plagioclase and pyroxene. Clots of ophitic textures with separate examples of clinopyroxene and olivine enclosed by elongate plagioclase laths are scattered throughout. Several plagioclase crystals have undulatory extinction along with usual twinning. Very little iddingsite observed on olivine.

Mode: Matrix 48.50%, Plagioclase 24.30%, Vesicles 16.50%, Olivine 4.65%, Clinopyroxene 6.01%

Sample ID: MB13-4A
Rock Type: Basalt
Easting: 0615290
Northing: 4834043

Hand Sample: Light gray porphyritic rock. Fine grained groundmass with small (1 mm or less) iridescent olivine phenocrysts. No vesicles.

Thin Section: Aphanitic, holocrystalline rock. Phenocrysts include sparse plagioclase laths averaging 1 mm long, olivine, and resorbed orthopyroxene. Coarse-grained matrix, with orthopyroxene, clinopyroxene and several trachytic plagioclase crystals reaching 0.25 mm long. Oxide minerals are sparse. Poikilitic textures with olivine embedded in resorbed orthopyroxene are common. Iddingsite is abundant within and surrounding olivine crystals. The majority of olivines are skeletal and/or resorbed.

Mode: Matrix 50.98%, Plagioclase 0.42%, Orthopyroxene 18.23%, Clinopyroxene 1.12%, Vesicles 0.28%

Sample ID: AD14-1
Rock Type: Basalt
Easting: 0614668
Northing: 4833588

Hand Sample: Gray, massive basalt with green and blue iridescent olivine crystals and small flattened vesicles. The majority of olivines are <1 mm in size.

Thin Section: Aphanitic, holocrystalline, olivine-rich sample. Coarse-grained olivine is euhedral to subhedral with few scattered skeletal crystals. Fine-grained groundmass of mostly plagioclase, with larger plagioclase phenocrysts that are tractyic. Olivine and possibly some pyroxenes make up the groundmass in a very fine grained matrix (<0.01 mm). Light red-brown iddingsite halos surround the olivines. Several olivines are resorbed, and some olivines have possible spinel inclusions. Sparse oxides are observed throughout.

Mode: Matrix 76.26%, Olivine 18.11%, Vesicles 5.40%, Plagioclase 0.24%

Sample ID: AD14-2
Rock Type: Basalt
Easting: 0615232
Northing: 4833924

Hand Sample: Gray, massive, porphyritic basalt with iridescent olivine phenocrysts averaging 1 mm or slightly larger.

Thin Section: Aphanitic, holocrystalline rock with coarse-grained euhedral to subhedral olivine crystals. Plagioclase is mostly uniform in size, with a few exceptions of larger crystals. Groundmass consists of about 80% plagioclase, with oxides, olivines, and pyroxenes scattered throughout. Plagioclase in groundmass has trachytic texture assemblages.

Mode: Matrix 80.85%, Olivine 18.79%, Plagioclase 0.24%, Vesicles 0.12%

Sample ID: AD14-4 **Easting:** 0578719
Rock Type: Andesite Scoria **Northing:** 4836326

Hand Sample: Dark gray, fresh, highly vesicular scoria from the Lava Mountain cinder cone. Phenocrysts are glassy and extremely small. The largest vesicles are only a few mm in diameter.

Thin Section: Aphanitic, hypocrystalline, fine-grained rock with euhedral orthopyroxenes. Most orthopyroxenes are boxy as opposed to elongated and average ~0.1 mm. Very fine grained plagioclase matrix with fewer crystals than see at Spring Mountain. Vesicles are abundant. Matrix is about 30% glass, 10% orthopyroxenes, and 60% plagioclase, which is extremely disoriented. Zoning is evident in select orthopyroxenes. Several orthopyroxenes are skeletal. Vesicles constitute almost half the section.

Mode: Matrix 48.39%, Vesicles 44.89%, Orthopyroxene 6.72%

Sample ID: AD14-5 **Easting:** 0578909
Rock Type: Andesite **Northing:** 4836617

Hand Sample: Dark gray, aphanitic, vesicular rock with no clear visible phenocrysts. Vesicles average about 1 mm in diameter, however rare larger vesicles are up to 14 mm. Plagioclase cleavage is sparsely evident.

Thin Section: Aphanitic, holocrystalline, fine-grained scoria. Few vesicles. Most crystals are subhedral to euhedral, as less than 5 pyroxenes are considered anhedral and heavily resorbed. Larger plagioclase laths average 1 mm. Groundmass is orthopyroxne, fine-medium plagioclase, and few clinopyroxenes. Sieved orthopyroxenes are abundant, with few clinopyroxenes. Ophitic textures are common. Glomerophyric textures of orthopyroxenes and clinopyroxenes are common. Some orthopyroxenes are twinned. One feldspar phenocryst is extremely resorbed.

Mode: Matrix 65.48%, Orthopyroxene 24.37%, Vesicles 7.23%, Clinopyroxene 1.90%, Plagioclase 1.02%

Sample ID: AD14-6 **Easting:** 0579103
Rock Type: Andesite **Northing:** 4836741

Hand Sample: Light gray, massive, aphanitic rock. Phlogopite sheets are in several vesicles/fractures. Pyroxene crystals are sparse and <1 mm. There is faint evidence for linear flow textures.

Thin Section: Aphanitic, holocrystalline, fine-grained andesite. Pyroxene phenocrysts are very small and subhedral to anhedral. There is some evidence of crystals weathering to clay. Clots of coarser grained plagioclase are interspersed throughout the groundmass. Groundmass is trachytic plagioclase, small vesicles, and orthopyroxenes. Sparse zoning observed on several orthopyroxenes, along with skeletal features and resorption. Two xenocrystic plagioclase crystals are surrounded by a reaction rim.

Mode: Matrix 86.42%, orthopyroxene 12.29%, Vesicles 0.91%, Clinopyroxene 0.23%, Plagioclase 0.13%

Sample ID: AD14-7 **Easting:** 0579271
Rock Type: Andesite **Northing:** 4836856

Hand Sample: Light gray, aphanitic to slightly porphyritic rock. One white phenocryst/microcryst (presumed to be plagioclase) is 3 mm wide. Black equant orthopyroxene crystals are very small.

Thin Section: Aphanitic, holocrystalline rock. Many elongate orthopyroxenes averaging ~0.1 mm in length are euhedral and have very high interference colors. Extremely fine grained matrix of plagioclase and clinopyroxene, with no orientation to plagioclase matrix grains. Several orthopyroxenes are resorbed and skeletal. One microcline crystal is observed along with several xenocrysts are similar to those seen in AD14-11.

Mode: Matrix 74.49%, Orthopyroxene 24.36%, Vesicles 2.18%, Clinopyroxene 0.38%

Sample ID: AD14-8 **Easting:** 0579359
Rock Type: Andesite **Northing:** 4836727

Hand Sample: Dark gray, aphantic, vesicular rock. Vesicles average 1-2 mm in diameter.

Thin Section: Aphanitic, holocrystalline sample. Elongated orthopyroxene phenocrysts are suhedral an average 0.5 mm across. Plagioclase groundmass shows slight flow orientation. Small clinopyroxenes are scattered in groundmass along with orthopyroxene and plagioclase. Coarser-grained matrix compared to AD14-7. Several orthopyroxenes are skeletal. Vesicles common.

Mode: Matrix 83.14%, Orthopyroxene 11.84%, Vesicles 5.02%

Sample ID: AD14-9 **Easting:** 0579801
Rock Type: Andesite **Northing:** 4836750

Hand Sample: Light gray, massive, aphanitic rock with sparse black equant pyroxene phenocrysts and no vesicles.

Thin Section: Aphanitic, holocrystalline rock with sparse pyroxene phenocrysts in an extremely fine-grained matrix. Pyroxenes are anhedral. Grains in the matrix are disoriented, and the groundmass is fine grained plagioclase, orthopyroxene, and about 20% scattered oxides. One

orthopyroxene has plagioclase laths growing within it. Few pyroxenes are twinned and many are resorbed. Xenocrysts with phlogopite as in AD14-11 are sparse. Slight zoning in some orthopyroxenes. Several pyroxenes are skeletal.

Mode: Matrix 94.61%, Orthopyroxene 5.01%, Clinopyroxene 0.26%, Vesicles 0.13%

Sample ID: AD14-10 **Easting:** 0580078
Rock Type: Andesite/Dacite **Northing:** 4837144

Hand Sample: Black, aphanitic/vitropheric, dense, massive rock with sparse white xenocrysts found within vesicles and the rock itself. Identical to AD14-12.

Thin Section: Aphanitic, hypocrystalline sample. Phenocrysts are subhedral to anhedral, . Matrix is glassy with extremely oriented sparse flow path plagioclase; larger crystals have swallowtail textures. There are very few phenocrysts; they are all plagioclase and one extremely small (~1.8 mm) orthopyroxene. Groundmass is about 20% glass. Plagioclase phenocrysts are extremely resorbed. Some feldspars have sweeping extinction.

Mode: Matrix 96.39% Plagioclase 1.80%, Vesicles 1.53%, Clinopyroxene 0.28%

Sample ID: AD14-11 **Easting:** 0580466
Rock Type: Basaltic Andesite **Northing:** 4837482

Hand Sample: Light gray, aphanitic rock with sparse evidence of possible flow patterns. Phlogopite crystals are scattered in vesicles and fractures in the rock. Very few small, black pyroxene crystals.

Thin Section: Aphanitic, holocrystalline rock with subhedral to anhedral phenocrysts. Phenocrysts include orthopyroxene and olivine. Trachytic plagioclase in the matrix shows extreme flow path directions in the groundmass. Groundmass is primarily very sparse oxides and plagioclase. Phlogopite surrounds xenocrystic feldspars that are scattered throughout the section averaging 0.40 mm, athough there is no phlogopite in the groundmass. Several olivines are skeletal. Few orthopyroxenes are zoned.

Mode: Matrix 80.83%, Orthopyroxene 9.38%, Olivine 6.97%, Vesicles 2.82%

Sample ID: AD14-12 **Easting:** 0580900
Rock Type: Andesite/Dacite **Northing:** 4837675

Hand Sample: Black, aphanitic/vitropheric, dense, massive rock with sparse white xenocrysts found within vesicles and the rock itself. Identical to AD14-10.

Thin Section: Aphanitic, hypocrystalline matrix with very few, almost no, phenocrysts in a fine-grained section. The few plagioclase and one orthoclase phenocrysts are euhedral to subhedral. Groundmass is very little glass with extremely small plagioclase crystals that have swallowtail

textures. One orthopyroxene has a reaction rim of more pyroxene. Some of the small, square plagioclase crystals are zoned and/or extremely resorbed.

Mode: Matrix 97.47%, Plagioclase 1.73%, Vesicles 0.80%

Sample ID: AD14-13 **Easting:** 0580433
Rock Type: Andesite **Northing:** 4832009

Hand Sample: Dark gray, aphanitic to slightly coarser grained rock. Sparse vesicles are <1 mm.

Thin Section: Aphanitic, holocrystalline sample with subhedral orthopyroxene phenocrysts. No phenocrysts are observed besides orthopyroxenes. Clots of coarser grained plagioclase is seen in the groundmass. Groundmass is orthopyroxene, altered material, and plagioclase. Sparse, very small vesicles measuring about 0.25 mm or less across. One orthopyroxene crystal is sieved.

Mode: Matrix 77.55%, Orthopyroxene 12.13%, Vesicles 8.77%, Plagioclase 0.90%

Sample ID: AD14-14 **Easting:** 0578461
Rock Type: Basaltic Andesite **Northing:** 4838653

Hand Sample: Light gray, massive, aphanitic rock with sparse equant pyroxene phenocrysts. Olivines are extremely small and green in color. Phlogopite is scattered in fractures.

Thin Section: Aphanitic, holocrystalline rock. Phenocrysts include euhedral to subhedral orthopyroxene, clinopyroxene, and olivine. The orthopyroxene phenocrysts are more elongated, while the clinopyroxene is more spherical. Pics. Closely-packed flow path aligned plagioclase is seen in the matrix, with various weathering particles and intersertial clinopyroxene. Some olivines have dark reaction rims from oxide minerals, and some are skeletal. One single xenocrystic quartz crystal is extremely fractured and approximately 4.6 mm across. Few orthopyroxene have skeletal features.

Mode: Matrix 75.17%, Orthopyroxene 16.10%, Olivine 5.18%, Quartz 3.59%

Sample ID: AD14-15 **Easting:** 0578165
Rock Type: Basaltic Andesite **Northing:** 4838976

Hand Sample: Light gray to brown rock with evidence of linear flow textures and small black equant pyroxene phenocrysts up to 1 mm in size.

Thin Section: Aphanitic, holocrystalline section. Phenocrysts include sparse euhedral to subhedral olivines and orthopyroxenes. Phenocrysts are small and select phenocrysts are on average not much larger than 1.5 mm. Groundmass is dominantly trachytic plagioclase (about 90%), sparse oxides, and orthopyroxene. Orthopyroxenes are zoned and sieved, and generally box shaped. Some olivines are skeletal.

Mode: Matrix 90.53%, Orthopyroxene 5.93%, Olivine 3.28%, Vesicles 0.25%

Sample ID: AD14-16 **Easting:** 0578783
Rock Type: Andesite **Northing:** 4838949

Hand Sample: Black, glassy, fragile, aphanitic/vitrophyric massive rock with white xenocrysts in both the groundmass and several vesicles. Empty vesicles are very small.

Thin Section: Aphanitic, holocrystalline rock with almost no phenocrysts except larger plagioclase crystals and two subhedral orthopyroxenes. Extremely fine-grained trachytic plagioclase is found in the matrix, but swallowtail texture is not profoundly evident. If there is glass, it is not widely evident. Groundmass is orthopyroxene, glass, and plagioclase. One orthopyroxene has a reaction rim of other pyroxene material.

Mode: Matrix 98.18%, Orthopyroxene 0.73%, Vesicles 1.09%

Sample ID: AD14-17 **Easting:** 0578826
Rock Type: Basaltic Andesite **Northing:** 4839004

Hand Sample: Aphanitic, massive, light gray rock with sparse black pyroxene phenocrysts.

Thin Section: Aphanitic, holocrystalline sections with olivine and pyroxene phenocrysts. There is more olivine evident here than in most other Lava Mountain sections. Groundmass is orthopyroxenes, clinopyroxenes, and plagioclase. The majority of olivines, averaging 0.35 mm, are skeletal and surrounded by dark oxides. Several orthopyroxenes are sieved and very resorbed, sometimes to where only a thin rim of the mineral remains.

Mode: Matrix 83.91%, Orthopyroxene 10.47%, Olivine 4.98%, Vesicles 0.64%

Sample ID: AD14-18 **Easting:** 0578117
Rock Type: Andesite **Northing:** 4838932

Thin Section: Aphanitic, holocrystalline slide. Phenocrysts include both elongated and square orthopyroxene, with some orthopyroxenes displaying twinning. Medium-grained matrix of evenly split plagioclase and orthopyroxene, with sparse clinopyroxene. Extremely disoriented plagioclase in groundmass, with altered material between the crystals. Sieved orthopyroxenes and some plagioclase show signs of zoning. Several vesicles are about 0.5 mm wide.

Mode: Matrix 72.82%, Orthopyroxene 23.46%, Vesicles 3.72%

Sample ID: CRM2 **Easting:** 0592170
Rock Type: Dacite **Northing:** 4853994

Hand Sample: Dark gray to black, aphanitic, vesicular rock with white xenocrysts scattered throughout the groundmass. Vesicles are larger and average 4 mm in diameter.

Thin Section: Aphanitic, hypocrystalline thin section. The only phenocrysts are orthopyroxenes. Some very strongly oriented trachytic plagioclase in the matrix has swallowtail textures. Groundmass is very fine grained plagioclase crystals. Many orthopyroxenes are boxy, as opposed to elongated. Several are sieved and skeletal.

Mode: Matrix 93.14%, Orthopyroxene 6.50%, Plagioclase 0.25%, Vesicles 0.12%

Sample ID: CRM3 **Easting:** 0592170
Rock Type: Dacite **Northing:** 4853994

Thin Section: Trachytic plagioclase in matrix, few swallowtail textures. One large pyroxene phenocryst measures about 1 mm across. Groundmass is plagioclase and orthopyroxene. Elongated pyroxenes are aligned with very strongly oriented plagioclase in flow pattern. Both skeletal and resorbed orthopyroxenes are present. Some pyroxenes have been so completely resorbed only a thin rim of the original mineral still remains.

Mode: Matrix 92.00%, Orthopyroxene 6.25%, Plagioclase 0.15%, Vesicles 0.15%

Sample ID: CRM4 **Easting:** 0592051
Rock Type: Basaltic Andesite **Northing:** 4853781

Thin Section: Aphanitic, holocrystalline rock with coarser grains. Olivine phenocrysts are subhedral to anhedral, several of which have black oxide rims. Oxides also fill inclusions of several olivines. They are in extreme disequilibrium and are altering to something else. Clots of clinopyroxenes are observed, with some showing signs of zoning. Plagioclase are small, thin, euhedral, needle-like crystals. Groundmass is mostly plagioclase and climopyroxene, with additional quartz, oxides, and altered material. String of quartz crystals are found throughout groundmass with ungalatory extinction. Orthopyroxenes are extremely sparse.

Mode: Matrix 57.96% (including quartz crystals), Olivine 23.04%, Clinopyroxene 18.58%, Plagioclase 0.45

Appendix B - Geochemistry

The symbol "-" means that element was not determined for that sample. Major and trace elements for all AD samples were determined by ICP-OES. All MB samples were analyzed for major and trace elements by XRF. Only select samples were analyzed for REE, and so only those samples are listed for that section. All major element data reported in this appendix is raw data.

Major Element Results (wt. %)

Samples	MB13-1	MB13-3	MB13-4A	MB13-4B	AD14-1	AD14-2
SiO_2	59.52	50.23	49.49	50.01	49.68	49.78
TiO_2	0.76	0.71	0.72	0.92	0.75	0.75
Al_2O_3	15.53	14.44	14.73	16.69	14.55	14.55
Fe_2O_3	0.95	2.38	2.34	1.64	9.66	9.52
FeO	5.68	6.62	6.92	7.32	-	-
MnO	0.11	0.15	0.15	0.15	0.15	0.15
MgO	5.22	11.41	11.82	7.68	11.28	10.91
CaO	6.83	10.37	10.60	11.30	10.32	10.82
Na_2O	2.91	2.01	1.98	2.26	2.00	2.04
K_2O	1.92	0.58	0.45	0.61	0.53	0.49
P_2O_5	0.23	0.17	0.16	0.20	0.16	0.16
Total	**100.28**	**100.26**	**100.05**	**100.04**	**99.08**	**99.17**
LOI	0.62	1.19	0.69	1.26	0.92	0.83

Sample	AD14-4	AD14-5	AD14-6	AD14-7	AD14-8
SiO_2	58.06	58.95	59.41	59.50	58.55
TiO_2	0.79	0.79	0.81	0.81	0.82
Al_2O_3	15.60	15.44	15.66	15.68	15.66
Fe_2O_3	7.24	7.00	7.03	6.97	7.17
MnO	0.11	0.10	0.10	0.10	0.11
MgO	5.20	4.93	4.81	4.70	4.93
CaO	7.10	6.64	6.73	6.68	6.85
Na_2O	2.95	2.97	3.06	3.08	2.94
K_2O	1.91	2.00	2.00	1.99	1.99
P_2O_5	0.26	0.23	0.25	0.25	0.25
Total	**99.22**	**99.05**	**99.86**	**99.75**	**99.28**
LOI	0.78	0.95	0.14	0.25	0.72

Sample	AD14-9	AD14-10	AD14-11	AD14-12	AD14-13	AD14-14
SiO_2	57.94	62.35	55.57	62.55	59.09	55.70
TiO_2	0.88	0.89	0.84	0.91	0.81	0.83
Al_2O_3	15.91	15.97	15.68	15.96	15.58	15.66
Fe_2O_3	7.66	6.74	8.22	6.76	6.97	8.00
MnO	0.12	0.10	0.13	0.10	0.10	0.12
MgO	4.72	2.27	6.61	2.23	4.77	6.38
CaO	7.25	5.64	8.14	5.63	6.66	8.06
Na_2O	3.07	3.33	2.79	3.31	3.05	2.78
K_2O	1.72	1.69	1.63	1.67	1.99	1.68
P_2O_5	0.27	0.21	0.28	0.21	0.25	0.28
Total	**99.53**	**99.19**	**99.89**	**99.32**	**99.28**	**99.50**
LOI	0.47	0.81	0.11	0.68	0.72	0.50

Sample	AD14-15	AD14-16	AD14-17	AD14-18
SiO_2	55.46	57.54	55.29	57.99
TiO_2	0.84	0.87	0.84	0.80
Al_2O_3	15.63	15.40	15.60	15.44
Fe_2O_3	8.01	7.10	7.99	7.10
MnO	0.13	0.11	0.12	0.11
MgO	6.50	3.28	6.49	5.41
CaO	8.04	6.38	8.04	6.94
Na_2O	2.76	3.19	2.74	2.93
K_2O	1.67	1.70	1.65	1.95
P_2O_5	0.28	0.24	0.28	0.24
Total	**99.32**	**95.81**	**99.05**	**98.91**
LOI	0.68	4.19	0.95	1.09

Trace Element Results (ppm)

Sample	MB13-1	MB13-3	MB13-4A	MB13-4B	AD14-1	AD14-2
Ni	107	295	280	95	322	296
Cr	308	955	977	255	927	907
Sc	18.0	28.0	29.0	30.0	30.0	30.5
V	161	210	207	231	180	181
Ba	1208	544	412	458	479	413
Rb	39	10	9	11	4	4
Sr	570	430	406	490	394	391
Zr	200	95	90	105	82	81
Y	29	25	24	25	17	17
Nb	11.7	4.2	3.8	5.1	5.9	6.0
Ga	18	14	14	16	-	-
Cu	34	66	68	31	91	80
Co	33	58	58	46	54	54
Zn	78	75	77	76	70	68
Pb	3	14	<1	<1	11	15
U	1	<0.5	<0.5	1	-	-
Th	6	<0.5	<0.5	<0.5	-	-
Cs	-	-	-	-	-	-
Hf	-	-	-	-	-	-
Ta	-	-	-	-	-	-
Mo	-	-	-	-	1	1
Be	-	-	-	-	1	1

Sample	AD14-4	AD14-5	AD14-6	AD14-7	AD14-8
Ni	87	89	83	77	84
Cr	215	221	203	200	201
Sc	21.1	19.4	19.4	19.3	20.2
V	146	134	138	136	142
Ba	1481	1320	1417	1426	1457
Rb	33	38	36	36	34
Sr	633	541	639	638	633
Zr	178	191	189	188	186
Y	23	25	24	24	24
Nb	14.7	14.6	14.4	15.1	16.7
Ga	-	-	-	-	-
Cu	34	31	40	46	35
Co	28	28	27	26	28
Zn	77	78	78	76	78
Pb	18	17	19	19	16
U	-	-	-	-	-
Th	-	-	-	-	-
Cs	-	-	-	-	-
Hf	-	-	-	-	-
Ta	-	-	-	-	-
Mo	5	7	6	6	5
Be	1	1	1	1	1

Sample	AD14-9	AD14-10	AD14-11	AD14-12	AD14-13	AD14-14
Ni	69	11	119	12	82	119
Cr	126	27	240	26	204	264
Sc	21.8	16.4	25.2	16.6	19.4	24.8
V	160	127	173	132	138	170
Ba	1520	1141	1563	1134	1428	1571
Rb	22	21	21	19	34	22
Sr	759	600	694	588	634	666
Zr	166	176	152	178	189	154
Y	22	23	21	24	24	21
Nb	16.7	8.7	17.8	8.5	15.6	18.7
Ga	-	-	-	-	-	-
Cu	42	22	38	23	44	37
Co	29	18	34	17	27	33
Zn	79	88	70	78	97	94
Pb	16	17	14	16	17	16
U	-	-	-	-	-	-
Th	-	-	-	-	-	-
Cs	-	-	-	-	-	-
Hf	-	-	-	-	-	-
Ta	-	-	-	-	-	-
Mo	7	2	1	1	7	5
Be	1	1	1	1	1	1

Sample	AD14-15	AD14-16	AD14-17	AD14-18
Ni	118	35	115	99
Cr	275	54	271	251
Sc	24.8	18.8	24.8	20.5
V	168	142	169	142
Ba	1571	1342	1563	1395
Rb	22	20	22	32
Sr	665	689	666	596
Zr	156	170	155	181
Y	21	23	21	24
Nb	16.5	13.9	18.5	13.0
Ga	-	-	-	-
Cu	44	25	32	35
Co	35	22	33	29
Zn	76	74	77	72
Pb	15	18	15	15
U	-	-	-	-
Th	-	-	-	-
Cs	-	-	-	-
Hf	-	-	-	-
Ta	-	-	-	-
Mo	2	6	1	6
Be	1	1	1	1

Rare Earth Element Results (ppm)

Sample	MB13-3	MB13-4A	MB13-4B	AD14-1	AD14-4	AD14-9
La	23.2	23.1	30.1	23.8	54.5	53.2
Ce	45.2	45.5	58.8	46.1	107.9	104.3
Pr	5.13	5.11	6.41	5.17	11.95	11.52
Nd	18.2	18.4	22.9	18.6	43.0	41.5
Sm	3.70	3.72	4.36	3.70	7.69	7.12
Eu	1.04	1.06	1.25	1.05	1.76	1.77
Gd	3.06	3.12	3.68	3.13	5.40	4.95
Tb	0.53	0.53	0.62	0.53	0.86	0.79
Dy	3.04	3.09	3.57	3.10	4.56	4.25
Ho	0.59	0.60	0.69	0.60	0.88	0.78
Er	1.73	1.76	2.01	1.77	2.45	2.30
Tm	0.24	0.24	0.28	0.24	0.34	0.31
Yb	1.72	1.75	2.00	1.75	2.40	2.27
Lu	0.25	0.26	0.29	0.26	0.35	0.33

Sample	AD14-10	AD14-14	AD14-17
La	42.7	49.8	49.9
Ce	85.5	97.7	97.4
Pr	9.73	10.69	10.68
Nd	36.0	38.4	38.4
Sm	6.77	6.77	6.69
Eu	1.79	1.69	1.66
Gd	5.10	4.82	4.76
Tb	0.82	0.78	0.77
Dy	4.48	4.17	4.12
Ho	0.84	0.77	0.80
Er	2.44	2.29	2.25
Tm	0.34	0.31	0.30
Yb	2.41	2.29	2.26
Lu	0.35	0.34	0.33

Microprobe Analysis Results

Slide	Point	SiO2	TiO2	Al2O3	FeO	MnO	MgO
MB-13-4a	Ol1-1	38.10	0.00	0.02	20.22	0.29	40.54
MB-13-4a	Ol1-2	37.69	0.01	0.00	22.89	0.33	38.32
MB-13-4a	Ol4-2	37.48	0.01	0.00	23.22	0.35	38.07
MB-13-4a	Ol4-1	38.31	0.00	0.02	19.21	0.26	41.24
MB-13-4a	Ol2-1	38.82	0.01	0.02	15.84	0.22	43.89
MB-13-4a	Ol3-2	37.58	0.00	0.00	23.05	0.33	37.79
MB-13-4a	Ol5-1	38.10	0.01	0.01	19.72	0.29	40.59
MB-13-4a	Ol2-2	37.30	0.01	0.00	21.65	0.32	39.35
MB-13-4a	Ol5-2	37.33	0.01	0.00	23.49	0.34	37.31
MB-13-4a	Ol3-1	38.12	0.01	0.02	18.49	0.26	41.47
MB13-3	Ol6-1	39.44	0.00	0.02	10.52	0.14	47.89
MB13-3	Ol8-2	39.29	0.00	0.03	10.07	0.14	48.05
MB13-3	Ol7-1	39.34	0.00	0.02	9.84	0.14	48.20
MB13-3	Ol9-2	39.21	0.00	0.04	9.71	0.14	48.10

Slide	Point	CaO	NiO	Cr2O3	Total
MB-13-4a	Ol1-1	0.22	0.21	0.05	99.64
MB-13-4a	Ol1-2	0.19	0.18	0.02	99.64
MB-13-4a	Ol4-2	0.20	0.17	0.03	99.53
MB-13-4a	Ol4-1	0.18	0.23	0.05	99.50
MB-13-4a	Ol2-1	0.18	0.33	0.07	99.37
MB-13-4a	Ol3-2	0.21	0.18	0.04	99.19
MB-13-4a	Ol5-1	0.20	0.20	0.05	99.17
MB-13-4a	Ol2-2	0.18	0.20	0.05	99.06
MB-13-4a	Ol5-2	0.22	0.18	0.03	98.91
MB-13-4a	Ol3-1	0.23	0.23	0.06	98.87
MB13-3	Ol6-1	0.20	0.37	0.15	98.75
MB13-3	Ol8-2	0.19	0.38	0.13	98.29
MB13-3	Ol7-1	0.20	0.40	0.14	98.29
MB13-3	Ol9-2	0.21	0.38	0.15	97.96

Slide	Point	Fo	Fa
MB-13-4a	Ol1-1	77.66	21.73
MB-13-4a	Ol1-2	74.43	24.94
MB-13-4a	Ol4-2	74.01	25.32
MB-13-4a	Ol4-1	78.86	20.61
MB-13-4a	Ol2-1	82.76	16.75
MB-13-4a	Ol3-2	74.01	25.33
MB-13-4a	Ol5-1	78.11	21.29
MB-13-4a	Ol2-2	75.95	23.45
MB-13-4a	Ol5-2	73.39	25.92
MB-13-4a	Ol3-1	79.51	19.89
MB13-3	Ol6-1	88.65	10.93
MB13-3	Ol8-2	89.12	10.48
MB13-3	Ol7-1	89.35	10.23
MB13-3	Ol9-2	89.43	10.13

Radiogenic Isotope Results

Sample	MB13-3	AD14-4	AD14-10	AD14-17
87Sr/86Sr	0.70608	0.70723	0.70751	0.70700
143Nd/144Nd	0.51169	0.51157	0.51149	0.51163
206Pb/204Pb	16.390	16.401	16.337	16.456
207Pb/204Pb	15.408	15.415	15.406	15.419
208Pb/204Pb	37.641	37.658	37.421	37.594